In Vivo Computation - Where Computing Meets Nanosystem for Smart Tumor Biosensing

A thesis submitted in fulfilment of the requirements for the degree of

Doctor of Philosophy in Engineering

by

Muhammad Ali

Division of Health, Engineering, Computing and Science

THE UNIVERSITY OF WAIKATO
Te Whare Wānanga o Waikato

February 2023

Abstract

According to World Health Organization, 13.1 million people will die in the world just because of cancer by 2030. Early tumor detection is very crucial to saving the world from this alarming mortality rate. However, it is an insurmountable challenge for the existing medical imaging techniques with limited imaging resolution to detect microscopic tumors. Hence, the need of the hour is to explore novel cross-disciplinary strategies to solve this problem. The rise of nanotechnologies provides a strong belief to solve complex medical problems such as early tumor detection. Nanoparticles with sizes ranging between 1-100 nanometers can be used as contrast agents. Their small sizes enable them to leak out of blood vessels and accumulate within tumors. Moreover, their chemical, optical, magnetic and electronic properties also change at nanoscale, which make them an ideal probing agent to spatially highlight the tumor site. Though, using nanoparticles to target malignant tumors is a promising concept, only 0.7% of the injected nanoparticles reach the tumor according to the statistical results of last 10 years.

In this thesis, we propose novel *in vivo* computational frameworks for fast, accurate and robust nanobiosensing. Specifically, the peritumoral region corresponds to the "objective function"; the tumor is the "global optimum"; the region of interest is the "domain" of the objective function; and the nanoswimmers are the

"computational agents" (i.e., guesses or optimization variables). First, in *externally manipulable in vivo computation*, nanoswimmers are used as contrast agents to probe the region of interest. The observable characteristics of these nanoswimmers, under the influence of tumor-induced biological gradients, are utilized by the external tracking system to steer nanoswimmers towards the possible tumor direction. To take it one step ahead, we provide solutions to the real-life constraints of *in vivo* natural computation such as uniformity of the external steering force and finite life span of the nanoswimmers. To overcome these challenges, we propose a multi-estimate-fusion strategy to obtain a common steering direction for the swarm of nanoswimmers and an iterative memory-driven gradient descent optimization strategy for faster tumor sensitization.

Next, we propose a parallel framework called *autonomous in vivo computation*, where the tumor sensitization is highly scalable and tracking-free. We demonstrate that the tumor-triggered biophysical gradients can be leveraged by nanoparticles to collectively move toward the potential tumor hypoxic regions without the aid of any external intervention. Although individual nanoparticles have no target-directed locomotion ability due to limited communication and computation capability, we show that once passive collaboration is achieved, they can successfully avoid obstacles and detect the tumor.

Finally, to address the respective limitations of externally manipulable and autonomous settings such as constant monitoring and slow detection, we propose a *semi-autonomous in vivo computational* framework. We show that the spot sampling strategy for an autonomous swarm of nanoswimmers can achieve faster tumor sensitization in complex environments. This approach makes the swarm highly scalable along with giving it the freedom from constant monitoring.

The performance of the aforementioned tumor sensitization frameworks is evaluated through comprehensive *in silico* experiments that mimic the realistic targeting processes in externally manipulable, self-regulatable and semi-autonomous settings. The efficacies of the proposed frameworks are demonstrated through numerical simulations that incorporate various physical constraints with respect to controlling and steering of computational agents, their motion in discretized vascular networks and their motion under the influence of disturbance and noise.

Note on Publications

This thesis is "with publications" and the details of the publications are outlined below.

Note that there may be small inconsistencies in the notations because the chapters have been reproduced as accepted/submitted for publications. Also, there is a reference list at the end of each chapter.

Chapter 2: Published Online

Chen, Y., Ali, M., Shi, S., Cheang, U. Kei. (2019). Biosensing-by-Learning Direct Targeting Strategy for Enhanced Tumor Sensitization. *IEEE Transactions on Nanobioscience*, doi: 10.1109/TNB.2019.2919132. **(J1)**

Chapter 3: Published Online

Ali, M., Chen, Y., Cree, M. J. (2022). *In Vivo* Computation with Sensor Fusion and Search Acceleration for Smart Tumor Homing. *Elsevier Computers in Biology and Medicine*, doi: 10.1016/j.compbiomed.2022.105887. **(J2)**

Chapter 4: Published Online

Ali, M., Chen, Y., Cree, M. J. (2021). Autonomous In vivo Computation in Internet-of-Nano-Bio-Things. *IEEE Internet of Things Journal*, doi: 10.1109/JIOT.2021.3111089. **(J3)**

Chapter 5: Submitted

Ali, M., Chen, Y., Cree, M. J. (2022). Semi-Autonomous *In Vivo* Computation in Internet of Bio-Nano Things. Submitted in: *IEEE Internet of Things Journal*. **(J4)**

Conference Publications

1. Chen, Y., Ali, M., Shi, S., Cheang, U. Kei. (2019). "Direct Targeting Strategy for Smart Cancer Detection as Natural Computing". *53rd IEEE International Conference on Communications (ICC).* **(C1)**

2. Ali, M., Cree, M. J., Sharifi, N., Chen, Y. (2019). "Nanoswimmer-oriented Direct Targeting Strategy Inspired by Momentum-based Gradient Optimization". *41st Annual International Conference of the IEEE Engineering in Medicine and Biology Society (EMBC).* **(C2)**

3. Sharifi, N., Holmes, G., Zhou, Y., Ali, M., Chen, Y. (2019). "Overcoming Channel Uncertainties in Molecular-Communication-Inspired Direct Drug Targeting". *41st Annual International Conference of the IEEE Engineering in Medicine and Biology Society (EMBC).* **(C3)**

4. Ali, M., McGrath, N., Shi, S., Cree, M. J., Cheang, U. Kei, Chen, Y. (2020). "Bio-inspired Self-regulated In-vivo Computation for Smart Cancer Detection". *20th IEEE International Conference on Nanotechnology (NANO).* **(C4)**

5. Ali, M., Cree, M. J., Sharifi, N., Chen, Y. (2020). "Self-regulated and Coordinated Smart Tumor Homing for Complex Vascular Networks". *42nd Annual International Conference of the IEEE Engineering in Medicine and Biology Society (EMBC).* **(C5)**

6. Sharifi N., Ali, M., Holmes, G., Chen, Y. (2020). "Blind Obstacle Avoidance Using Taxicab Geometry for Nanorobot Assisted Direct Drug Targeting". *42nd Annual International Conference of the IEEE Engineering in Medicine and Biology Society (EMBC).* **(C6)**

7. Shi, S., Xiong, J., Ali, M., Chen, Y., Cheang, U. Kei, Kim, M. J., Yao, X. (2020). "Nanorobots-assisted Tumor Sensitization and Targeting for Multifocal Tumor". *20th IEEE International Conference on Nanotechnology (NANO).* **(C7)**

Acknowledgements

First of all, I would like to thank Almighty Allah for His blessings as nothing is possible without His help. Afterwards, I am heartily thankful to my parents, sisters and wife for supporting and praying for me throughout my research phase.

Upon the completion of my thesis, I am grateful to Professor Yifan Chen and Associate Professor Michael J. Cree for their consistent support and guidance. Their consummate supervision and valuable discussion from time to time helped me to keep going focused towards my goal. They assisted me while doing research, writing, submitting papers for publication, responding to reviewers' comments and finalising my thesis.

I am thankful to my father-in-law Professor Umar Farooq for his special support during my PhD journey. His expert suggestions and morale boosting discussions from time to time were really fruitful throughout my research. Special thanks to my colleague Dr. Atta Ullah who helped me in removing different bugs and errors which I encountered during coding in MATLAB. The lengthy ideas exploring discussions with him were also very helpful.

I am also grateful to the School of Engineering, Division of Health, Engineering, Computing and Science, the University of Waikato for providing me a nice, friendly, supportive and constructive environment to do the research.

Dedication

I dedicate this thesis to two very special ladies of my life i.e., my mother; for continuously praying for my success, and my wife; for supporting, motivating and helping me throughout this research phase.

Contents

List of Figures

List of Tables

Acronyms

AIVC autonomous *in vivo* computation.

AP autonomous phase.

ASSS autonomous swarm spot sampling.

BGF biological gradient field.

CdSe cadmium selenide.

CL centralized learning.

CM centralized movement.

DL decentralized learning.

DM decentralized movement.

DTS direct targeting strategy.

EPR enhanced permeability and retention.

EWF equal weighted fusion.

GD gradient descent.

HIVC hybrid *in vivo* computation.

IA intended actuation.

IT imaging and tracking.

IVC *in vivo* computation.

LCST lower critical solution temperature.

LSPE least-square-position-estimation.

MAS multi-agent systems.

MDGD memory-driven gradient descent.

MEF multi-estimate fusion.

MITs medical imaging techniques.

MIVC manipulable *in vivo* computation.

MLGD memory-less gradient descent.

MNPs magnetic nanoparticles.

MRI magnetic resonance imaging.

NS nanoswimmer.

NSs nanoswimmers.

OA optimization agent.

OAs optimization agents.

OR observing-and-recording.

OV optimization variable.

OVs optimization variables.

PWF proportional weighted fusion.

RP reinforcement phase.

SS swarm-steering.

TDM time-division multiplexing.

UA unintended actuation.

UCST upper critical solution temperature.

WHO World Health Organization.

Chapter 1

Introduction

Cancer remains one of the leading causes of human mortalities for the last few decades (Siegel et al.; 2017). According to World Health Organization (WHO), the annual number of cancer related deaths is 171.2 in every 100,000 people. WHO also projected that 13.1 million people would die from cancer in 2030 and approximately 39.6% of the world population will be diagnosed with cancer at some point during their lifetime. Two-third of the cancer associated deaths globally, can be saved through early detection and localization of cancer. Current medical imaging techniques such as magnetic resonance imaging (MRI), computed tomography and X-rays have resolution limitation and hence cannot detect small malignant tumors before clinical symptoms start to appear (Kasban et al.; 2015). Indeed with the finest modern-era instruments and methodologies, cancerous cells can go unnoticed for 10 years when they have ended up to be 50 million cancer cells strong (Hori and Gambhir; 2011).

Nanoparticles can be used as potential contrast agents which can provide better demarcation between healthy and diseased tissues (Malekzad et al.; 2017; Bucci

et al.; 2017). Detection of small tumors in hard-to-reach tissues and human body cavities may be performed through nanoparticles, possessing biosensing ability along with physical or chemical tumor-induced sensitivity. Nanobiosensing is an emerging technology with a huge potential in the area of biomedicine. One particular example of nanobiosensing is detection of biological targets such as early stage tumors. Nanoparticles or liposomes (Ferrari; 2005; Qian et al.; 2012) are getting huge interest from researchers as candidates for contrast agent in medical imaging techniques (Wen et al.; 2016). They can be used to detect small tumors before the process of metastasizing initiates. For example, CREKA-Tris (GD-DOTA)3 have been used in getting robust contrast enhancement by enabling the detection of small metastatic tumors ($<$0.5 mm).

Nanoparticles behave in different interesting ways in response to the biological changes happening in the peritumoral area. Therefore, understanding of the tumor environment is vital for successful and precise realization of early tumor detection. Previous studies demonstrate that the passive properties of peritumoral area change due to the presence of early malignant tumors (Sutherland; 1988). Tumor triggered biological gradients such as pH, temperature, enzyme reactions or redox potential are regarded as internal stimuli which can assist in tumor detection (Von Maltzahn et al.; 2011; Zhang et al.; 2016; Seidi et al.; 2018). Similarly external stimuli such as infrared, heat or light can be used to prime an environment around tumor (Kwon et al.; 2015).

The response of nanoparticles to the tumor induced biological gradients has helped to design nanoparticles which can be effectively used in medicine (Karimi et al.; 2016). For example, self-assembled miscelles transform from their normal state in a healthy tissue environment (pH = 7.4) to a swollen state in a tumoral

environment (pH = 6.8) (Li et al.; 2016). Similarly, temperature sensitive polymers such as PNIPAA undergo morphological transformations as a result of hypodermic nature of most malignant tumoral environments (Beija et al.; 2011). Multiple swarms of nanoparticles cooperate to find the targeted site by moving through the high-risk tissue. Consequently, engineered nanoparticles improve the success rate by orders of magnitude (Park et al.; 2010; Kim et al.; 2017; Overchuk and Zheng; 2018).

To sum up, nanoparticles can be injected into the blood stream to achieve contrast enhancement after their deposition on the tumorous site. They rely on human circulation system to reach the tumor and increase the resolution of imaging techniques like MRI through highlighting the diseased area.

1.1 Research Problem

The traditional targeting method used for the transportation of nanoparticles to the tumor is inefficient as it relies solely on human circulation system. From computational perspective, this systemic targeting is regarded as brute-force search where a large number of nanoparticles attempt to detect a tumor enumerating all possible pathways in the complex vascular network. Factors such as biodegradation, scattering and presence of mobile obstacles in the blood stream contribute to the loss of nanoparticles in the human vasculature. Statistical results from the past decade show that only 0.7% of the injected nanoparticles reach the target (Wilhelm et al.; 2016). This low percentage is a fundamental hurdle for bringing nanomedicines from the laboratory into the clinic.

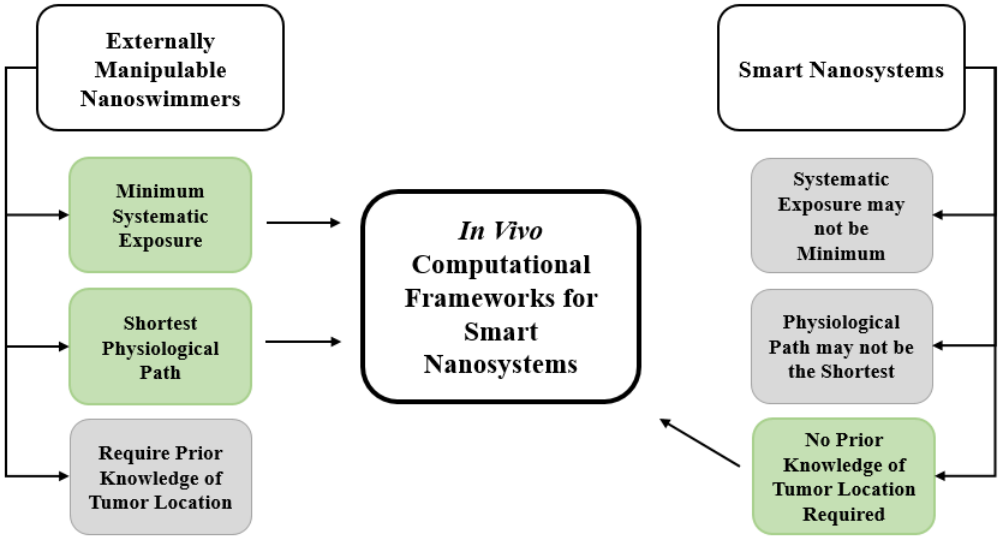

Figure 1.1: Basic features of proposed in vivo computational frameworks harvesting positive features (shown in green boxes) from both smart nanosystems and direct targeting employed by externally manipulable nanoswimmers whereas ignoring the limitations (shown in grey boxes) of both systems.

Replacing non-manipulable nanoparticles with swarm of externally manipulable nanoswimmers (NSs) may help in improving the delivery of contrast agents to the tumor (see left hand side of Fig. 1.1). Under such direct targeting strategy, external steering field is applied to guide NSs towards the tumor, hence requiring prior knowledge of the tumor location. This strategy improves the efficiency of getting NSs to the tumor (Felfoul et al.; 2016). However, it is not feasible to obtain precise knowledge of early tumor location through existing medical imaging techniques with limited imaging resolution.

Tumor homing capability of NSs can also be improved through smart nanosystems (see right hand side of Fig. 1.1) in which tumor microenvironment assists in target localization. NSs are either engineered to respond in a certain manner to host environment after their systemic injection or the peritumoral area is first

primed to interact with NSs to guide them towards the possible tumor location (Kwon et al.; 2015). Prior knowledge of tumor location is not required in both cases but the sensitization process still relies on systemic targeting. Therefore, the targeting process is slow with higher biodegradation of NSs as the physiological path taken by them may not be the shortest.

The aforementioned discussion demonstrates that significant amplification of tumor homing can be achieved by bringing into play the tumor-induced biological gradient field that interacts with the NSs for their subsequent target directed locomotion. To summarize, locomotion of the NSs towards an unknown tumor can be realized through an externally tracking and controlling system, an independent and self-regulated system, or a semi-autonomous hybrid system. We propose *in vivo* computational frameworks for these systems as illustrated in Fig. 1.2 and are outlined in the following methodology section. Such biosensing-by-learning nanosystems can help to immensely revolutionize the existing diagnostic and therapeutic techniques.

1.2 Research Methodology

Instead of complete dependence on systemic targeting, the current work proposes externally manipulable, self-regulatable, and semi-autonomous (hybrid) systems where engineered NSs replace non-manipulable nanoparticles for tumor homing. This research develops theoretical frameworks for tumor sensitization through manipulable *in vivo* computation (MIVC), autonomous *in vivo* computation (AIVC), and hybrid *in vivo* computation (HIVC), under the umbrella of computing-inspired bio-sensitization. In these frameworks, a computational agent (such as an NS) tries

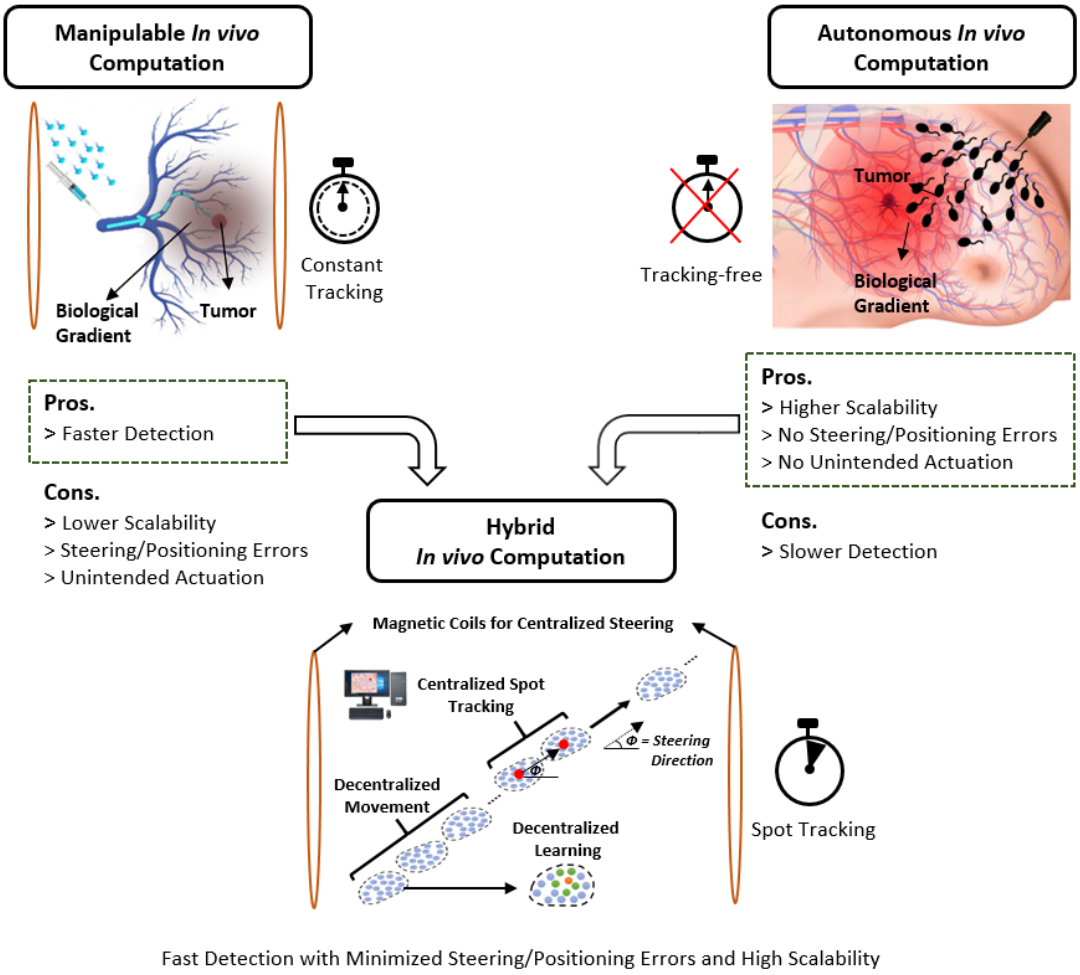

Figure 1.2: Proposed in vivo *computational frameworks for smart tumor sensitization.*

to find a target (such as the tumor) by iteratively moving through the search domain (such as the tissue region at a high risk of malignancy).

For externally manipulable computation, the tumor homing is achieved under the guidance of an external force (such as a magnetic field to steer NSs towards the possible tumor location). The approach uses the external controlling unit to track the observable characteristics of injected NSs to adopt the shortest physio-

logical path which ensures minimum systemic exposure when they search for an unknown tumor. Although external propulsion of NSs makes the tumor homing fast but this approach suffers from position and steering errors due to constrained accuracy of the external equipment. Moreover, *in vivo* tracking of a large number of NSs is challenging which limits the size of the swarm as highlighted in Fig. 1.2. Finally, the uniform magnetic field for the steering of swarm in single direction also introduces a constraint on the intended motion (based on the localized gradient estimate) of individual NS.

Interestingly, biological gradient-induced cooperation and collaboration among the swarm of NSs can also achieve successful target detection in autonomous computation. The stochastic (random) movements of NSs when allowed to aggregate and migrate together, result in target-directed locomotion. These gradient sensing NSs with minimum computation ability and no individual locomotion capability, perform tumor homing without the aid of any external equipment. Due to the inherent autonomous nature of NSs, this approach is not only highly scalable but also immune from steering and positioning errors as shown in Fig. 1.2. Nevertheless, as expected, the tumor sensitization is slow in the absence of an external driving force.

Finally, to further remove the limitations of the aforementioned nanosystems such as slow detection (in AIVC), positioning/steering errors, constant monitoring and unintended actuation (in MIVC), a semi-autonomous hybrid *in vivo* computation (HIVC) framework is proposed, where the scalable swarm of NSs, without the requirement of constant tracking, achieves faster tumor sensitization as shown in Fig. 1.2. The swarm senses the biological gradients and moves towards the target

autonomously, where an external unit is briefly used to fetch data (spot-tracking), required for much needed propulsion towards the target.

1.3 Contributions of the Thesis

In this thesis, different computational strategies are exploited to achieve fast, accurate and robust early tumor detection. The main contributions are as follows:

- A novel *MIVC* framework is proposed for nanobiosensing. In this framework, NSs assembled by magnetic nanoparticles are used to find the target by moving through the search domain under the influence of an external force (e.g., steering magnetic field).

- The aforementioned framework is associated with the limitations of natural computing such as uniform magnetic field, finite life span of nanoparticles and cytotoxicity. We address these constraints by using the multi-estimate fusion (MEF) and memory-driven gradient descent (MDGD) strategies and through maintaining swarm compactness.

- Next, the magnetic nanoparticles can be replaced with a swarm of self-regulatable NSs such as those built on the principle of particle robots by (Li et al.; 2019). Hence, we propose a parallel framework called *AIVC* for tumor homing. Under this framework, an analogy is presented between tumor sensitization through natural computation and autonomous multi-agent system (MAS). The AIVC framework is further analyzed by introducing real-world constraints such as noisy search domain and ever-existing mobile obstacles.

Such imperfections can reduce the efficiency of any target homing process. Hence, they are incorporated to verify the robustness of AIVC.

- Finally, the features of self-regulation and external manipulation are combined and a comprehensive HIVC framework for tumor homing is proposed. This framework overcomes the weaknesses of both MIVC (i.e., need of constant monitoring, low scalability, positioning and steering errors) and AIVC (i.e., slow detection of the target) through the autonomous swarm spot sampling (ASSS) strategy.

The thesis is organised as follows. In Chapter 2, we propose a novel iterative-optimization-inspired direct targeting strategy for smart nanosystems, which harness swarms of externally manipulable nanoswimmers assembled by magnetic nanoparticles for tumor sensitization and targeting. Chapter 3 focuses on resolving the real-life constraints of direct targeting strategy proposed in Chapter 2. Numerical experiments demonstrate that challenges of natural *in vivo* computation such as uniformity of magnetic field and finite life span of nanoswimmers can be solved by the proposed MEF and MDGD strategies respectively. Chapter 4 introduces a parallel framework of AIVC in which target detection is achieved through the swarm coordination, following the simple mechanism of aggregation and migration. Furthermore, in this chapter, reality checks of natural computing that may effect the system efficacy are discussed, providing a critical insight about the limitations of AIVC. Chapter 5 introduces HIVC resolving the key limitations of MIVC and AIVC. In Chapter 6, we provide the conclusion of our research work and some recommendations for future work. Fig. 1.3 gives a pictorial illustration of the thesis structure.

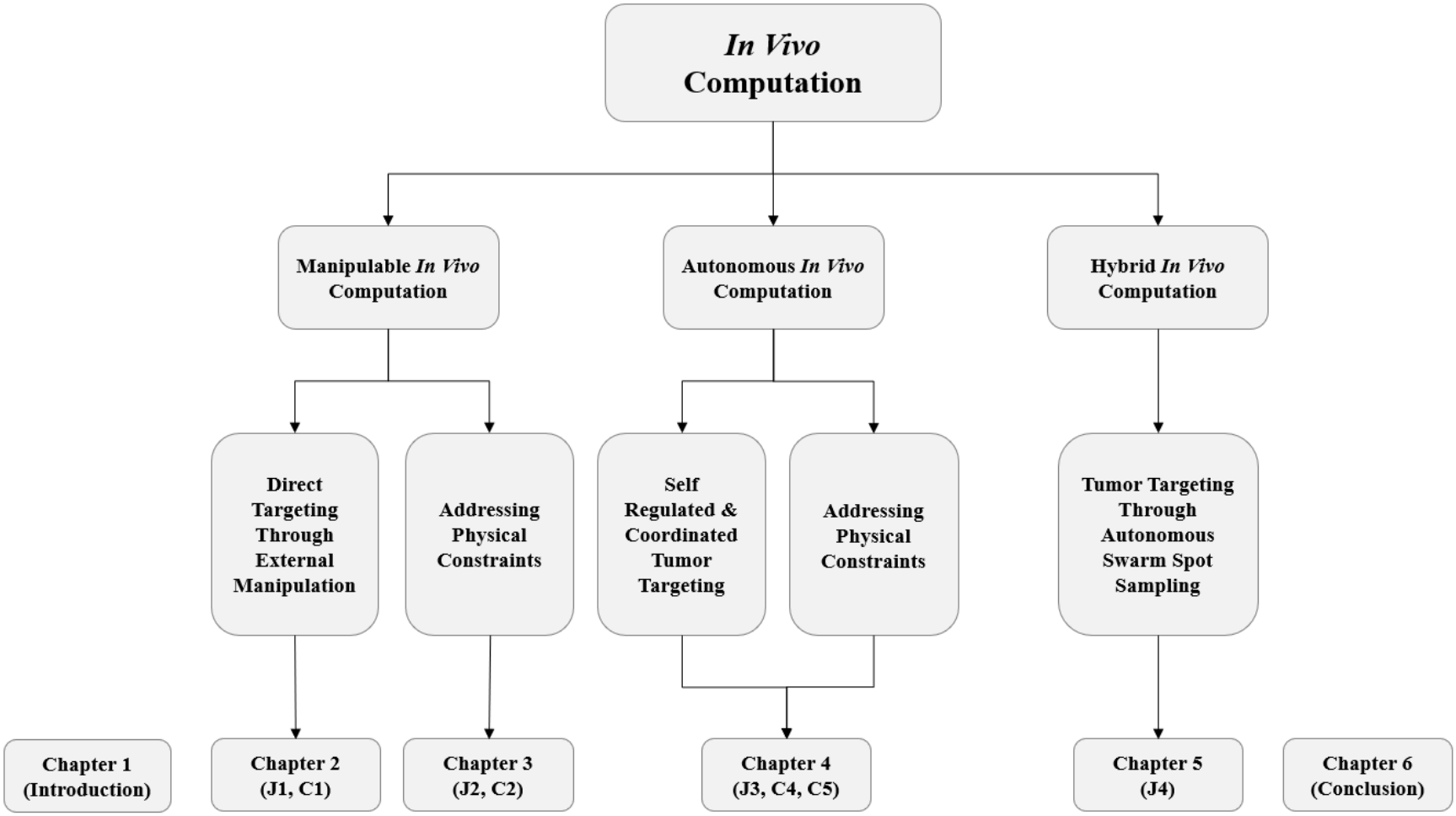

Figure 1.3: Pictorial representation of the thesis structure.

References

Beija, M., Marty, J.-D. and Destarac, M. (2011). Thermoresponsive poly (n-vinyl caprolactam)-coated gold nanoparticles: sharp reversible response and easy tunability, *Chemical Communications* **47**(10): 2826–2828.

Bucci, O. M., Bellizzi, G., Borgia, A., Costanzo, S., Crocco, L., Di Massa, G. and Scapaticci, R. (2017). Experimental framework for magnetic nanoparticles enhanced breast cancer microwave imaging, *IEEE Access* **5**: 16332–16340.

Felfoul, O. et al. (2016). Magneto-aerotactic bacteria deliver drug-containing nanoliposomes to tumour hypoxic regions, *Nat. Nanotechnol.* **11**(11): 941–947.

Ferrari, M. (2005). Cancer nanotechnology: opportunities and challenges, *Nature Reviews Cancer* **5**(3): 161–171.

Hori, S. S. and Gambhir, S. S. (2011). Mathematical model identifies blood biomarker–based early cancer detection strategies and limitations, *Science translational medicine* **3**(109): 109ra116–109ra116.

Karimi, M., Ghasemi, A., Zangabad, P. S., Rahighi, R., Basri, S. M. M., Mirshekari, H., Amiri, M., Pishabad, Z. S., Aslani, A., Bozorgomid, M. et al. (2016). Smart micro/nanoparticles in stimulus-responsive drug/gene delivery systems, *Chemical Society Reviews* **45**(5): 1457–1501.

Kasban, H., El-Bendary, M. and Salama, D. (2015). A comparative study of medical imaging techniques, *Int. J. Information Sci. Intelligent System* **4**: 37–58.

Kim, H., Lee, J., Oh, C. and Park, J.-H. (2017). Cooperative tumour cell membrane targeted phototherapy, *Nature Communications* **8**(1): 1–10.

Kwon, E. J., Lo, J. H. and Bhatia, S. N. (2015). Smart nanosystems: Bio-inspired technologies that interact with the host environment, *Proceedings of the National Academy of Sciences* **112**(47): 14460–14466.

Li, D., Ding, J., Zhuang, X., Chen, L. and Chen, X. (2016). Drug binding rate regulates the properties of polysaccharide prodrugs, *Journal of Materials Chemistry B* **4**(30): 5167–5177.

Li, S., Batra, R., Brown, D., Chang, H.-D., Ranganathan, N., Hoberman, C., Rus, D. and Lipson, H. (2019). Particle robotics based on statistical mechanics of loosely coupled components, *Nature* **567**(7748): 361–365.

Malekzad, H., Zangabad, P. S., Mirshekari, H., Karimi, M. and Hamblin, M. R. (2017). Noble metal nanoparticles in biosensors: recent studies and applications, *Nanotechnology Reviews* **6**(3): 301–329.

Overchuk, M. and Zheng, G. (2018). Overcoming obstacles in the tumor microenvironment: Recent advancements in nanoparticle delivery for cancer theranostics, *Biomaterials* **156**: 217–237.

Park, J.-H., von Maltzahn, G., Ong, L. L., Centrone, A., Hatton, T. A., Ruoslahti, E., Bhatia, S. N. and Sailor, M. J. (2010). Cooperative nanoparticles for tumor detection and photothermally triggered drug delivery, *Advanced Materials* **22**(8): 880–885.

Qian, W.-Y., Sun, D.-M., Zhu, R.-R., Du, X.-L., Liu, H. and Wang, S.-L. (2012). ph-sensitive strontium carbonate nanoparticles as new anticancer vehicles for controlled etoposide release, *International Journal of Nanomedicine* **7**: 5781.

Seidi, K., Neubauer, H. A., Moriggl, R., Jahanban-Esfahlan, R. and Javaheri, T. (2018). Tumor target amplification: implications for nano drug delivery systems, *Journal of Controlled Release* **275**: 142–161.

Siegel, R. L., Miller, K. D., Fedewa, S. A., Ahnen, D. J., Meester, R. G., Barzi, A. and Jemal, A. (2017). Colorectal cancer statistics, 2017, *CA: A Cancer Journal for Clinicians* **67**(3): 177–193.

Sutherland, R. M. (1988). Cell and environment interactions in tumor microregions: the multicell spheroid model, *Science* **240**(4849): 177–184.

Von Maltzahn, G., Park, J.-H., Lin, K. Y., Singh, N., Schwöppe, C., Mesters, R., Berdel, W. E., Ruoslahti, E., Sailor, M. J. and Bhatia, S. N. (2011). Nanoparticles that communicate in vivo to amplify tumour targeting, *Nature Materials* **10**(7): 545–552.

Wen, C.-Y., Xie, H.-Y., Zhang, Z.-L., Wu, L.-L., Hu, J., Tang, M., Wu, M. and Pang, D.-W. (2016). Fluorescent/magnetic micro/nano-spheres based on quantum dots and/or magnetic nanoparticles: preparation, properties, and their applications in cancer studies, *Nanoscale* **8**(25): 12406–12429.

Wilhelm, S., Tavares, A. J., Dai, Q., Ohta, S., Audet, J., Dvorak, H. F. and Chan, W. C. (2016). Analysis of nanoparticle delivery to tumours, *Nature Reviews Materials* **1**(5): 1–12.

Zhang, B., Wang, H., Shen, S., She, X., Shi, W., Chen, J., Zhang, Q., Hu, Y., Pang, Z. and Jiang, X. (2016). Fibrin-targeting peptide creka-conjugated multi-walled carbon nanotubes for self-amplified photothermal therapy of tumor, *Biomaterials* **79**: 46–55.

Chapter 2

Biosensing-by-learning Direct Targeting Strategy for Enhanced Tumor Sensitization

Objective: We propose a novel iterative-optimization-inspired direct targeting strategy (DTS) for smart nanosystems, which harness swarms of externally manipulable nanoswimmers assembled by magnetic nanoparticles (MNPs) for knowledge-aided tumor sensitization and targeting. We aim to demonstrate through computational experiments that the proposed DTS can significantly enhance the accumulation of MNPs in the tumor site, which serve as a contrast agent in various medical imaging modalities, by using the shortest possible physiological routes and with minimal systemic exposure.

Methods: The epicenter of a tumor corresponds to the global maximum of an externally measurable objective function associated with an *in vivo* tumor-triggered biological gradient; the domain of the objective function is the tissue region at a

high risk of malignancy; swarms of externally controllable magnetic nanoswimmers for tumor sensitization are modeled as the guess inputs. The objective function may be resulted from a passive phenomenon such as reduced blood flow or increased kurtosis of microvasculature due to tumor angiogenesis; otherwise, the objective function may involve an active phenomenon such as the fibrin formed during the coagulation cascade activated by tumor-targeted "activator" nanoparticles. Subsequently, the DTS can be interpreted from the iterative optimization perspective: guess inputs (i.e., swarms of nanoswimmers) are continuously updated according to the gradient of the objective function in order to find the optimum (i.e., tumor) by moving through the domain (i.e., tissue under screening). Along this line of thought, we propose the computational model based on the gradient descent (GD) iterative method to describe the GD-inspired DTS, which takes into account the realistic *in vivo* propagation scenario of nanoswimmers.

Results: By means of computational experiments, we show that the GD-inspired DTS yields higher probabilities of tumor sensitization and more significant dose accumulation compared to the "brute-force" search, which corresponds to the systemic targeting scenario where drug nanoparticles attempt to target a tumor by enumerating all possible pathways in the complex vascular network.

Conclusion: The knowledge-aided DTS has potential to enhance the tumor sensitization and targeting performance remarkably by exploiting the externally measurable, tumor-triggered biological gradients.

Significance: We believe that this work motivates a novel biosensing-by-learning framework facilitated by externally manipulable, smart nanosystems.

2.1 Introduction

2.1.1 Background

2.1.1.1 Contrast-enhanced Medical Imaging

Magnetic resonance imaging (MRI) is one of the standard procedures for non-invasive clinical diagnosis of cancers due to its high soft tissue contrast, spatial resolution, and penetration depth (Thoidingjam and Tiku; 2017). In addition, images are acquired without the use of ionizing radiation or radio tracers that would cause harmful side-effects. Contrast agents such as magnetic nanoparticles (MNPs) are commonly used in MRI to provide better delineation between healthy and diseased tissues (Thoidingjam and Tiku; 2017). Another promising modality for cancer diagnosis and recurrence monitoring is microwave imaging in view of its safety, mobility, and cost-effectiveness (Modiri et al.; 2017). For example, a number of operational microwave breast imaging systems are already in clinical use (Yang et al.; 2017; Song et al.; 2017; Porter et al.; 2016; Preece et al.; 2016; Meaney et al.; 2013) as reviewed in (O'Loughlin et al.; 2018, Early Access, DOI: 10.1109/TBME.2018.2809541). A major challenge faced by this approach is the potentially small dielectric contrast between tumor and its surrounding tissues, and between benign and cancerous changes (Lazebnik et al.; 2007; O'Rourke et al.; 2007; Semenov; 2009). To overcome these issues, MNPs have also been proposed as a contrast agent (Bucci et al.; 2017, 2015). However, the current systemic targeted drug delivery route can only deliver a very small fraction ($< 2\%$) of the administered nanoparticles to the precise site (Bae and Park; 2011). The main constraints include the reliance on systemic circulation, the lack of a propelling

force, and the absence of a sensory-based displacement capability (Felfoul et al.; 2016).

2.1.1.2 Amplification of Tumor Homing through Externally Manipulable Nanoswimmers

Enhancing the diagnostic efficacy of contrast agents necessitates the use of a direct targeting strategy (DTS) that allows agents to reach the target tissues using the shortest physiological routes and with minimal systemic exposure. In (Felfoul et al.; 2016), swarms of magneto-aerotactic bacteria, namely Magnetococcus marinus strain MC-1, are harnessed for delivering drug-containing nanoliposomes to the diseased site to improve the therapeutic index of various nanocarriers in tumor regions. MC-1 cells, each containing a chain of magnetic iron oxide nanocrystals, tend to swim along local magnetic field lines and towards low oxygen concentrations based on a two-state aerotactic sensing system. As shown in (Felfoul et al.; 2016), when MC-1 cells are injected near the tumor and magnetically guided, up to 55% of MC-1 cells can penetrate into hypoxic regions of the tumor, unlike the case for bacteria that are not guided into the tumor where only less than 10% of MC-1 cells can penetrate the xenograft. Furthermore, nanoswimmers assembled by MNPs have also been proposed for direct targeting, which use magnetic self-assembly of $50 - 100$ nm iron oxide nanoparticles (Cheang and Kim; 2015). Under an external magnetic field, the MNPs can magnetize and form chains that are flexible under time-varying magnetic fields *via* magnetohydrodynamics. A coil system has been designed to actuate the nanoswimmers by applying a nearly uniform magnetic field through the Helmholtz configuration (Cheang et al.; 2016, 2017). One common external force can control large numbers of nanoswimmers

to perform a complex task such as penetration of a tumor cell membrane for the selective release of a drug inside the cell (Cheang et al.; 2016; Mertz; 2018). However, nanoswimmers-assisted direct targeting of contrast agents requires *a priori* knowledge about the location of the diseased site, which is usually unavailable if the image quality is too low in the pre-contrast medical imaging. This results in a chicken-or-egg dilemma.

2.1.1.3 Amplification of Tumor Homing through Smart Nanosystems

Another strategy to amplify disease targeting is to design smart nanosystems that leverage the living host environment (Seidi et al.; 2018; Overchuk and Zheng; 2018; Kim et al.; 2017; Zhang et al.; 2016; Kwon et al.; 2015; von Maltzahn et al.; 2011; Park, von Maltzahn, Ong, Centrone, Hatton, Ruoslahti, Bhatia and Sailor; 2010; Agemy et al.; 2010; Park, von Maltzahnc, Xu, Fogald, Kotamraju, Ruoslahti, Bhatia and Sailor; 2010; Simberg et al.; 2007). These nanosystems can be classified in two categories: environment-responsive and environment-primed (Kwon et al.; 2015). The former category encompasses nanoparticles that sense and subsequently respond to their environment. Altered *in vivo* conditions such as redox potential, pH, enzymatic activity, and homeostatic pathways (see Fig. 1 in (Kwon et al.; 2015) for a comprehensive overview of various mechanisms) induced by disease conditions can be leveraged to mobilize nanoparticle systems that are administered in these preexisting contexts. The latter category is defined by an emerging paradigm of cooperative nanosystems, such that the host environment is manipulated by an external influence to enable desired host-nanoparticle and nanoparticle-nanoparticle interactions, such as communication, recruitment, or amplification. Modifications to the host that achieve this primed environment

can be accomplished by administering energy (X-rays, infrared light, heat), drugs, or nanoparticles themselves. For example, the nanosystem presented in (Park, von Maltzahnc, Xu, Fogald, Kotamraju, Ruoslahti, Bhatia and Sailor; 2010) consists of two components. The first component is gold nanorods that populate the porous tumor vessels *via* systemic targeting by utilizing the conventional enhanced permeability and retention (EPR) effect and then act as photothermal antennas to specify tumor heating *via* remote near-infrared laser irradiation. Local tumor heating accelerates the recruitment of the second component: a targeted nanoparticle consisting of either a prototypical imaging agent (magnetofluorescent iron oxide nanoworms) or a prototypical therapeutic agent (doxorubicin-loaded liposomes). Moreover, as shown in (von Maltzahn et al.; 2011), gold nanorods or engineered proteins can target tumors and then locally activate the coagulation cascade to broadcast tumor location to clot-targeted nanoworms or liposomes in circulation. Target amplification results in a more than 40 times increase in the amount of chemotherapeutic drug delivery to tumors compared with nanoparticles that cannot transmit controls. Smart nanosystems do not require location information of the diseased site. However, they still rely on systemic circulation for homing to cancer cells without using an external guidance.

2.1.2 Biosensing-by-learning DTS

The aforementioned experimental investigations that demonstrate significant amplification of tumor homing through either nanoswimmers (Felfoul et al.; 2016) or cooperative nanoparticles (von Maltzahn et al.; 2011) provide the basis for an externally manipulable, smart nanosystem, where non-manipulable nanoparticles

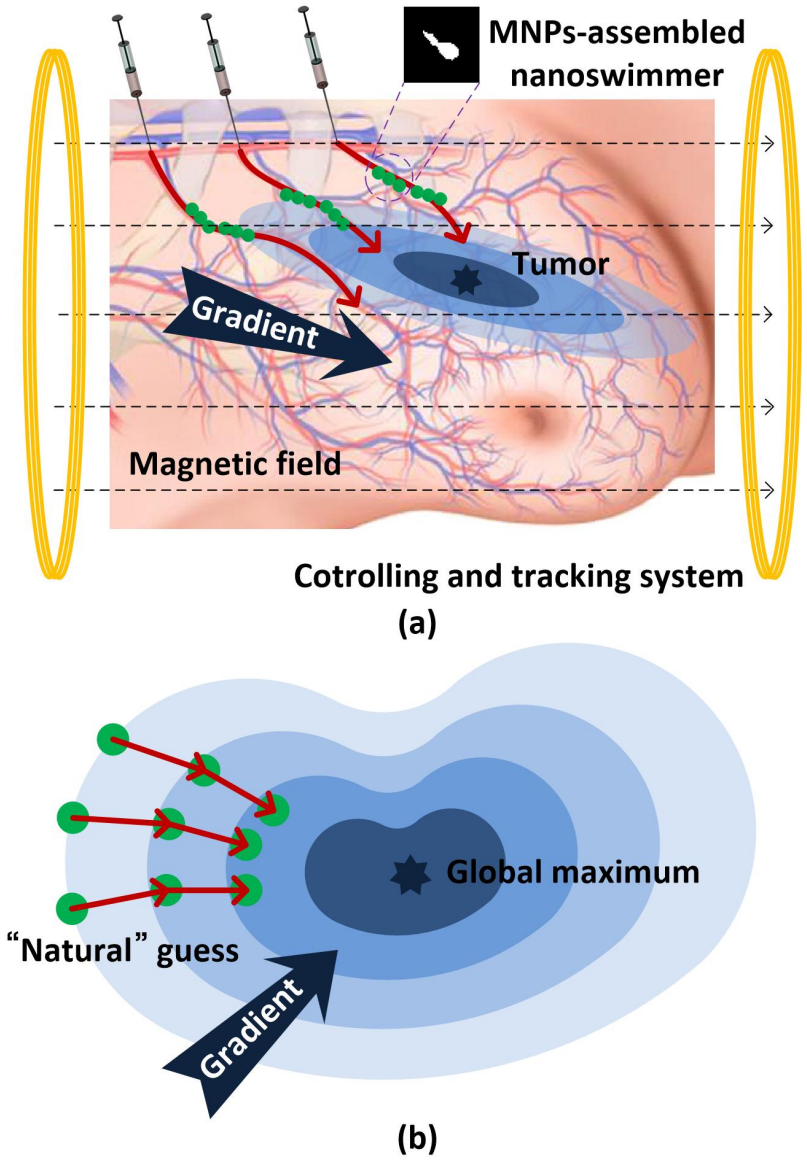

Figure 2.1: Analogy between (a) the proposed DTS employed in an externally manipulable, smart nanosystem for tumor sensitization, and (b) the iterative optimization process.

can be replaced by nanoswimmers assembled by iron oxide MNPs (Cheang and Kim; 2015), as depicted in Fig. 2.1(a). The magnetic response of MNPs, induced by a polarizing magnetic field, allows for reliable estimation of the locations of

magnetic changes through differential medical imaging (Bucci et al.; 2017, 2015). For environment-responsive operations, an external controlling and tracking system probes the host environment by analyzing the measurable characteristics of nanoswimmers (e.g., trajectories, magnetic changes induced) and steers them towards the direction where a tumor is likely to be present as shown in Fig. 2.1(a). For environment-primed operations, gold nanorods first prime the host environment (Park, von Maltzahn, Ong, Centrone, Hatton, Ruoslahti, Bhatia and Sailor; 2010; Park, von Maltzahnc, Xu, Fogald, Kotamraju, Ruoslahti, Bhatia and Sailor; 2010; von Maltzahn et al.; 2011) to interact with nanoswimmers. Similarly, the external system monitors the *in vivo* responses by observing the properties of nanoswimmers and maneuver them correspondingly to enhance tumor sensitization. Should a specific tissue region be a tumor, MNPs will accumulate in the region on the basis of the EPR effect or receptor-ligand binding, which can be observed externally by noticing that MNPs appear to stop moving (Chen et al.; 2017, 2016, Article ID 309703, 11 pages, http://dx.doi.org/10.1155/2013/309703).

The current investigation attempts to develop a computational model for feasibility study of the proposed knowledge-aided DTS. Nature's blueprints have inspired exciting new fields of science such as bio-inspired computing that creates problem-solving techniques using insights from natural systems. For example, the process of natural selection has inspired the development of the classical genetic algorithm to solve complex optimization and search problems. It is also stimulating to look the other way by exploiting computing strategies for biomedical applications (Chen et al.; 2016, 2017). There is an intriguing analogy between the proposed DTS in an externally manipulable nanosystem for tumor sensitization (Fig. 2.1(a)) and the iterative optimization process (Fig. 2.1(b)). The global max-

imum of a unimodal, externally measurable objective function corresponding to a tumor-induced biological phenomenon is the tumor to be detected; the domain of the function is the tissue region at a high risk of malignancy; the guess solution is a swarm of externally manoeuvrable magnetic nanoswimmers. A guess input (i.e., nanoswimmers) locates the optimal solution (i.e., cancer) by moving through the domain (i.e., high-risk tissue) under the guidance of a specified force (i.e., steering field). The objective function may be altered by the guess made of natural materials because the guess input interacts with the domain (i.e., nanoswimmers undergo physical, chemical, and biological interactions with the host environment). This is in contrast to a traditional iterative method using a non-interacting approximate solution. An external observer can then infer the domain by monitoring the movement of the guess ("seeing-is-sensing" (Chen et al.; 2016)), where the $(n+1)^{\text{th}}$ approximation is derived from the n^{th} one. This strategy is within the general framework of computing-inspired bio-detection proposed in our previous work (Chen et al.; 2017). Provided with the analogy, a wide variety of iterative methods can thus be applied to the design of an optimal DTS. To elaborate on the proposed methodology, the classical gradient descent (GD) method is used to inspire the DTS, where the guess input takes steps based on the gradient of the objective function at the current point. Furthermore, the derivative of the function needs to be approximated in real-time and the movement of the guess is constrained by the physical conditions of human microvasculature.

It is worth noting that, from the computational perspective, the traditional systemic delivery of contrast agents can be regarded as a "brute-force" search where a large number of contrast agent nanoparticles attempt to detect a tumor *via* a medical imaging system by enumerating all possible pathways in the

complex vascular network and checking whether each pathway is intercepted by a tumor. Furthermore, the original smart nanosystems in (Seidi et al.; 2018; Overchuk and Zheng; 2018; Kim et al.; 2017; Zhang et al.; 2016; Kwon et al.; 2015; von Maltzahn et al.; 2011; Park, von Maltzahn, Ong, Centrone, Hatton, Ruoslahti, Bhatia and Sailor; 2010; Agemy et al.; 2010; Park, von Maltzahnc, Xu, Fogald, Kotamraju, Ruoslahti, Bhatia and Sailor; 2010; Simberg et al.; 2007) can be regarded as a brute-force search given an *expanded* tumoral region due to tumor target amplification facilitated by the peritumoral biological conditions (for environment-responsive nanosystems) or the initial-stage triggering modules (for environment-primed nanosystems).

2.1.3 Organization of the Chapter

The chapter is organized as follows. In Section 2.2, we discuss some suitable *in vivo* biological gradients that can be mapped to externally measurable objective functions for the proposed DTS. In Section 2.3, we analyze the propagation model of nanoswimmers in a discretized capillary network. This is followed by discussion on the general iterative DTS framework including some representative objective functions showing different situations that the DTS has to face and the computational framework in Section 2.4. In Section 2.5, we propose the GD-inspired DTS subject to the realistic physical constraints of controlling and tracking nanoswimmers *in vivo*, based on the general problem setting in Section 2.4. In Section 2.6, we provide numerical examples to demonstrate the effectiveness of the proposed strategy. Finally, some concluding remarks are drawn in Section 2.7.

2.2 In Vivo Biological Gradients for Proposed DTS

In the current work, tumor sensitization is performed indirectly through an external controlling and tracking system as shown in Fig. 2.1(a), such as an integrated device consisting of multiple pairs of electromagnetic coils to generate the rotating magnetic field to actuate the magnetic nanoswimmers (Cheang et al.; 2016, 2017) and another coil to supply the polarizing magnetic field inducing the magnetic contrast associated with the nanoswimmers (Bucci et al.; 2017, 2015). Therefore, it is necessary that the *in vivo* biological gradients can be mapped to an externally measurable objective function by using nanoswimmers as a probe for analysis of the host environment.

2.2.1 Environment-responsive Nanosystems

For this type of nanosystems, passive physical properties of the host environment such as peritumoral vascular architecture (Gazit et al.; 1995; Baish et al.; 1996; Baish and Jain; 2000) and blood flow velocity (Fukumura and Jain; 2007; Wang et al.; 2009; Baish et al.; 1996; Komar et al.; 2009) can be exploited to derive the biological gradients. Oxygen and nutrients are supplied to cancer cells *via* new blood vessels that have extended into the cancer tissue. Typical skeletonized images of various classes of vascular networks demonstrate that normal capillaries exhibit almost uniformly distributed grid patterns to ensure adequate oxygen transportation throughout the tissue (Gazit et al.; 1995; Baish et al.; 1996; Baish and Jain; 2000). On the other hand, tumor vessels have a profound sort of tortuosity with many smaller bends on each larger bend (Gazit et al.; 1995; Baish et al.; 1996; Baish and Jain; 2000). In terms of blood flow velocity, its value in

tumor tissues is significantly lower than that in healthy tissues due to the hypovascular structure of the malignant lesion (Komar et al.; 2009; Fukumura and Jain; 2007). This phenomenon has been observed for cancer cells in the visceral pleura (Wang et al.; 2009), malignant gliomas (Baish et al.; 1996), and pancreatic tumors (Komar et al.; 2009). In summary, the externally measurable objective functions corresponding to the aforementioned two biological conditions can be derived from the variation in tortuosity of nanoswimmer trajectory and the variation in nanoswimmer velocity, respectively, with respect to the values for normal tissues. Both of them would increase as the distance between the nanoswimmer and the tumor decreases.

2.2.2 Environment-primed Nanosystems

For this type of systems, specific "activator" nanomaterials can be used to detect a diseased site and act as tumor-specific triggers to induce biological gradients. For example, gold nanorods can be modified to circulate for long periods of time in the blood stream and be passively accumulated in tumors *via* systemic circulation (Park, von Maltzahn, Ong, Centrone, Hatton, Ruoslahti, Bhatia and Sailor; 2010; Park, von Maltzahnc, Xu, Fogald, Kotamraju, Ruoslahti, Bhatia and Sailor; 2010; von Maltzahn et al.; 2011). They are used to heat tumor tissues by amplifying the absorption of near-infrared energy that is mostly transparent to living tissues (Park, von Maltzahn, Ong, Centrone, Hatton, Ruoslahti, Bhatia and Sailor; 2010; Park, von Maltzahnc, Xu, Fogald, Kotamraju, Ruoslahti, Bhatia and Sailor; 2010; von Maltzahn et al.; 2011). The associated photothermal heating is highly localized around the tumor site. Consequently, the gradient of blood flow velocity is

amplified due to the differential response of normal and tumor microcirculation to hyperthermia, where blood flow in normal tissue increases much faster with temperature and stasis occurs at higher levels of hyperthermia compared to tumors owning to the rapid growth of tumor cell population relative to deteriorating vascular beds (Dudar and Jain; 1984; Song; 1984). Furthermore, local heating disrupts tumor vessels and initiates extravascular coagulation. Hence, the fibrin forms the coagulation gradient centered at the tumor caused by temperature increase. The magnetic nanoswimmers employ the peptide coatings that recognize fibrin directly for clot targeting (Park, von Maltzahn, Ong, Centrone, Hatton, Ruoslahti, Bhatia and Sailor; 2010; Park, von Maltzahnc, Xu, Fogald, Kotamraju, Ruoslahti, Bhatia and Sailor; 2010; von Maltzahn et al.; 2011). Direct binding in regions of coagulation will reduce the concentration of mobile nanoswimmers under tracking. In summary, the externally measurable objective functions associated with the aforementioned two phenomena can be derived from the variation in nanoswimmer velocity and the variation in magnetic contrast induced by nanoswimmers, respectively, with respect to the values for normal tissues. Both of them would increase as the distance between the nanoswimmer and the tumor decreases. In addition, local hyperthermia results in a temperature gradient from the tissue malignancy to its peripheral region, which may be directly measured from the infrared thermographic imaging if the tumor is close to the skin (Park, von Maltzahn, Ong, Centrone, Hatton, Ruoslahti, Bhatia and Sailor; 2010; Park, von Maltzahnc, Xu, Fogald, Kotamraju, Ruoslahti, Bhatia and Sailor; 2010; von Maltzahn et al.; 2011). In this case, the global gradient towards the tumor epicenter can be readily obtained.

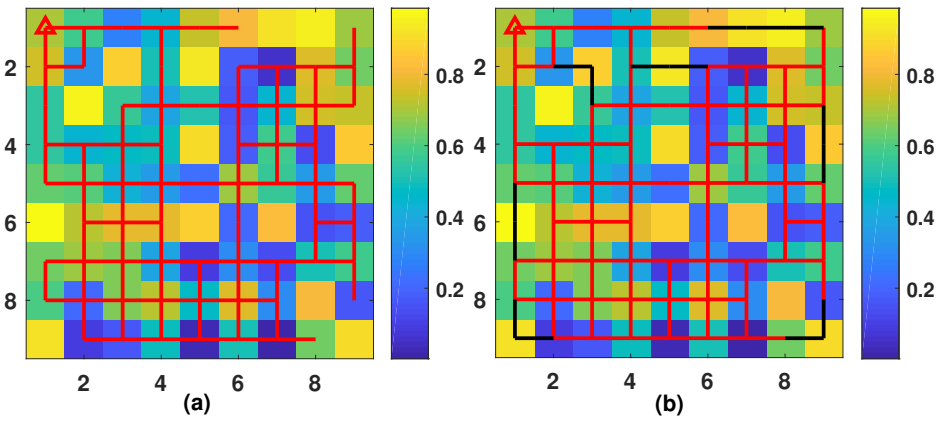

Figure 2.2: (a) An invasion percolation network after 100 growth steps, and (b) adding vessels to ensure nonzero blood flow throughout the network.

2.3 Vascular Network Model for Proposed DTS

Tumor vasculature is more chaotic in appearance than normal vasculature, which can be measured using fractal geometries (Baish and Jain; 2000). For example, tumor vessels yield fractal dimensions of 1.89 ± 0.04, whereas normal arteries and veins yield dimensions of 1.70 ± 0.03, and normal capillaries produce essentially two-dimensional patterns (Gazit et al.; 1995; Baish et al.; 1996; Baish and Jain; 2000). It was also observed that the microvascular density in the peritumoral region increases due to the supply of growth factors from the tumor and reduces in the tumor center due to a combination of severely reduced blood flow and solid stress exerted by the tumor (Lee et al.; 2006).

Consequently, it is assumed that normal tissues are regularly vascularized, which results in a homogeneous lattice comprised of straight, rigid cylindrical capillaries that join adjacent nodes (McDougall et al.; 2002; Baish et al.; 1996). On the other hand, the observed fractal dimensions of tumor vasculature can be

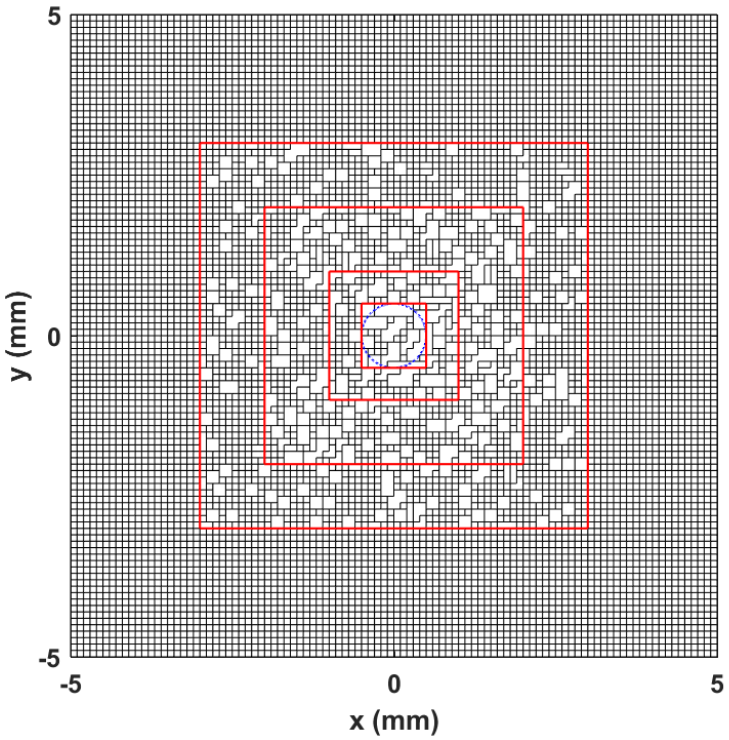

Figure 2.3: Simulated multi-layer vascular network. The level of occupancy on the lattice reduces from 100% *to* 40% *gradually as the distance to the tumor center (denoted by the blue dotted circle) decreases. The boundaries of the layers are denoted by the red solid lines.*

described by the invasion percolation process (Gazit et al.; 1995; Baish et al.; 1996; Baish and Jain; 2000), which is implemented by first assigning uniformly distributed random values of strengths to each point on the underlying square lattice representing potential paths of vascular growth. Starting at an arbitrary site the network occupies the lattice point adjacent to the current site that has the lowest strength. Growth is iterated until the desired lattice occupancy is reached. Blood vessels are assumed to connect all adjacent occupied lattice points. Finally, additional edges are added to "pathological" nodes to ensure nonzero blood

flow throughout the entire percolation cluster. The simulated networks may be matched with real tumor vasculature by selecting appropriate occupancy levels. Following (Baish et al.; 1996), the fractal dimensions are around 1.6, 1.8, 1.9, and 2.0 for 40, 60, 80, and 100% occupancy on the backbone, respectively.

Moreover, malignant tumors often possess fuzzy and blurred boundaries (Rangayyan et al.; 1997; Saunders et al.; 2006). As such, the fractal dimensions across the boundary of a tumor can be characterized by a smooth transition from inside a tumor to the outside. To quantify the diffusive nature of a tissue anomaly, a discretized multilayer model can be applied to approximate the gradual, continuous change in the fractal dimension across the periphery of a lesion. Fig. 2.2(a) depicts an invasion percolation network after 100 growth steps, and Fig. 2.2(b) shows additional vessels to ensure nonzero blood flow throughout the network assuming that the blood inflow and outflow are in the upper-left and lower-right corners, respectively. Fig. 2.3 illustrates a simulated multilayer vascular network, where the intercapillary distance is set to be 100 μm, and the level ofoccupancy on the lattice reduces from 100% to 40% gradually as the distance to the tumor center decreases.

2.4 Formulation of Proposed DTS

2.4.1 Externally Measurable Objective Function

Let f represent an externally measurable objective function and be defined on the domain $\mathbb{D}$, which denotes the high-risk tissue region under surveillance. The landscape of f is distorted by a "natural" guess G representing a swarm of magnetic

nanoswimmers as follows

$$\begin{aligned} f\left(\vec{x};G\right) &= f_{\mathrm{A}}\left(\vec{x};G\right) + f_{\mathrm{C}}\left(\vec{x};G\right) \\ &= f_{\mathrm{T}}(\vec{x}) + f_{\mathrm{D}}\left(\vec{x};G\right) + f_{\mathrm{C}}\left(\vec{x};G\right), \quad \vec{x} \in \mathbb{D}, \end{aligned} \tag{2.1}$$

where $f_{\mathrm{A}}\left(\vec{x};G\right)$ is the *apparent* objective function measured at location $\vec{x}$ through guess G, $f_{\mathrm{T}}(\vec{x})$ is the *true* objective function at $\vec{x}$ independent of the presence or absence of G, $f_{\mathrm{D}}\left(\vec{x};G\right)$ is the disturbance resulted from the interaction between G and the domain $\mathbb{D}$, and $f_{\mathrm{C}}\left(\vec{x};G\right)$ is the correction factor accounting for the disturbance caused by G. For a meaningful optimization process, it is assumed that regardless of any variation caused by the guess to the function, the location of the global maximum denoting the tumor, $\vec{x}^{\star}$, remains unchanged.

The true objective $f_{\mathrm{T}}(\vec{x})$, dependent on the underlying tumor-triggered biological phenomena, may take the form of variation in path tortuosity, nanoswimmer velocity, or magnetic contrast induced by nanoswimmers as discussed earlier. Subsequently, for the measure of tortuosity, an alteration $f_{\mathrm{D}}(\vec{x};G)$ would incur if the nanoswimmers are engineered to modify the vasculature of tumors (e.g., anti-angiogenic agents to shut down tumor vessels or pro-angiogenic agents to normalize tumor vessels) (Kwon et al.; 2015). For the measure of velocity, $f_{\mathrm{D}}(\vec{x};G)$ is given by the relative velocity of nanoswimmers with respect to the blood stream. In the case of magnetic change, $f_{\mathrm{D}}(\vec{x};G)$ is proportional to the reduction in the concentration of nanoswimmers due to various loss mechanisms such as degradation (nanoswimmers degenerate in the blood), branching (nanoswimmers move into an unintended vascular branch), and diffusion (random motions of nanoswimmers driven by the concentration gradient) (Chen et al.; 2015). Finally, the correc-

tion factor $f_{\mathrm{C}}(\vec{x};G)$ attempts to counteract $f_{\mathrm{D}}(\vec{x};G)$ to minimize its influence on the true landscape, i.e., $f_{\mathrm{C}}(\vec{x};G) = -f_{\mathrm{D}}(\vec{x};G) + \chi(\vec{x};G)$ with $\chi(\vec{x};G)$ being the random compensation error. Therefore, (2.1) can be rewritten as

$$f(\vec{x};G) = f_{\mathrm{T}}(\vec{x}) + \chi(\vec{x};G), \quad \vec{x} \in \mathbb{D}. \tag{2.2}$$

As the research is in its early stage, there is no widely-accepted, quantitative model on any of the aforementioned biological gradients in the existing literature other than some qualitative observations made from experimental data. As an initial investigation, three representative objective functions are considered as shown in Fig. 2.4. The maximum value is normalized to 1 and the minimum value is 0. The search domain is -5 mm $\leq x, y \leq 5$ mm. The landscapes are:

1. *Sphere Function (Bowl-shaped):*

$$f(x,y) = \begin{cases} 1, & \sqrt{x^2+y^2} \leq 0.5 \text{ and } (x,y) \in \mathbb{V} \\ 1 - 0.02\,(x^2+y^2), & \\ & \sqrt{x^2+y^2} > 0.5 \text{ and } (x,y) \in \mathbb{V}. \end{cases} \tag{2.3}$$

2. *Matyas Function (Plate-shaped):*

$$f(x,y) = \begin{cases} 1, & \sqrt{x^2+y^2} \leq 0.5 \text{ and } (x,y) \in \mathbb{V} \\ 1 - 0.01\,(x^2+y^2) + 0.02xy, & \\ & \sqrt{x^2+y^2} > 0.5 \text{ and } (x,y) \in \mathbb{V}. \end{cases} \tag{2.4}$$

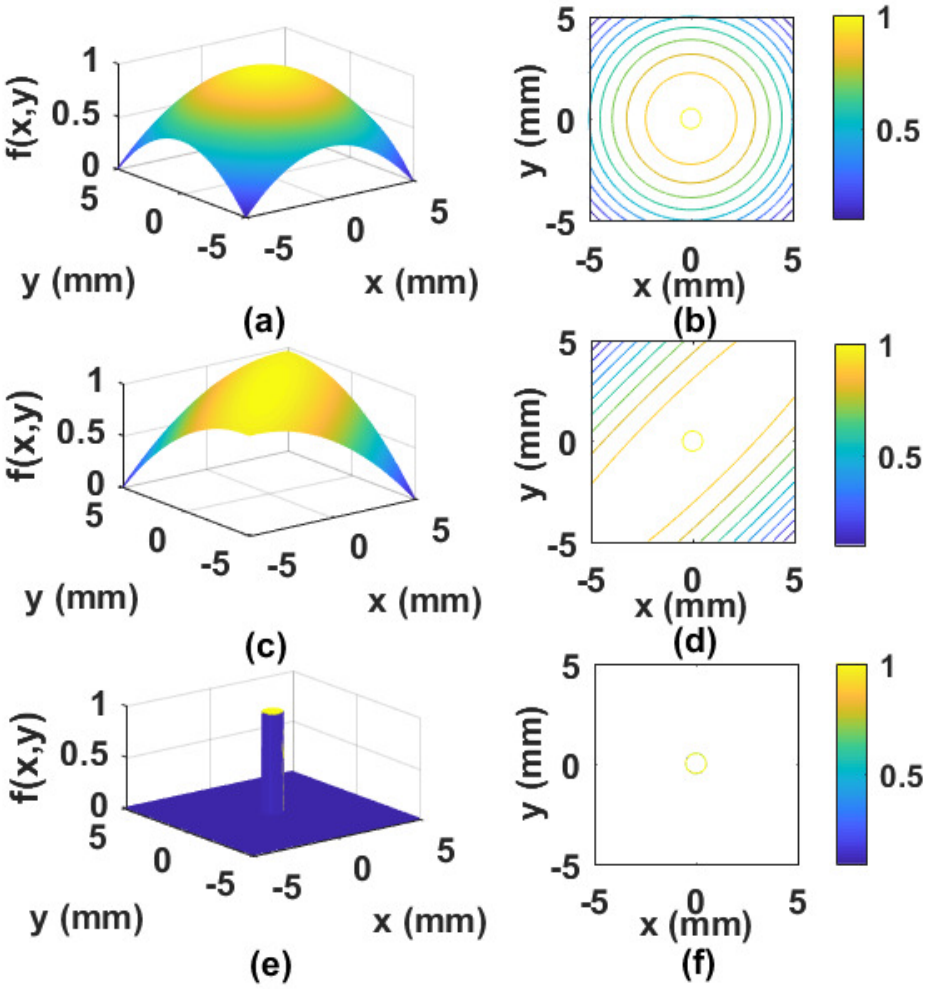

Figure 2.4: Illustration of $f(x, y)$ for three representative objective functions: (a) Sphere function and (b) its contour plot; (c) Matyas function and (d) its contour plot; (e) Easom function and (f) its contour plot. For the objective $f(x, y)$, the maximum is normalized to 1 and the minimum value is 0.

3. *Easom function:*

$$f(x,y) = \begin{cases} 1, & \sqrt{x^2+y^2} \leq 0.5 \text{ and } (x,y) \in \mathbb{V} \\ 0.01 + 0.99\cos(3x)\cos(3y) & \\ \qquad \times \exp\left[-\left(9x^2+9y^2\right)\right], & \\ & \sqrt{x^2+y^2} > 0.5 \text{ and } (x,y) \in \mathbb{V}. \end{cases} \tag{2.5}$$

The term $\mathbb{V}$ denotes the discrete vascular network as illustrated in Fig. 2.3. As shown in Fig. 2.4(a)-(b), both the Sphere and Matyas functions represent the situation that the tumor center, denoted by a circle of radius 0.5 mm located at the origin, is associated with the region having the highest values of $f(x, y)$. This may correspond to the largest (normalized) variation of blood flow velocity due to tumor angiogenesis or the largest (normalized) magnetic change induced by nanoswimmers due to fibrin tropism in tumor tissues. Both the functions are convex and quadratic. They have no local minimum except the global one. On the other hand, the Easom function in Fig. 2.4(c) represents the situation that $f(x, y)$ remains more or less unchanged across a large surveillance region. The tumor center yields an abrupt increase of $f(x, y)$. Intuitively, this may represent the worst-case direct targeting scenario due to the lack of an externally observable biological gradient.

In the absence of detailed information on the diameters of vessels, the viscosity of blood, and the applied blood pressure for tumor vessels and normal capillaries near the tumor, we simply imprint the objective functions on the vascular network $\mathbb{V}$ such that the values of the functions are only defined on the domain $\mathbb{V}$ as shown in (2.3)-(2.5). The blood inflow and outflow are assumed to be in the lower-left and upper-right corners, respectively, where prescribed pressures are set.

2.4.2 Computation Framework

The proposed DTS starts with multiple guess inputs $G_1, G_2, \cdots, G_N$ being deployed in multiple pre-specified sites $\mathbb{R}_1, \mathbb{R}_2, \cdots, \mathbb{R}_N \subseteq \mathbb{D}$, where $\mathbb{R}_n$ $(n = 1, 2, \cdots, N)$ denote the injection sites of nanoswimmers as depicted in Fig. 2.1. The guesses

begin searching for the optimal solution following some iterative algorithms. The computational framework includes the following key steps.

1. *Initialization.* The guess inputs are deployed in $\mathbb{R}_1, \mathbb{R}_2, \cdots, \mathbb{R}_N$ at the same starting times $t_{\mathrm{IA},1}^{(1)}$ as shown in Fig. 2.5(a)-(b) with initial locations $\vec{x}_1\left(t_{\mathrm{IA},1}^{(1)}\right)$, $\vec{x}_2\left(t_{\mathrm{IA},1}^{(1)}\right), \cdots, \vec{x}_N\left(t_{\mathrm{IA},1}^{(1)}\right)$, respectively. The superscript and subscript of the variable t correspond to the index of the current iteration and the index of the guess in a specified operational mode, respectively. Suppose that the external system operates in the simple time-multiplexed manner. Without loss of generality, consider the first guess input G_1, which operates on the following three modes: Intended Actuating (IA), Imaging and Tracking (IT), and Unintended Actuating (UA). Two time-division multiplexing (TDM) protocols are considered. For TDM1 each guess takes turn to operate in the IA and IT modes, whereas for TDM2 each guess takes turn to operate in the IA mode, followed by a common IT mode as illustrated in Fig. 2.5(a) and 2.5(b), respectively.

2. *IA.* For TDM1, from $t_{\mathrm{IA},1}^{(1)}$ to $t_{\mathrm{IT},1}^{(1)}$, G_1 operates in the IA mode and its trajectory is determined by the angle deviation relative to a principal axis denoting an intended steering vector upon G_1 at $\vec{x}_1\left(t_{\mathrm{IA},1}^{(1)}\right)$, $\phi\left(t_{\mathrm{IA},1}^{(1)}\right)$, which indicates a uniform magnetic field in the surveillance domain (Cheang et al.; 2016, 2017) and is dependent on the specific iterative method under consideration (e.g., the GD-inspired DTS in Section 2.5). The next location of G_1 at time

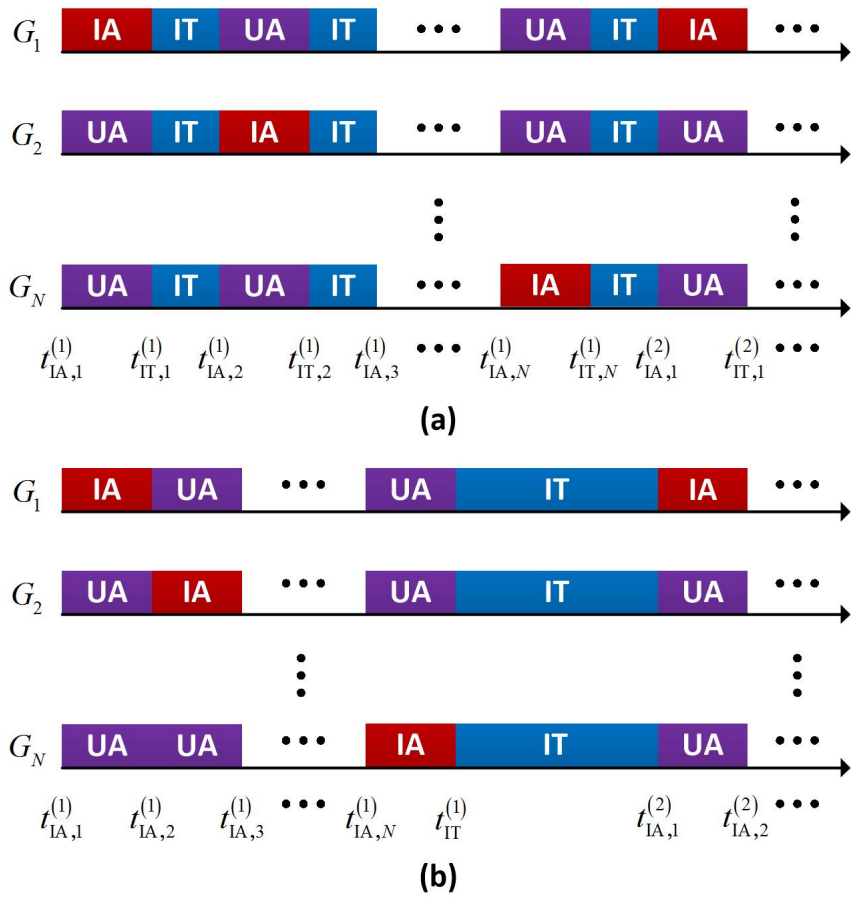

Figure 2.5: Time sequence of system operational modes in one cycle for multiple guess inputs. Each guess has three operational modes: Intended Actuating (IA), Imaging and Tracking (IT), and Unintended Actuating (UA). Two time-division multiplexing (TDM) protocols are considered. (a) TDM1: each guess takes turn to operate in the IA and IT modes; and (b) TDM2: each guess takes turn to operate in the IA mode, followed by a common IT mode.

instant $t^{(1)}_{\mathrm{IT},1}$ is then updated according to:

$$\begin{aligned}&\vec{x}_1\left(t^{(1)}_{\mathrm{IT},1}\right)\\&=\vec{x}_1\left(t^{(1)}_{\mathrm{IA},1}\right)+d_1\left(t^{(1)}_{\mathrm{IA},1}\right)\vec{u}_{\angle\left[\phi\left(t^{(1)}_{\mathrm{IA},1}\right)+\Delta\phi\left(t^{(1)}_{\mathrm{IA},1}\right)\right]}\\&\quad+\vec{q}_1\left(t^{(1)}_{\mathrm{IA},1}\right).\end{aligned}\tag{2.6}$$

The term $\vec{u}_{\angle\phi}$ denotes a unit vector with angle ϕ and $\Delta\phi\left(t_{\mathrm{IA},1}^{(1)}\right)$ is a random variable summarizing all steering imperfections, which is assumed to be normally distributed with variance $\sigma_{\Delta\phi}^2$ and zero mean for simplicity. The displacement length $d_1\left(t_{\mathrm{IA},1}^{(1)}\right)$ satisfies

$$\begin{aligned}
&\left\| d_1\left(t_{\mathrm{IA},1}^{(1)}\right)\vec{u}_{\angle\left[\phi\left(t_{\mathrm{IA},1}^{(1)}\right)+\Delta\phi\left(t_{\mathrm{IA},1}^{(1)}\right)\right]}\right\|_1 \\
&= \left| d_1\left(t_{\mathrm{IA},1}^{(1)}\right)\cos\left[\phi\left(t_{\mathrm{IA},1}^{(1)}\right)+\Delta\phi\left(t_{\mathrm{IA},1}^{(1)}\right)\right]\right| \\
&\quad + \left| d_1\left(t_{\mathrm{IA},1}^{(1)}\right)\sin\left[\phi\left(t_{\mathrm{IA},1}^{(1)}\right)+\Delta\phi\left(t_{\mathrm{IA},1}^{(1)}\right)\right]\right| \\
&= v_1\left(t_{\mathrm{IA},1}^{(1)}\right)\left(t_{\mathrm{IT},1}^{(1)}-t_{\mathrm{IA},1}^{(1)}\right),
\end{aligned} \tag{2.7}$$

where $\|\cdot\|_1$ denotes the ℓ_1 norm and $v_1\left(t_{\mathrm{IA},1}^{(1)}\right)$ is the velocity of G_1 at $t_{\mathrm{IA},1}^{(1)}$ given the taxicab geometry of the vascular network. Finally, $\vec{q}_1\left(t_{\mathrm{IA},1}^{(1)}\right)$ is the position "quantization" error due to the discrete lattice pattern of the vasculature as illustrated in Fig. 2.6, which is the displacement vector from the point $\vec{x}_1\left(t_{\mathrm{IA},1}^{(1)}\right)+d_1\left(t_{\mathrm{IA},1}^{(1)}\right)\vec{u}_{\angle\left[\phi\left(t_{\mathrm{IA},1}^{(1)}\right)+\Delta\phi\left(t_{\mathrm{IA},1}^{(1)}\right)\right]}$ on the continuous taxicab circle of radius $v_1\left(t_{\mathrm{IA},1}^{(1)}\right)\left(t_{\mathrm{IT},1}^{(1)}-t_{\mathrm{IA},1}^{(1)}\right)$, to its closest point in the discrete vascular network having the same taxicab distance to $\vec{x}_1\left(t_{\mathrm{IA},1}^{(1)}\right)$.

For TDM2, the same process as mentioned above applies except that $t_{\mathrm{IT},1}^{(1)}$ is replaced by $t_{\mathrm{IA},2}^{(1)}$ as shown in Fig. 2.5(b).

3. *IT*. For TDM1, from $t_{\mathrm{IT},1}^{(1)}$ to $t_{\mathrm{IA},2}^{(1)}$, G_1 operates in the IT mode. In the absence of a steering field, G_1 follows a random walk in the lattice (i.e., at each intersection it has the same probability to either move up or to the right) and swims towards various locations in equal observation time intervals along a

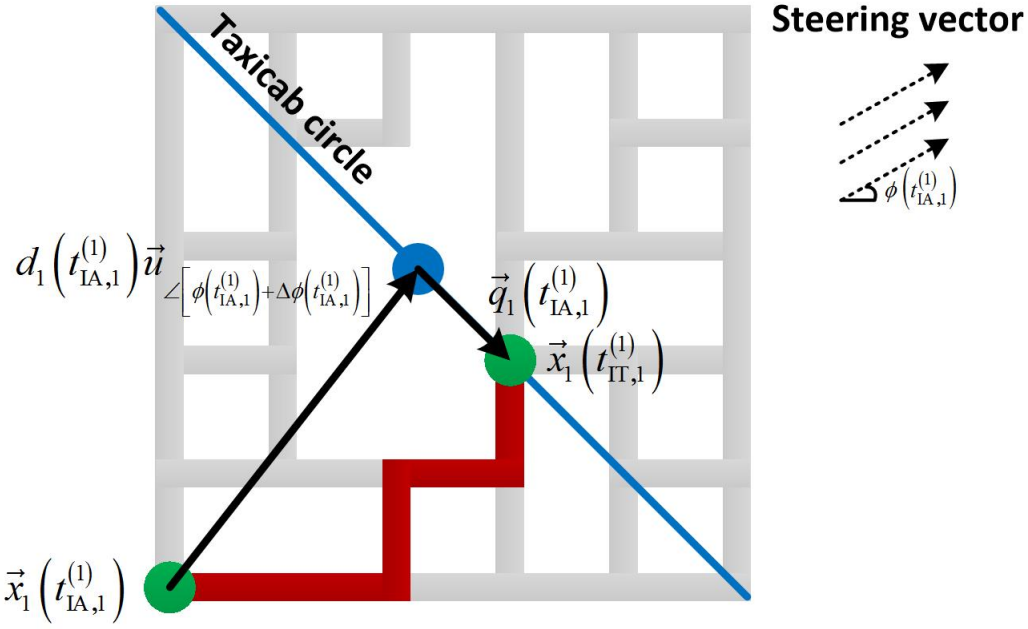

Figure 2.6: Updating of a guess input in the taxicab vascular network subject to a specified steering vector.

zigzag pathway, $\vec{x}_1\left(t_{\mathrm{IT},1}^{(1)}\right)$, $\vec{x}_1\left(t_{\mathrm{IT},1}^{(1)}+\Delta t\right)$, $\cdots$, $\vec{x}_1\left(t_{\mathrm{IT},1}^{(1)}+K\Delta t\right)$, $\vec{x}_1\left(t_{\mathrm{IA},2}^{(1)}\right)$ as shown in Fig. 2.7, where $\Delta t = \left(t_{\mathrm{IA},2}^{(1)}-t_{\mathrm{IT},1}^{(1)}\right)/(K+1)$. Various imaging modalities such as MRI (Thoidingjam and Tiku; 2017) and microwave imaging (Bucci et al.; 2017) can be used to detect the magnetic contrast induced by multiple magnetic nanoswimmers simultaneously, which allows for tracking of all the nanoswimmers. In contrast to mathematical computing where the location of a guess input is known exactly, the guess location in the current "natural" computing needs to be estimated. The positioning error is summarized in the random variable $\Delta\vec{x}_1$ as also shown in Fig. 2.7, whose horizontal and vertical components are assumed to be independently and identically distributed Gaussian random variables with equal variance

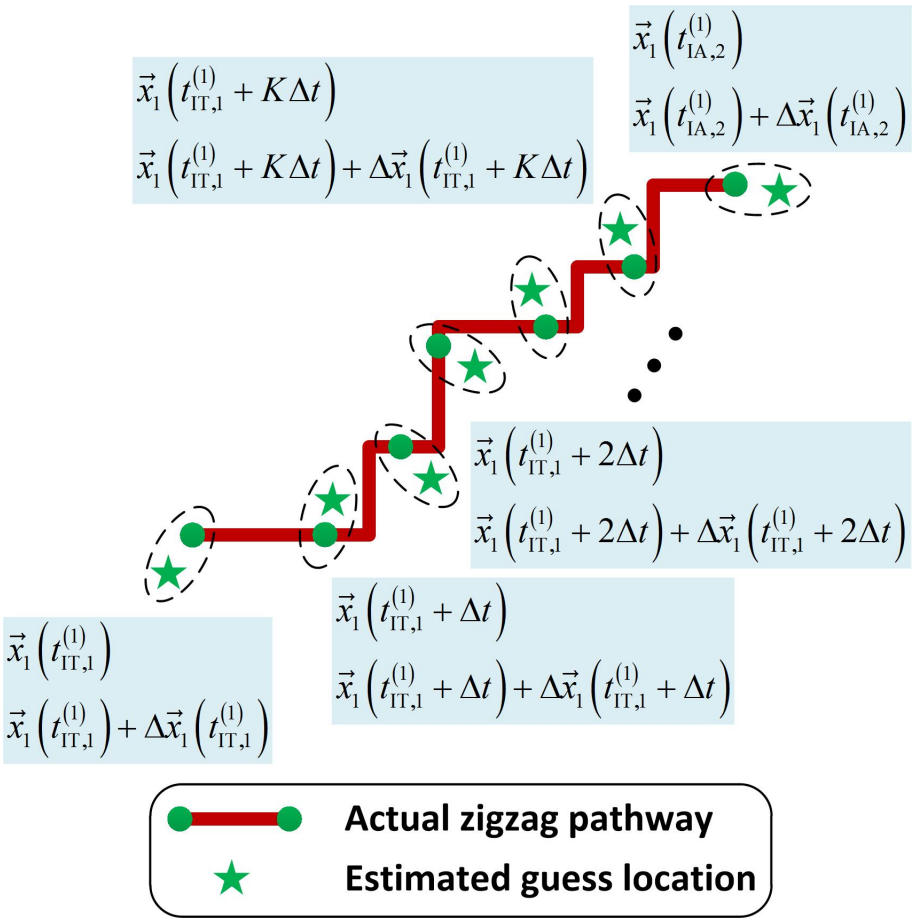

Figure 2.7: Pictorial illustration of the IT process: the guess follows a random walk in the lattice and moves towards various locations along a zigzag pathway, $\vec{x}_1\left(t_{\mathrm{IT},1}\right)$, $\vec{x}_1\left(t_{\mathrm{IT},1}+\Delta t\right)$, $\cdots$, $\vec{x}_1\left(t_{\mathrm{IT},1}+K\Delta t\right)$, $\vec{x}_1\left(t_{\mathrm{IA},2}\right)$ with Δt being the observation time interval.

$\sigma_{\Delta x}^2$ and zero mean for simplicity. In that case, $|\Delta\vec{x}_1|$ is Rayleigh-distributed. The objective function is then evaluated at each location. For example, if

the nanoswimmer velocity is considered, the values are obtained as

$$
\begin{aligned}
& f\left(\vec{x}_1\left(t_{\mathrm{IT},1}^{(1)}+k\Delta t\right)+\Delta\vec{x}_1\left(t_{\mathrm{IT},1}^{(1)}+k\Delta t\right)\right) \\
& \approx \frac{1}{\Delta t}\Big\|\vec{x}_1\left(t_{\mathrm{IT},1}^{(1)}+(k+1)\Delta t\right) \\
& \qquad +\Delta\vec{x}_1\left(t_{\mathrm{IT},1}^{(1)}+(k+1)\Delta t\right) \\
& \qquad -\vec{x}_1\left(t_{\mathrm{IT},1}^{(1)}+k\Delta t\right) \\
& \qquad -\Delta\vec{x}_1\left(t_{\mathrm{IT},1}^{(1)}+k\Delta t\right)\Big\|_1,\ k=0,1,\cdots,K.
\end{aligned}
\tag{2.8}
$$

Subsequently, the gradient for guess G_1 at $t_{\mathrm{IT},1}^{(1)}$ is estimated as follows

$$
\begin{aligned}
& \nabla f\left(\vec{x}_1\left(t_{\mathrm{IT},1}^{(1)}\right)\right) \\
& \approx \max_{k_1,k_2} \\
& \Bigg\{\Big[f\left(\vec{x}_1\left(t_{\mathrm{IT},1}^{(1)}+k_1\Delta t\right)+\Delta\vec{x}_1\left(t_{\mathrm{IT},1}^{(1)}+k_1\Delta t\right)\right) \\
& \quad -f\left(\vec{x}_1\left(t_{\mathrm{IT},1}^{(1)}+k_2\Delta t\right)+\Delta\vec{x}_1\left(t_{\mathrm{IT},1}^{(1)}+k_2\Delta t\right)\right)\Big]\Big/ \\
& \quad \Big\|\vec{x}_1\left(t_{\mathrm{IT},1}^{(1)}+k_1\Delta t\right)+\Delta\vec{x}_1\left(t_{\mathrm{IT},1}^{(1)}+k_1\Delta t\right) \\
& \quad -\vec{x}_1\left(t_{\mathrm{IT},1}^{(1)}+k_2\Delta t\right)-\Delta\vec{x}_1\left(t_{\mathrm{IT},1}^{(1)}+k_2\Delta t\right)\Big\|_2\Bigg\}, \\
& \qquad\qquad k_1>k_2 \text{ and } k_1,k_2\in\{0,1,\cdots,K\},
\end{aligned}
\tag{2.9}
$$

where $\|\cdot\|_2$ is the ℓ_2 norm. The overall gradient after N IT processes is estimated by taking into account all the N gradients obtained at $t_{\mathrm{IT},1}^{(1)}, t_{\mathrm{IT},2}^{(1)}, \cdots$, $t_{\mathrm{IT},N}^{(1)}$, respectively. A new steering vector for G_1 is then computed by following a specified algorithm as discussed in Section 2.5, which is used to guide the movement of G_1 during the next IA operation at $t_{\mathrm{IA},1}^{(2)}$ as shown in Fig.

2.5(a). As the nanoswimmer is in the form of nanochains or bundle-like aggregates assembled by MNPs (Cheang and Kim; 2015), it has a finite lifespan due to the dissembling and diffusion of MNPs during propagation. In the case that G_1 is fully consumed in $\mathbb{D}$, a new guess input is deployed at $\mathbb{R}$.

For TDM2, G_1 operates in the UA mode (as explained below) from $t^{(1)}_{\mathrm{IA},2}$ to $t^{(1)}_{\mathrm{IA},3}$ when G_2 is in the IA mode.

4. *UA*. For TDM1, from $t^{(1)}_{\mathrm{IA},2}$ to $t^{(1)}_{\mathrm{IT},2}$, G_1 operates in the UA mode. This is similar to the IA operation except that the steering field is meant for the second guess G_2. This is due to the limitation of the current coil system in generating the steering field, which exerts a global uniform torque on all the nanoswimmers simultaneously instead of localized torques on individual nanoswimmers. The same DTS steps (i.e., IA $\rightarrow$ IT $\rightarrow$ UA) are applied to all the guesses in sequence and the iteration continues unless certain stopping criteria are met.

   For TDM2, from $t^{(1)}_{\mathrm{IA},3}$ to $t^{(1)}_{\mathrm{IA},4}$, G_1 again operates in the UA mode when G_3 is now in the IA mode. The next IT operation only occurs after all the guess inputs complete their individual IA operations. This will be followed by a new round of IA $\rightarrow$ UA $\rightarrow$ IT operations starting at $t^{(2)}_{\mathrm{IA},1}$ as shown in Fig. 2.5(b).

The mapping from an iterative optimization process in mathematical computing to the aforementioned tumor sensitization process in natural computing is illustrated in Fig. 2.8, which encompasses the following procedures.

1. *General Mapping.* Formulate the nanoswimmers-assisted tumor sensitization in the perspective of natural computing as a stylized representation of the iterative optimization problem in mathematical computing.

2. *Specific Mapping.* Consider a specific iterative optimization algorithm $\mathcal{A}$ (e.g., GD), and map $\mathcal{A}$ onto the corresponding DTS $\mathcal{S}$. For example, the key operations in a standard GD include taking the step, finding the gradient, and evaluating the objective function. The first operation corresponds to the IA mode in the DTS and the last two operations are associated with the IT mode in the DTS.

3. *Reality Check.* Identify the key physical constraints associated with $\mathcal{S}$ when applied in a realistic *in vivo* environment, compared to the original algorithm $\mathcal{A}$ when applied in an idealistic mathematical setting. For example, the imperfections in DTS include the landscape mismatch $\chi\left(\vec{x};G\right)$ in (2.2), the steering imperfection $\Delta\phi\left(t_{\mathrm{IA},1}^{(1)}\right)$ and the landscape quantization noise $\vec{q}_1\left(t_{\mathrm{IA},1}^{(1)}\right)$ in (2.6), the finite velocity of guess $v_1\left(t_{\mathrm{IA},1}^{(1)}\right)$ in (2.7), the positioning error $\Delta\vec{x}_1\left(t_{\mathrm{IT},1}^{(1)}+(k+1)\Delta t\right)$ and the gradient estimation inaccuracy in (2.8), the interference in guess update caused by UA, and the finite lifespan of guess inputs.

4. *Performance Benchmarking.* From the tumor sensitization perspective, we can evaluate the performance of the DTS $\mathcal{S}$ by comparing $\mathcal{S}$ to the "brute-force" systemic targeting without implementing any knowledge-aided strategy. From the iterative optimization perspective, we can compare $\mathcal{S}$ to the standard algorithm $\mathcal{A}$. In this case, $\mathcal{S}$ is regarded as a degenerate form of $\mathcal{A}$.

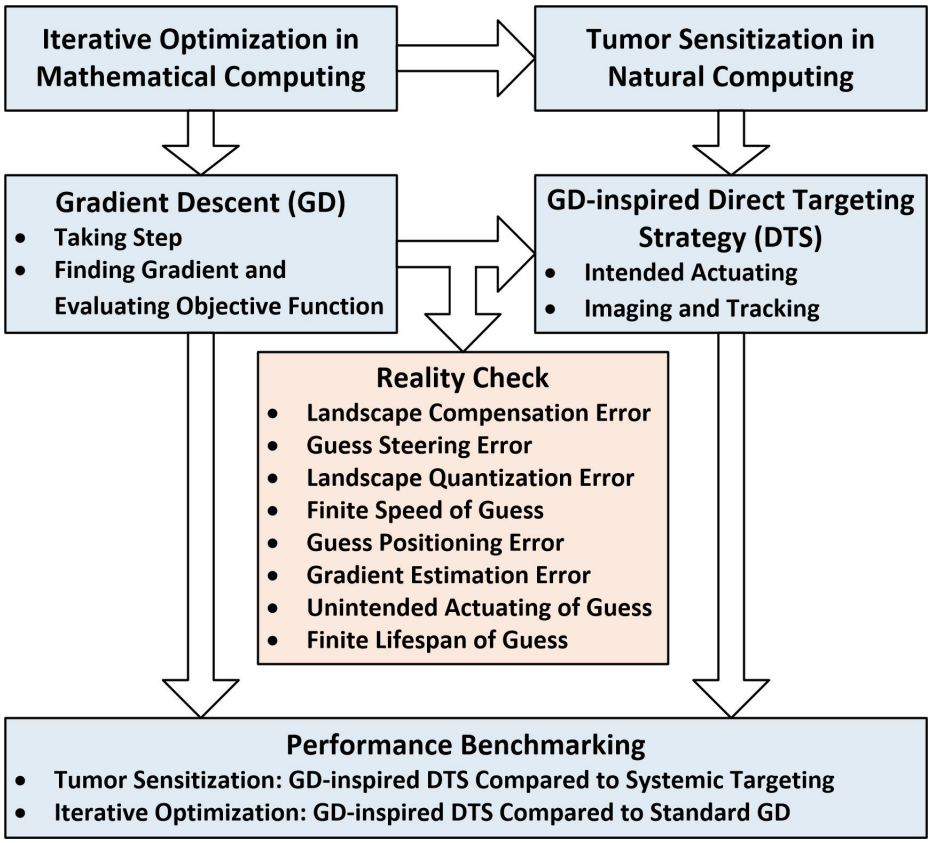

Figure 2.8: Mapping from iterative optimization in mathematical computing to tumor sensitization in natural computing.

2.5 GD-inspired DTS

The GD-inspired DTS starts with a generic guess G_1 located at $\vec{x}_1$ at time instant $t_{\mathrm{IA},1}^{(1)}$, which attempts to find a global maximum $f(\vec{x}^*)$.

2.5.1 DTS for TDM1

For TDM1 shown in Fig. 2.5(a), consider the sequence $\vec{x}_1\left(t_{\mathrm{IT},1}^{(1)}\right), \vec{x}_1\left(t_{\mathrm{IT},1}^{(2)}\right), \vec{x}_1\left(t_{\mathrm{IT},1}^{(3)}\right), \cdots$, over multiple iterations. In the classical GD, $\vec{x}_1\left(t_{\mathrm{IT},1}^{(m)}\right) = \vec{x}_1\left(t_{\mathrm{IT},1}^{(m-1)}\right) +$

$\gamma_{m-1}\nabla f\left(\vec{x}_1\left(t_{\mathrm{IT},1}^{(m-1)}\right)\right), m = 2,3,\cdots$. In this way, we have $f\left(\vec{x}_1\left(t_{\mathrm{IT},1}^{(1)}\right)\right) \leq f\left(\vec{x}_1\left(t_{\mathrm{IT},1}^{(2)}\right)\right) \leq f\left(\vec{x}_1\left(t_{\mathrm{IT},1}^{(3)}\right)\right) \leq \cdots$, so hopefully the sequence $\vec{x}_1\left(t_{\mathrm{IT},1}^{(m)}\right)$ converges to the desired global maximum. However, in the GD-inspired DTS, the location updating is interrupted by multiple IT and UA processes as depicted in Fig. 2.5(a). Hence, the position update is modified as $\vec{x}_1\left(t_{\mathrm{IT},1}^{(m)}\right) = \vec{x}_1\left(t_{\mathrm{IA},1}^{(m)}\right) + \gamma_m\nabla f\left(\vec{x}_1\left(t_{\mathrm{IA},1}^{(m)}\right)\right)$.

The gradient $\nabla f\left(\vec{x}_1\left(t_{\mathrm{IA},1}^{(m)}\right)\right)$ is estimated through the N IT processes as illustrated in Fig. 2.5(a). If the gradient does not change much over the duration of $t_{\mathrm{IT},1}^{(m)}$ to $t_{\mathrm{IT},1}^{(m+1)}$, it can be estimated as

$$\nabla f\left(\vec{x}_1\left(t_{\mathrm{IA},1}^{(m)}\right)\right) \approx \max_{n=1,2,\cdots,N}\left\{\nabla f\left(\vec{x}_1\left(t_{\mathrm{IT},n}^{(m)}\right)\right)\right\}. \tag{2.10}$$

Otherwise, only the last gradient estimate is used such that

$$\nabla f\left(\vec{x}_1\left(t_{\mathrm{IA},1}^{(m)}\right)\right) \approx \nabla f\left(\vec{x}_1\left(t_{\mathrm{IT},N}^{(m)}\right)\right). \tag{2.11}$$

Suppose that $f(\vec{x})$ is convex and $\nabla f(\vec{x})$ is Lipschitz, the step size γ_m can be chosen to guarantee convergence to a global optimum by using the Barzilai-Borwein method (Barzilai and Borwein; 1988):

$$\begin{aligned}\gamma_m \approx & \frac{\left(\vec{x}_1\left(t_{\mathrm{IA},1}^{(m)}\right) - \vec{x}_1\left(t_{\mathrm{IA},1}^{(m-1)}\right)\right)^T}{\left\|\nabla f\left(\vec{x}_1\left(t_{\mathrm{IA},1}^{(m)}\right)\right) - \nabla f\left(\vec{x}_1\left(t_{\mathrm{IA},1}^{(m-1)}\right)\right)\right\|^2} \\ & \times\left[\nabla f\left(\vec{x}_1\left(t_{\mathrm{IA},1}^{(m)}\right)\right) - \nabla f\left(\vec{x}_1\left(t_{\mathrm{IA},1}^{(m-1)}\right)\right)\right].\end{aligned} \tag{2.12}$$

Note that the vessel network used in the simulation procedure is a discontinuous two-dimensional grid as shown in Fig. 2.3; therefore the position update follows

the procedure described in Section 2.4.2. As the vessels run only parallel to the two coordinate axes, at each junction the guess input can move in two possible directions, up and right, as the flow is from the lower left to the upper right. The Barzilai-Borwein condition in (2.12) is employed to determine the duration of the m^{th} IA operation for G_1:

$$t_{\text{IT},1}^{(m)} - t_{\text{IA},1}^{(m)} = \frac{\gamma_m \cos\phi_m + \gamma_m \sin\phi_m}{v_1\left(t_{\text{IA},1}^{(m)}\right)}, \tag{2.13}$$

where ϕ_m is the angle of the gradient estimated at the m^{th} cycle.

2.5.2 DTS for TDM2

For TDM2 shown in Fig. 2.5(b), similarly, consider the sequence $\vec{x}_1\left(t_{\text{IA},2}^{(1)}\right), \vec{x}_1\left(t_{\text{IA},2}^{(2)}\right), \vec{x}_1\left(t_{\text{IA},2}^{(3)}\right), \cdots$. In the classical GD, $\vec{x}_1\left(t_{\text{IA},2}^{(m)}\right) = \vec{x}_1\left(t_{\text{IA},2}^{(m-1)}\right) + \gamma_{m-1}\nabla f\left(\vec{x}_1\left(t_{\text{IA},2}^{(m-1)}\right)\right)$, $m = 2, 3, \cdots$, to ensure that the sequence $\vec{x}_1\left(t_{\text{IA},2}^{(m)}\right)$ converges to the desired global maximum. However, in the GD-inspired DTS, the location updating is interrupted by multiple UA processes and one IT process as depicted in Fig. 2.5(b). Hence, the position update is expressed as $\vec{x}_1\left(t_{\text{IA},2}^{(m)}\right) = \vec{x}_1\left(t_{\text{IA},1}^{(m)}\right) + \gamma_m \nabla f\left(\vec{x}_1\left(t_{\text{IA},1}^{(m)}\right)\right)$.

To ensure that such an arrangement does not favor IA processes that are closer to the earlier IT operation resulted from more accurate gradient estimation, the gradient change over the duration of $t_{\text{IA},1}^{(m-1)}$ to $t_{\text{IA},1}^{(m)}$ should be minimal, which is approximated by

$$\nabla f\left(\vec{x}_1\left(t_{\text{IA},1}^{(m)}\right)\right) \approx \nabla f\left(\vec{x}_1\left(t_{\text{IT}}^{(m-1)}\right)\right), \tag{2.14}$$

where $\nabla f\left(\vec{x}_1\left(t_{\text{IT}}^{(m-1)}\right)\right)$ is the gradient estimated during the $(m-1)^{\text{th}}$ IT process.

Finally, due to the practical constraint of DTS, the initial deployment region of the guess input is confined within a small area, which is the injection site of nanoswimmers, instead of the entire solution space. To further ensure that the guess input is confined within the tissue region under screening, the replacement strategy is implemented: a guess that travels outside the allowed searching region is abandoned, which will degrade in the human body without further maneuvering and tracking. A new guess is then generated in the deployment area by injecting an aggregate of nanoswimmers.

2.6 Performance Analysis

We use several numerical examples to evaluate the tumor sensitization and targeting performance of the GD-inspired DTS, which is compared to the brute-force search.

2.6.1 Simulation Set-up

The simulation tool used in the computational experiments is MATLAB®. The multi-layer vasculature in the surveillance region, -5 mm $\leq x, y \leq 5$ mm, is generated by using the inversion-percolation-based model described in Section 2.3 and depicted in Fig. 2.3. The three objective functions presented in Section 2.4.1 are applied to synthesize different levels of tumor sensitization difficulty, which are defined on the discretized domain of the vasculature. The deployment region is set to be -5 mm $\leq x, y \leq -4$ mm, within which the initial positions of the guesses are uniformly generated. The speed of nanoswimmers is assumed to be 100 μm/s. The maximum search time allowed and the number of simulation runs are set to

be 200 s and 1000, respectively. Two performance metrics are considered, the probability of cancer detection P_D given by the ratio of the number of occurrences when the tumor is successfully detected to the total number of simulations, and the percentage of contrast agent nanoparticles delivered to the tumor site η given by the ratio of the amount of guesses reaching the tumor to the amount of guesses deployed.

For the proposed DTS, both the two protocols in Fig. 2.5 are considered where the simulation procedure follows the steps in Section 2.4.2. In the current study, two guess inputs are deployed for direct targeting at each round of simulation. The durations of IA and IT are set to be 10 s and the number of observation intervals during each IT operation (see also Fig. 2.7) is 10. The searching process would be stopped if any guess reaches the cancer center denoted by a circle of radius 0.5 mm at the origin as shown in Fig. 2.4. It is assumed that the other guess would be guided to the tumor center upon successful detection if it has not overshot the tumor location.

For the brute-force search, the same objective functions as those applied in the DTS are considered. Nevertheless, each guess follows a random walk in the lattice (i.e., at each intersection it has the same probability to either move up or to the right) without making use of the gradient of the objective function, which synthesizes the scenario that contrast medium nanoparticles are carried through the systemic circulation in order to target a tumor for contrast-enhanced medical imaging. When the number of nanoparticles is sufficiently large (i.e., a multitude of guess samples over multiple simulation runs), systemic administration essentially enumerates all possible pathways in the vascular network and thus is similar to the brute-force search. For consistency with the setting of the DTS, two guess inputs

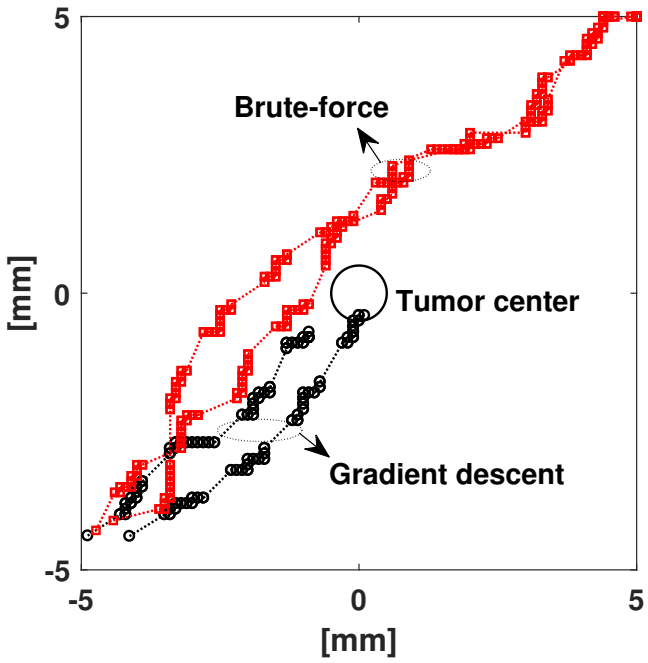

Figure 2.9: Trajectories of guess inputs when TDM1 is applied: "○" - GD-inspired DTS, "□" - brute-force search.

are deployed at each simulation. Furthermore, the random drift and IT durations follow the two protocols in Fig. 2.5, though the movements of these two guesses are completely independent of each other due to lack of a common steering field. The searching process would be stopped if any guess reaches the cancer center as in the case of DTS. However, the other guess would continue its random drift in the absence of an external guidance.

2.6.2 Simulation Results

Fig. 2.9 shows the typical trajectories of guess inputs for the landscape of Sphere function when the TDM1 protocol is applied. The symbols of "○" and "□" denote

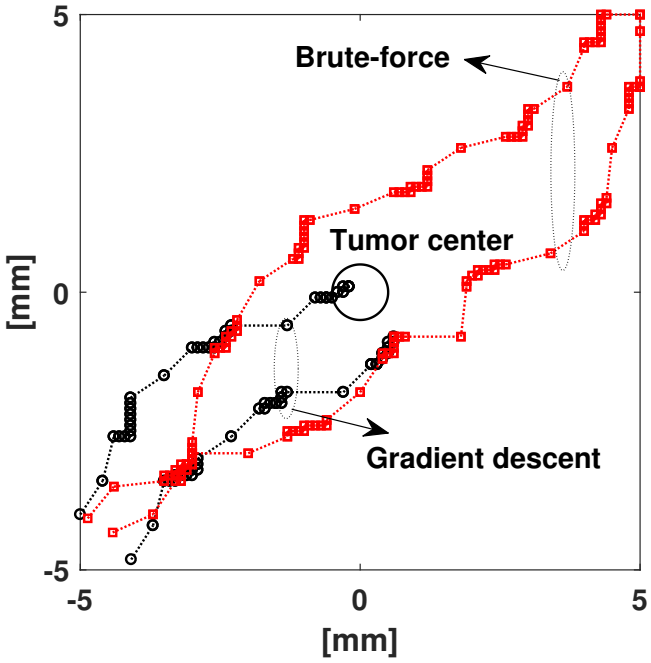

Figure 2.10: Trajectories of guess inputs when TDM2 is applied: "○" - GD-inspired DTS, "□" - brute-force search.

the actual guess footprints for the GD-inspired DTS and brute-force search, respectively, and regions with clustered footprints correspond to the IA mode. As can be seen from the figure, in the case of DTS the movement of both guesses is coordinated by an external field towards the maximum-gradient direction estimated in the IA mode. On the other hand, the movement of two guesses is irregular and uncorrelated for the brute-force search. The DTS successfully detects the tumor center, whereas the brute-force search technique fails to find the center of tissue malignancy because only a fraction of the possible pathways are explored with two guess inputs in one simulation run. Fig. 2.10 presents the guess trajectories when the TDM2 protocol is applied. The time interval between two consecutive IAs

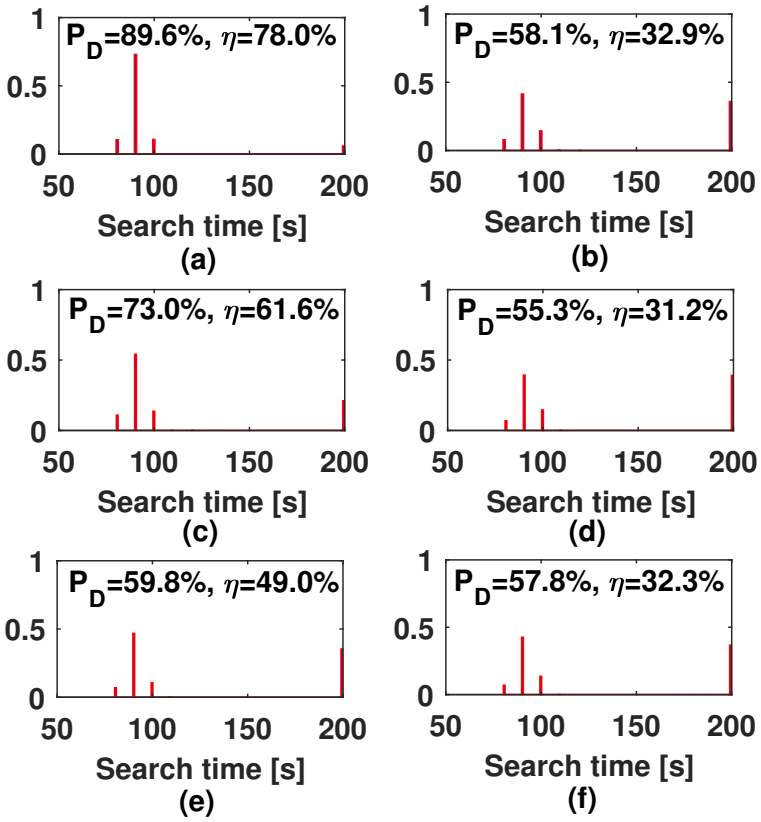

Figure 2.11: Histograms of search time when TDM1 is applied: (a) GD-inspired DTS and (b) brute-force search in a Sphere landscape; (c) GD-inspired DTS and (d) brute-force search in a Matyas landscape; (e) GD-inspired DTS and (f) brute-force search in an Easom landscape. Also shown are the respective detection ratios P_D and targeting efficiencies η.

for TDM2 is twice of the value for TDM1 because in the former case, each guess takes turn to operate in the IA mode, followed by a common IT mode. Hence, the gradient estimated during the IT operation may be different from the actual gradient for the later IA process, leading to more departing trajectories of the guesses as depicted in Fig. 2.10. It is expected that this phenomenon would result in

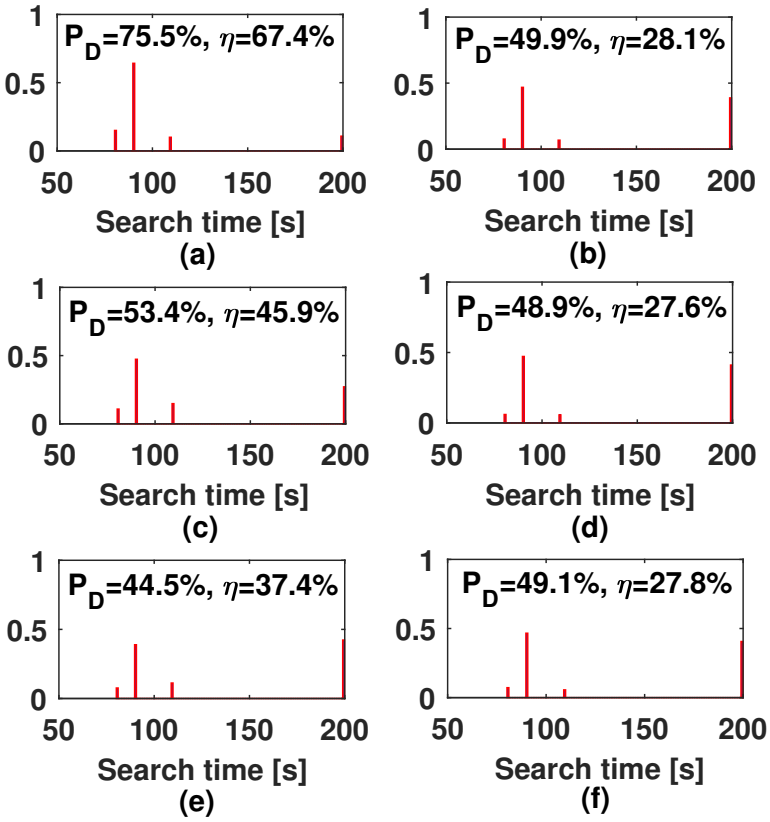

Figure 2.12: Histograms of search time when TDM2 is applied: (a) GD-inspired DTS and (b) brute-force search in a Sphere landscape; (c) GD-inspired DTS and (d) brute-force search in a Matyas landscape; (e) GD-inspired DTS and (f) brute-force search in an Easom landscape. Also shown are the respective detection ratios P_D and targeting efficiencies η.

deteriorating tumor sensitization and targeting performance. Similar observations can be made for the Matyas and Easom landscapes.

Fig. 2.11 presents the histograms of search time for the three objective functions when the TDM1 protocol is employed. The search time of 200 s (maximum value) indicates the situation that none of the two guesses senses the tumor. It can be seen that the GD-inspired DTS yields a detection ratio of $P_D = 89.6\%$ for the

Sphere function (Fig. 2.11(a)), which is much higher than that for the brute-force search ($P_D = 58.1\%$, Fig. 2.11(b)). Furthermore, the DTS has better performance in the Sphere landscape than the Matyas ($P_D = 73.0\%$, Fig. 2.11(c)) and Easom ($P_D = 59.8\%$, Fig. 2.11(e)) functions. This observation demonstrates the advantage of the proposed biosensing-by-learning strategy over brute-force search and the potential performance deterioration due to a more complex landscape (i.e., plate-shaped Matyas function and gradientless Easom function versus bowl-shaped Sphere function). In terms of the targeting efficiency, the DTS achieves a much higher value of $\eta = 78.0\%$ compared to that for the Matyas ($\eta = 61.6\%$) and Easom ($\eta = 49.0\%$) functions as well as the brute-force search ($\eta \approx 32\%$).

Fig. 2.12 presents the histograms of search time for TDM2. Similar observations to the trend in Fig. 2.11 can be made. Furthermore, comparing Fig. 2.12 to Fig. 2.11 shows that, TDM1 yields higher probabilities of tumor sensitization and larger percentages of drug molecules delivered to the tumor than TDM2.

2.7 Conclusion

We have proposed a novel iterative-optimization-inspired DTS in externally manipulable smart nanosystems, which exploits tumor-triggered *in vivo* biological gradients for "guided" direct targeting. We have demonstrated through computational experiments that the proposed DTS can significantly improve the probability of tumor sensitization and the accumulation of drug nanoparticles in the tumor site by using the shortest possible physiological routes and with minimal systemic exposure. We believe that this work motivates a new paradigm directed toward smart biosensing facilitated by externally controllable nanoswimmers.

Future work may include extension of the framework to DTS inspired by multi-solution or multi-objective optimizations when there are multiple tumors or different phenomena-of-interest in the tissue region under surveillance. Moreover, it is important to examine further the impact of nanoswimmer nonidealities, such as finite lifespan, imprecise steering, and inaccurate tracking. Finally, the proposed DTS and the objective functions used should be validated by real experiments to justify further the clinical relevance of the proposed strategy.

References

Agemy, L., Sugahara, K. N., Kotamraju, V. R., Gujraty, K., Girard, O. M., Kono, Y., Mattrey, R. F., Park, J.-H., Sailor, M. J., Jimenez, A. I., Cativiela, C., Zanuy, D., Sayago, F. J., Aleman, C., Nussinov, R. and Ruoslahti, E. (2010). Nanoparticle-induced vascular blockade in human prostate cancer, *Blood* **116**: 2847–2856.

Bae, Y. H. and Park, K. (2011). Targeted drug delivery to tumors: Myths, reality and possibility, *J. Con. Rel.* **153**: 198–205.

Baish, J. W., Gazit, Y., Berk, D. A., Nozue, M., Baxter, L. T. and Jain, R. K. (1996). Role of tumor vascular architecture in nutrient and drug delivery: An invasion percolation-based network model, *Microvasc. Res.* **51**: 327–346.

Baish, J. W. and Jain, R. K. (2000). Fractals and cancer, *Cancer Res.* **60**: 3683–3688.

Barzilai, J. and Borwein, J. M. (1988). Two-point step size gradient methods, *IMA Journal of Numerical Analysis* **8**(1): 141–148.

Bucci, O. M., Bellizzi, G., Borgia, A., Costanzo, S., Crocco, L., Massa, G. D. and Scapaticci, R. (2017). Experimental framework for magnetic nanoparticles enhanced breast cancer microwave imaging, *IEEE Access* **5**: 16332–16340.

Bucci, O. M., Crocco, L. and Scapaticci, R. (2015). On the optimal measurement configuration for magnetic nanoparticles-enhanced breast cancer microwave imaging, *IEEE Trans. Biomed. Eng.* **62**(2): 407–414.

Cheang, U. K., Kim, H., Milutinović, D., Choi, J. and Kim, M. J. (2017). Feedback control of robotic achiral microswimmers, *J. Bionic. Eng.* **14**(2): 245–259.

Cheang, U. K. and Kim, M. J. (2015). Self-assembly of robotic micro- and nanoswimmers using magnetic nanoparticles, *J. Nanopart. Res.* **17**(145).

Cheang, U. K., Meshkati, F., Kim, H., Lee, K., Fu, H. C. and Kim, M. J. (2016). Versatile microrobotics using simple modular subunits, *Sci. Rep.* **6**(30472).

Chen, Y., Kosmas, P., Anwar, P. S. and Huang, L. (2015). A touch-communication framework for drug delivery based on a transient microbot system, *IEEE Trans. Nanobiosci.* **14**(4): 397–408.

Chen, Y., Kosmas, P. and Martel, S. (Article ID 309703, 11 pages, http://dx.doi.org/10.1155/2013/309703). A feasibility study for microwave breast cancer detection using contrast-agent-loaded bacterial microbots, *Int. J. Antennas Propag.* **2013**.

Chen, Y., Nakano, T., Kosmas, P., Yuen, C., Vasilakos, A. V. and Asvial, M. (2016). Green touchable nanorobotic sensor networks, *IEEE Commun. Mag.* pp. 136–142.

Chen, Y., Shi, S., Yao, X. and Nakano, T. (2017). Touchable computing: Computing-inspired bio-detection, *IEEE Trans. Nanobiosci.* **16**(8): 810–821.

Dudar, T. E. and Jain, R. K. (1984). Differential response of normal and tumor microcirculation to hyperthermia, *Cancer Res.* **44**: 605–612.

Felfoul, O., Mohammadi, M., Taherkhani, S. and et al. (2016). Magneto-aerotactic bacteria deliver drug-containing nanoliposomes to tumour hypoxic regions, *Nature Nanotechnology* **11**: 941–947.

Fukumura, D. and Jain, R. K. (2007). Tumor microvasculature and microenvironment: targets for anti-angiogenesis and normalization, *Microvasc. Res.* **74**: 72–84.

Gazit, Y., Berk, D. A., Leunig, M., Baxter, L. T. and Jain, R. K. (1995). Scale-invariant behavior and vascular network formation in normal and tumor tissue, *Phys. Rev. Lett.* **75**(12): 2428–2431.

Kim, H., Lee, J., Oh, C. and Park, J.-H. (2017). Cooperative tumour cell membrane targeted phototherapy, *Nat. Commun.* **8**(15880): 1–10.

Komar, G., Kauhanen, S., Liukko, K., Seppanen, M., Kajander, S., Ovaska, J., Nuutila, P. and Minn, H. (2009). Decreased blood flow with increased metabolic activity: A novel sign of pancreatic tumor aggressiveness, *Clin. Cancer Res.* **15**(17): 5511–5517.

Kwon, E. J., Lo, J. H. and Bhatia, S. N. (2015). Smart nanosystems: Bio-inspired technologies that interact with the host environment, *Proc. Natl. Acad. Sci. U. S. A.* **112**(47): 14460–14466.

Lazebnik, M., Popovic, D., McCartney, L., B.Watkins, C., Lindstrom, M. J., Harter, J., Sewall, S., Ogilvie, T., Magliocco, A., Breslin, T. M., Temple, W., Mew, D., Booske, J. H., Okoniewski, M. and Hagness, S. C. (2007). A large-scale study of the ultrawideband microwave dielectric properties of normal, benign and malignant breast tissues obtained from cancer surgeries, *Phys. Med. Biol.* **52**: 6093–6115.

Lee, D.-S., Rieger, H. and Bartha, K. (2006). Flow correlated percolation during vascular remodeling in growing tumors, *Phys. Rev. Lett.* **96**(058104).

McDougall, S. R., Anderson, A. R. A. and Chaplain, M. A. J. (2002). Mathematical modelling of flow through vascular networks: Implications for tumor-induced angiogenesis and chemotherapy strategies, *Bull. Math. Biol.* **64**: 673–702.

Meaney, P. M., Kaufman, P. A., Muffly, L. S., Click, M., Poplack, S. P., Wells, W. A., Schwartz, G. N., di Florio-Alexander, R. M., Tosteson, T. D., Li, Z., Geimer, S. D., Fanning, M. W., Zhou, T., Epstein, N. R. and Paulsen, K. D. (2013). Microwave imaging for neoadjuvant chemotherapy monitoring: Initial clinical experience, *Breast Cancer Res.* **15**(2): 1–16.

Mertz, L. (2018). Tiny conveyance: Micro- and nanorobots prepare to advance medicine, *IEEE Pulse* **9**(1): 19–23.

Modiri, A., Goudreau, S., Rahimi, A. and Kiasaleh, K. (2017). Review of breast screening: Toward clinical realization of microwave imaging, *Med. Phys.* **44**(12): e446–e458.

O'Loughlin, D., O'Halloran, M. J., Moloney, B. M., Glavin, M., Jones, E. and Elahi, M. A. (2018, Early Access, DOI: 10.1109/TBME.2018.2809541). Mi-

crowave breast imaging: Clinical advances and remaining challenges, *IEEE Trans. Biomed. Eng.* .

O'Rourke, A. P., Lazebnik, M., Bertram, J. M. and et al. (2007). Dielectric properties of human normal, malignant and cirrhotic liver tissue: *in vivo* and *ex vivo* measurements from 0.5 to 20 GHz using a precision open-ended coaxial probe, *Phys. Med. Biol.* **52**: 4707–4719.

Overchuk, M. and Zheng, G. (2018). Overcoming obstacles in the tumor microenvironment: Recent advancements in nanoparticle delivery for cancer theranostics, *Biomaterials* **156**: 217–237.

Park, J.-H., von Maltzahn, G., Ong, L. L., Centrone, A., Hatton, T. A., Ruoslahti, E., Bhatia, S. N. and Sailor, M. J. (2010). Cooperative nanoparticles for tumor detection and photothermally triggered drug delivery, *Adv. Mater.* **22**: 880–885.

Park, J.-H., von Maltzahnc, G., Xu, M. J., Fogald, V., Kotamraju, V. R., Ruoslahti, E., Bhatia, S. N. and Sailor, M. J. (2010). Cooperative nanomaterial system to sensitize, target, and treat tumors, *Proc. Natl. Acad. Sci. U. S. A.* **107**(3): 981–986.

Porter, E., Coates, M. and Popović, M. (2016). An early clinical study of time-domain microwave radar for breast health monitoring, *IEEE Trans. Biomed. Eng.* **63**(3): 530–539.

Preece, A. W., Craddock, I., Shere, M., Jones, L. and Winton, H. L. (2016). MARIA M4: Clinical evaluation of a prototype ultrawideband radar scanner for breast cancer detection, *J. Med. Imag.* **3**(3): 033502.

Rangayyan, R. M., El-Faramawy, N. M., Desautels, J. E. L. and Alim, O. A. (1997). Measures of acutance and shape for classification of breast tumors, *IEEE Trans. Med. Imag.* **16**(6): 799–810.

Saunders, R., Samei, E., Baker, J. and Delong, D. (2006). Simulation of mammographic lesions, *Academic Radiology* **13**(7): 860–870.

Seidi, K., Neubauer, H. A., Moriggl, R. and Jahanban-Esfahlan, R. (2018). Tumor target amplification: Implications for nano drug delivery systems, *J. Con. Rel.* **275**: 142–161.

Semenov, S. (2009). Microwave tomography: Review of the progress towards clinical applications, *Phil. Trans. R. Soc. A* **367**: 3021–3042.

Simberg, D., Duza, T., Park, J.-H., Essler, M., Pilch, J., Zhang, L., Derfus, A. M., Yang, M., Hoffman, R. M., Bhatia, S., Sailor, M. J. and Ruoslahti, E. (2007). Biomimetic amplification of nanoparticle homing to tumors, *Proc. Natl. Acad. Sci. U. S. A.* **104**(3): 932–936.

Song, C. W. (1984). Effect of local hyperthermia on blood flow and microenvironment: A review, *Cancer Res. (Suppl.)* **44**: 4721s–4730s.

Song, H., Sasada, S., Kadoya, T., Okada, M., Arihiro, K., Xiao, X. and Kikkawa, T. (2017). Detectability of breast tumor by a hand-held impulse-radar detector: Performance evaluation and pilot clinical study, *Sci. Rep.* **7**(1): 16353.

Thoidingjam, S. and Tiku, A. B. (2017). New developments in breast cancer therapy: role of iron oxide nanoparticles, *Adv. Nat. Sci.: Nanosci. Nanotechnol.* **8**: 023002.

von Maltzahn, G., Park, J.-H., Lin, K. Y., Singh, N., Schwöppe, C., Mesters, R., Berdel, W. E., Ruoslahti, E., Sailor, M. J. and Bhatia, S. N. (2011). Nanoparticles that communicate in vivo to amplify tumour targeting, *Nat. Mater.* **10**: 545–552.

Wang, Y., Iguchi, K., Ito, H., Ookawa, K., Kobayashi, N., Nakamura, R., Goto, Y., Sakai, M., Ishikawa, S. and Onizuka, M. (2009). Blood flow velocity is reduced in a tumor micro-dissemination in the visceral pleura in anesthetized open-chest rat lung, *In Vivo* **23**: 291–296.

Yang, F., Sun, L., Hu, Z., Wang, H., Pan, D., Wu, R., Zhang, X., Chen, Y. and Zhang, Q. (2017). A large-scale clinical trial of radar-based microwave breast imaging for Asian women: Phase I, *Proc. IEEE IEEE AP-S Symposium on Antennas and Propagation and USNC-URSI Radio Science Meeting 2017*, San Diego, USA.

Zhang, B., Wang, H., Shen, S., She, X., Shi, W., Chen, J., Zhang, Q., Hu, Y., Pang, Z. and Jiang, X. (2016). Fibrin-targeting peptide creka-conjugated multi-walled carbon nanotubes for self-amplified photothermal therapy of tumor, *Biomaterials* **79**: 46–55.

Chapter 3

In Vivo Computation with Sensor Fusion and Search Acceleration for Smart Tumor Homing

Background and Objective: Motivated by the advancements on bioresorbable nanoswimmers, this chapter considers the advantages of direct targeting over systemic targeting for smart tumor homing under the general framework of computational nanobiosensing. Nanoswimmers assembled by magnetic nanoparticles can be used as contrast agents to estimate the locations of tumors inside the human body.

Methods: Closely observing the response of nanoswimmers (which act as *in vivo* biosensors) to the tumor-triggered biological gradients and then guiding them through external manipulation, can result in a higher accumulation at the diseased location. Sensor informatics along with data fusion can play a crucial role in such a knowledge-aided targeting process. Specifically, built upon our previous

work on direct targeting inspired by the gradient descent optimization, this work is focused on resolving the real-life constraints of *in vivo* natural computation such as uniformity of the magnetic field and finite life span of the nanoswimmers. To overcome these challenges, we propose a multi-estimate-fusion strategy to obtain a common steering direction for the swarm of nanoswimmers.

Results: We show through computational experiments 1) that the mean of individual gradient estimations provides the best choice for symmetrical conditions (tumor location in line with the direction of blood flow) while leader-based swarm steering gives the best results for non-symmetrical search space, and 2) that the iterative memory-driven gradient descent optimization detects the target faster compared to the classical memory-less gradient descent and knowledge-less systemic targeting.

Conclusion: Our proposed strategies demonstrate that a clear demarcation between malignant tumors and healthy tissues can be visualized before nanoswimmers are consumed in human vasculature. We believe that our work will help in overcoming the challenges posed by natural *in vivo* computation for tumor diagnosis at its early stage.

3.1 Introduction

Early detection and localization of cancer can save up to two-third of cancer related deaths worldwide. Even with the best modern-era tools and strategies, cancerous cells can go unnoticed for 10 years when they have become 50 million cancer

cells strong (Hori and Gambhir; 2011). Conventional medical imaging techniques are constrained by resolution limits that are often insufficient to locate tumors at early stages (Kasban et al.; 2015). Micrometastasis and small high risk breast cancers (< 2 mm) can not be detected through state-of-the-art imaging modalities. Contrast agents such as CREKA-Tris $(\text{GD-DOTA})_3$, have been used in medical imaging to provide better demarcation between healthy and diseased tissues with dimensions smaller than 0.5 mm (Zhou et al.; 2015).

Magnetic nanoparticles (MNPs) are also commonly used for contrast enhancement. These MNPs are injected in the blood stream and can be magnetically guided to the cancerous site, thus increasing the resolution of imaging techniques like MRI through highlighting the diseased area. There are number of strategies which can be used to deliver MNPs to the tumor site. They can be categorized as “knowledge-less" if the movement of MNPs relies entirely on the human circulation system, and as “knowledge-aide” if the movement of engineered MNPs (with additional functions such as sensing, signaling and actuation) is externally manipulable.

With knowledge-less *systemic targeting*, an insufficient ($< 2\%$) number of nanoparticles reach the target tumor; thus this strategy is very inefficient (Bae and Park; 2011). Delivery of contrast agents to the tumor may be improved by using the *direct targeting* strategy in which non-manipulable nanoparticles are replaced by a swarm of externally manipulable nanoswimmers (NSs). These NSs can be directed to the target tumor by an externally applied steering field provided that the location of the tumor is known a priori. This has been shown to improve the efficiency of getting NSs to the target tumor (Felfoul et al.; 2016). However, acquiring sufficient knowledge of the location of the tumor is often problematic.

Diagnostic capability of NSs can also be amplified through *smart nanosystems* in which the tumor microenvironment is used to assist in detection of malignant tumors. In such nanosystems, NSs either sense the host environment after systemic administration and respond, or the host environment is first primed to interact with the engineered NSs (Kwon et al.; 2015). In both cases, prior knowledge of tumor location is not required. However, homing is achieved through systemic targeting with its associated weaknesses.

Instead of complete dependence on systemic targeting, *smart nanosystems* can be externally manipulated to guide a swarm of NSs towards the possible target direction (Chen et al.; 2019). This strategy can achieve faster and more efficient sensitization of the target (Chen, Ali, Shi and Cheang; 2019). However, challenges like uniformity of the realizable magnetic field, cytotoxicity and finite life span of NSs need to be adequately addressed (Shi et al.; 2020). An optimal external magnetic field for one NS may not be optimal for other NS of the swarm (Cheang and Kim; 2015). Hence, a compromised magnetic field has to be decided upon to counter the constraint of uniform magnetic field. Next, the swarm spreadness should be minimized to reduce the harm caused by cytotoxicity. Finally, NSs are chiral structure chains of magnetic nanoparticles linked together through biotin-streptavidin interactions (Wong et al.; 1999). Although, this bondage ensures linkage among nanoparticles, it is inevitable that some NSs may be disassembled during the process. Hence, target homing needs to be fast enough to avoid consumption of NSs in the human vasculature prior to tumor detection.

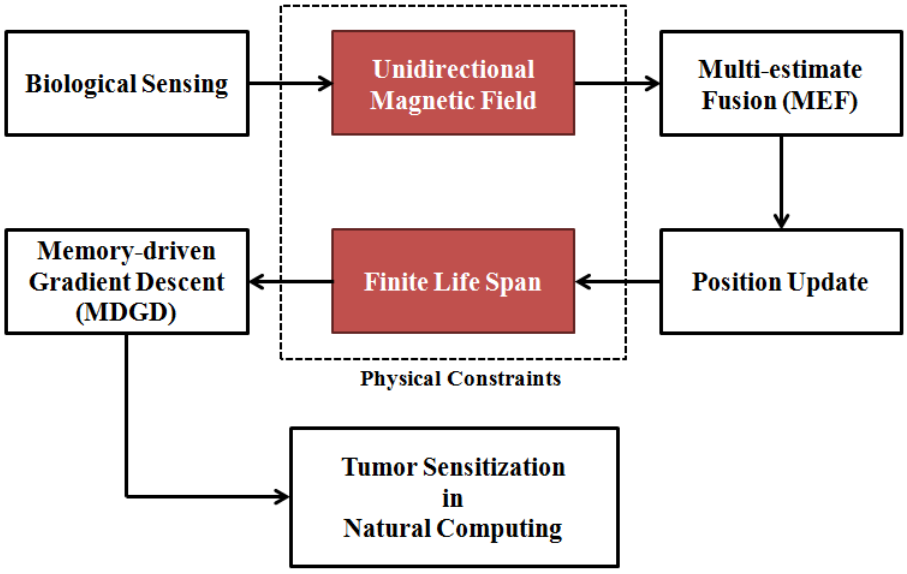

Figure 3.1: Flowchart to illustrate tumor sensitization in natural computing where red boxes demonstrate the key physical constraints addressed in current work.

3.1.1 Contributions of the Current Chapter

In this chapter, we aim to develop natural computing strategies that take into account the practical challenges of *in vivo* computation for tumor homing. Specifically,

1. We address the key physical constraint, i.e., unidirectional external magnetic field for steering the whole swarm (demonstrated in red in Fig. 3.1). With the help of multi-estimate fusion (MEF), we fuse the individual estimations of the desirable moving directions into a global estimate through different swarm steering strategies.

2. The focus throughout the tumor sensitization process is on maintaining swarm compactness which is vital to reducing the effect of cytotoxicity.

Hence, we propose the swarm spreadness as a key criterion for performance evaluation of multiple swarm steering strategies.

3. To address the finite life span limitation, we propose a memory-driven gradient descent (MDGD) strategy as shown in Fig. 3.1, which ensures faster target detection.

The efficiency of the aforementioned proposed strategies is tested through extensive simulation studies. Note that this chapter is focused on the early detection of common solid tumors such as lymphomas, sarcomas and carcinomas, which may exist in most organs or tissues of the human body.

3.1.2 Organization of the Chapter

The chapter is organized as follows. Section 3.2 outlines background knowledge along with the proposed externally manipulable smart nanosystem. In Section 3.3, tumor induced vasculature network and biological gradients are explained. Section 3.4 highlights the mapping between our proposed externally manipulable smart nanosystem and the iterative optimization process. The discretized vascular network model along with the introduction of several objective functions used to represent different scenarios of biological gradients are also introduced in this section. Section 3.5 formulates the computational framework along with different strategies for swarm steering using MEF. In addition, the direct targeting strategy inspired by MDGD for search acceleration is highlighted. System performance is analysed with the help of some numerical examples in Section 3.6 while some concluding remarks are given in Section 3.7.

3.2 Background

3.2.1 Cancer Sensitization through Systemic Targeting

Traditional tumor sensitization is passive targeting which relies on systemic circulation in the body. Systemic targeting is associated with cytotoxicity that ultimately harms healthy tissues along with malignant tumors. To control this side effect, targeted drug carriers such as nanoparticles or nanoliposomes have been proposed in the recent few decades (Upputuri et al.; 2015). Due to the influence of systemic circulation, ample driving force is not available to target the hypoxic regions. Moreover, nanoparticles are consumed and lost inside the human vasculature due to spreading (diffusion), deterioration, and branching (using wrong vessels), etc. It is because of these reasons systemic targeting only delivers a small fraction ($< 2\%$) of nanoparticles to the precise tumor location (Bae and Park; 2011), (Wilhelm et al.; 2016).

3.2.2 Cancer Sensitization through Externally Manipulable Nanoswimmers

To overcome the problem of low delivery percentage of nanoparticles, NSs assembled by magnetic nanoparticles have been proposed for direct targeting (Servant et al.; 2015), (Li et al.; 2017). These externally or physically stimulated swarm of NS show encouraging results in cancer diagnostics. The measurable characteristics of NSs such as their trajectories are observed and then externally maneuvered in the best possible direction by using a constant external magnetic field. This tracking (observing) and controlling (maneuvering) of NSs helps them to adopt

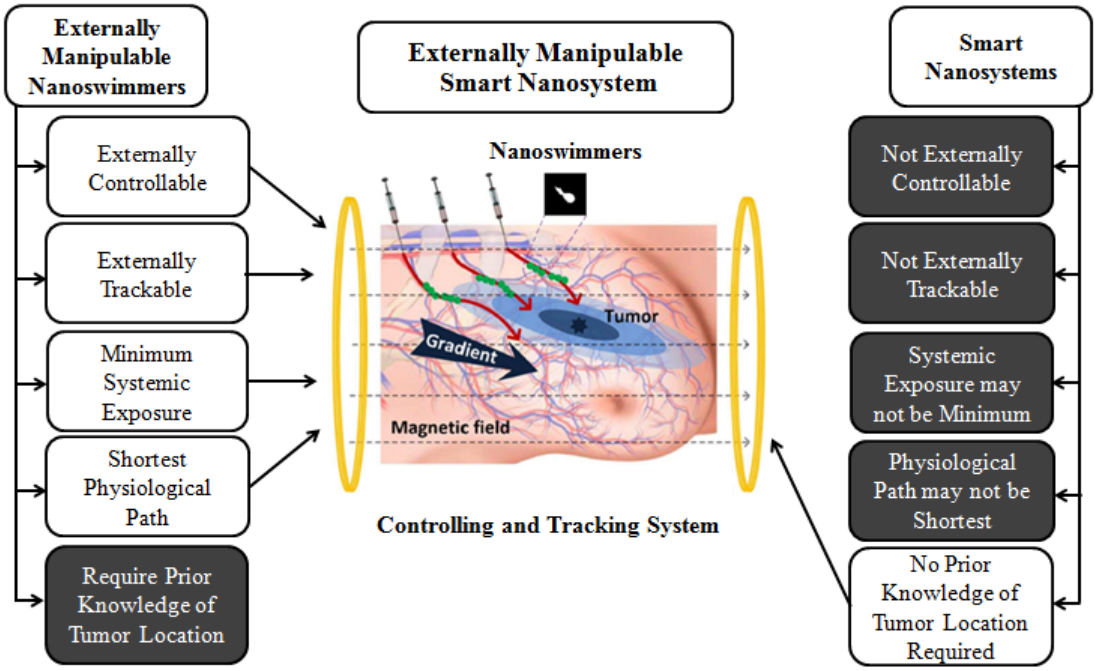

Figure 3.2: Proposed externally manipulable smart nanosystems harvesting positive features (shown in white boxes) from both smart nanosystems and direct targeting employed by externally manipulable nanoswimmers whereas ignoring the limitations (shown in grey boxes) of both systems.

the shortest physiological path and their systemic exposure is minimized. Prior knowledge of the tumor location is required for external tracking and control of NSs. This direct targeting has a number of important benefits as listed in the white boxes on left hand side of Fig. 3.2. It has been shown that up to 55% of drug-containing NSs reach the center of cancerous area (Felfoul et al.; 2016). However, the pre-contrast medical image quality of the diseased area is usually very low, which poses limitation on the usage of NS-assisted direct targeting.

3.2.3 Cancer Sensitization through Smart Nanosystems

Tumor homing can also be amplified with the help of so-called smart nanosystems in which the living host environment is used to assist with the detection of the malignant tissues (Seidi et al.; Apr. 2018). Material and biological properties do change significantly at the nanoscale under the influence of the disease, which can be leveraged to achieve improved diagnostic capability. These smart nanosystems may broadly be classified as environment-responsive and environment-primed (Kwon et al.; 2015). The first category is comprised of nanoparticles that sense and respond to their environment. Peritumoral area is altered by biochemical properties like redox potential, pH, enzymatic activity, and homoeostatic pathways, which highlight the locations of tumors. The second category refers to schemes in which a host environment is administered by external influences such as x-rays, heat, drugs, infrared light or nanoparticles themselves (Maltzahn et al.; 2011). After the host environment is primed, it becomes straightforward to achieve the desired aim of host-environment and nanoparticle-nanoparticle interactions (Ali et al.; 2020a,b). Synthetic nanoparticles can undergo autonomous motions when they extract various energies from the peritumoral region and convert them into mechanical output (Luo et al.; 2018). For example, nanoparticles with minimum computational capability can perform tumor homing and obstacle avoidance in complex human vasculature through simple principles of aggregation and migration. A swarm of nanoparticles passively "sense and share" the gradient-induced structural changes (aggregation), translate them into a push/pull effect which results in tumor-directed locomotion (migration) (Ali et al.; 2021). Such systems do not require prior knowledge of tumor. Tumor targeting is achieved without any

interaction of controlling hardware or clinicians but it suffers from a number of significant disadvantages as shown in the black boxes on right hand side of Fig. 3.2.

3.2.4 Proposed Externally Manipulable Smart Nanosystems

Fig. 3.2 summarizes the pros and cons of both externally manipulable NSs for direct targeting and smart nanosystems. We can harness many advantages with the former system like having minimum systemic exposure using the shortest physiological path. On the other hand, smart nanosystems do not require the knowledge of tumor location. However, they may not follow the shortest path and do not guarantee minimum systemic exposure. So the idea is to combine the desired features of both systems, which are shown as the white boxes in Fig. 3.2. We call the new system *externally manipulable smart nanosystem.* In such a system non-manipulable nanoparticles are replaced by a swarm of NSs such as the ones assembled by iron oxide MNPs (Cheang and Kim; 2015) that provide the features of controllability and trackability.

Biosensing can be achieved through analyzing the observable characteristics of NS in response to the tumor-induced changes in the natural biological environment. For example, MNPs are reliably used to estimate the locations of magnetic contrast through differential medical imaging (Bucci et al.; 2017). In a natural environment, contrast agents accumulate at the target through adequate penetration and retention in the tissue of interest (van et al.; 2020). The large gaps in endothelium of blood vessels facilitate leakage of contrast agents into interstitial space (Maeda et al.; 2013). This phenomenon helps to yield an improved bio-

distribution profile of contrast agents (Kobayashi et al.; 2014) and can be observed externally by noticing NSs when they stop moving.

Our previous work (Chen et al.; 2017; Chen, Ali, Shi and Cheang; 2019; Chen et al.; 2019) develops a theoretical framework for targeting strategies using externally manipulable smart nanosystems under the umbrella of computing-inspired bio-sensitization. In this framework, an optimization variable (such as a NS) tries to find a target (such as the tumor) by iteratively moving through the search domain (such as the tissue region at a high risk of malignancy) under the guidance of an external force (such as a magnetic field to steer NS towards the possible tumor location). In our earlier work, all NSs are steered towards a common direction due to the constraint of a uniform external field (Cheang and Kim; 2015). It results in actuating a NS in the intended direction whereas other NSs also move towards the common (unintended) direction. Hence, there are steering errors at every iteration.

To solve this problem, target sensitization can be achieved through introducing some influential NSs which can help to determine the steering direction for the whole swarm to move towards the target (Goodrich et al.; 2011). One such influential NS can be the leader which is closest to the target. In our natural *in vivo* computation framework, the leader can be selected as the one with the largest tumor-induced physical, chemical or biological transformation. There are several potential candidates which change their properties proportional to the biological gradients. Examples can be temperature-sensitive polymers or liposomes, and pH-responsive micelles. Once the leader is selected, the whole swarm is steered based on the localized estimation of the leader. An alternative approach, in which localized estimations of all NSs are fused together, can provide a solution in finding

the optimal heading direction of the swarm. This fusion can be average-based (all estimations having equal weight) or proportional-based (different weights for different estimations based on some criteria). Another potential approach can be a geolocation-based target detection. The localization of a target that radiates wireless signals is a widely investigated problem (Gavish and Weiss; 1992), (Erol-Kantarci et al.; 2010). The signal sensed by direction-finding sensors can be intersected to find the target location. In natural computation, the swarm of NS can be regarded as biological gradient sensing sensors and their positions are known. These sensors provide direction information of the "radiatin" source (tumor), whose location needs to be estimated.

Another key physical constraint is the loss of NSs inside the human vasculature due to deterioration, diffusion, and moving into unintended vessels, which limits the amount of deposition of NSs in early microcarcinoma. It is thus critical to ensure that NSs can arrive at the tumor site within the shortest possible duration to reduce bio-degradation and scattering. The tumor homing process can be divided into two sub-operations for NSs; biological gradient sensing and position update. The time taken by both these operations in natural computation contribute to the total detection time. The gradient sensing time should be large enough for reliable estimation of the search domain, however the swarm can be moved faster while updating its position to reduce the total detection time.

3.3 Biological Implications of Tumor on Proposed System

Early studies have shown that there are notable heterogeneities in the passive properties of early malignant tumors (Sutherland; 1988). To successfully realize the tumor sensitization framework and address the associated physical constraints, understanding of the tumor microenvironment is very important.

3.3.1 Tumor Vasculature

Microvascular density is lower in tumoral environment of human lungs, colon carcinomas and mammary than their normal tissue counterparts (Eberhard et al.; 2000). For example, microvascular density was found to be only 29% when compared to the vasculature of healthy lung tissues (Nico et al.; 2008). Similarly, normal pituitary gland is more vascular than the pituitary adenomas (Turner et al.; 2000). Moreover, normal tissues are regularly vascularized that result in a homogeneous lattice comprising of straight and rigid cylindrical capillaries joining adjacent nodes. In contrast, tumor vasculature is very complex and chaotic resulting in a sparse network in the peritumoral region. Factors like vessel dilation, angiogenesis, vessel wall degeneration and vessel collapse contribute to a loss of hierarchical organization (Gazit et al.; 1995). Therefore, an invasion percolation method has been used to explain higher fractal dimensions associated with the tumor vasculature. Keeping these facts in mind, a computational model for the possible growth of vasculature around the tumor center is introduced in 3.4.2.

3.3.2 Tumor-induced Biological Gradients

Biological gradients arise from the physical properties of the host environment such as changes in peritumoral vasculature architecture (Baish et al.; 1996; Baish and Jain; 2000), blood flow velocity, and oxygen concentration. Other biological properties such as enzyme reactions and bio-molecular cell structure are transformed due to malignant tumor cells. Moreover, chemical properties such as pH, also change in tumors due to the presence of lactic acid. It is produced to counter the reduction of oxygen supply and other nutrients due to the rapid proliferation of cancerous cells. Alternatively, the host environment can also be primed to induce biological gradients. Gold nanorods, for example, are modified to circulate in blood for longer periods of time and passively accumulate in tumors. They are used to heat tumor tissues by amplifying the absorption of near-infrared energy that is mostly transparent to living tissues. As a result of this hyperthermia, gradient of blood flow velocity is amplified due to the difference in response of normal and tumor microcirculation (Maltzahn et al.; 2011), (Park et al.; 2010). In addition, temperature gradient can also be introduced by local hyperthermia if the tumor is close to the skin.

Materials change their properties at the nanoscale, which enables them to have profound applications. For example, when light is shone on nanocrystals of cadmium selenide (CdSe) in liquid, they glow blue (when size = 2.0 nm), green (2.5 nm), yellow (3.0 nm), orange (3.9 nm), and red (4.2 nm), whereas CdSe itself is a big black crystal. It is not just the color that changes at the nanoscale. In medicine, miniaturization has helped to design nanoparticles, which behave in different interesting manners to tumor-induced biological gradients (Karimi et al.; 2016). For

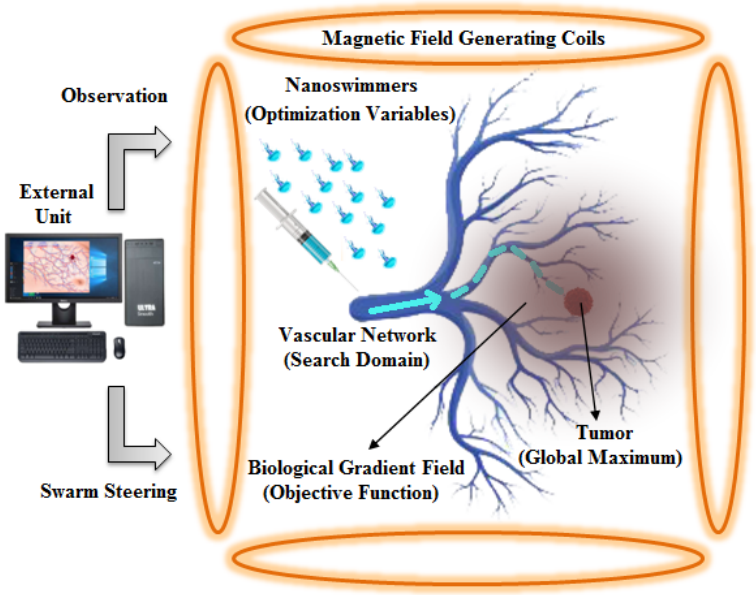

Figure 3.3: Analogy between externally manipulable smart nanosystem driven by biological gradient field and iterative optimization process driven by gradient descent.

example, PNIPAA and its derivatives, commonly known as temperature-sensitive nanopolymers, undergo structural changes due to the hypodermic nature of most malignant tumoral environments (Beija et al.; 2011). Similarly, self-assembled miscelles undergo swelling in an acidic peritumoral region (pH = 6.8) from its stable state in a healthy tissue environment (pH = 7.4) (Li et al.; 2016).

3.4 Mapping from Natural Computing to Mathematical Computing

The NSs-assisted tumor sensitization exhibit a one-to-one correspondence with iterative optimization in mathematical computing.

3.4.1 Relationship between Tumor Sensitization and Iterative Optimization

There is a fascinating analogy between the proposed externally manipulable smart nanosystem and iterative optimization as shown in Fig. 3.3. Firstly, the global maximum of an objective function in iterative optimization corresponds to the epicenter of the tumor. Secondly, the domain of the objective function corresponds to the tissue region under observation or the region-of-interest. Similarly, optimization variables (OVs) in iterative optimization are the swarm of NSs in the smart nanosystem. Both systems rely on gradients to reach the desired location. Movement of the NSs can be externally observed, tracked and if required, can also be maneuvered towards a particular direction through the external unit. An integrated device consisting of multiple pairs of electromagnetic coils approximating the Helmholtz coil system, can be used to generate the rotating magnetic field to actuate the NSs (Cheang et al.; 2017) whereas a weak static magnetic field can be used to orient the NSs in the desired direction (Cheang et al.; 2014). Working on these lines, a wide variety of iterative methods can be applied to the design of an optimal direct targeting strategy. However, natural biosensing presents some unique limitations which distinguish it from the classical optimization process.

As the composition of NSs is based on natural materials, their reaction with the biological search space is inevitable. Hence, search space can be altered as a consequence of its biochemical interactions with NSs. Similarly, the homing in natural environment is in discrete capillaries as compared to a continuous search domain in the classical optimization process. The aforementioned differences are based on the available search space around the target; however, there are also

some fundamental differences in terms of the challenges poised by the natural agents themselves. In natural computation, NSs can only be steered by a common external field. This will cause steering imperfections at every iterative step as the heading direction of one NS may not be the best direction for other NSs in the swarm. Conversely, there is no such limitation in mathematical optimization as all OVs can be updated towards their individual optimal coordinates. Next, interactions between the biological environment and natural homing agents introduce a limitation on the life span of NSs whereas OVs are not consumed in the mathematical operational domain. Strategies discussed in Sections 5.2 and 5.3 address the constraints of a common steering field and finite life span, respectively. Note that while explaining these strategies along with the general framework throughout 3.5, we will be using OVs to represent NSs to avoid any ambiguity.

3.4.2 Discretized Vascular Network

Based on the characteristics of tumoral vasculature outlined in 3.3.1, a vascular network is modelled for computational experiments. Tumor vasculature exhibits a percolation-like structure due to its fractal dimension measurements (Gazit et al.; 1997). Hence, we use invasion percolation method to simulate the sprouting process of tumor vessels (Baish et al.; 1996). In this model, uniformly distributed random values of strength are attached to each point on the square lattice. Then the network is populated so that the lattice points with minimum strength adjacent to the current location (initial starting point) are occupied. The search is continued until a desired occupancy level is attained, which is minimum at the tumor center and increases as we move away from the tumor. All adjacent occupied

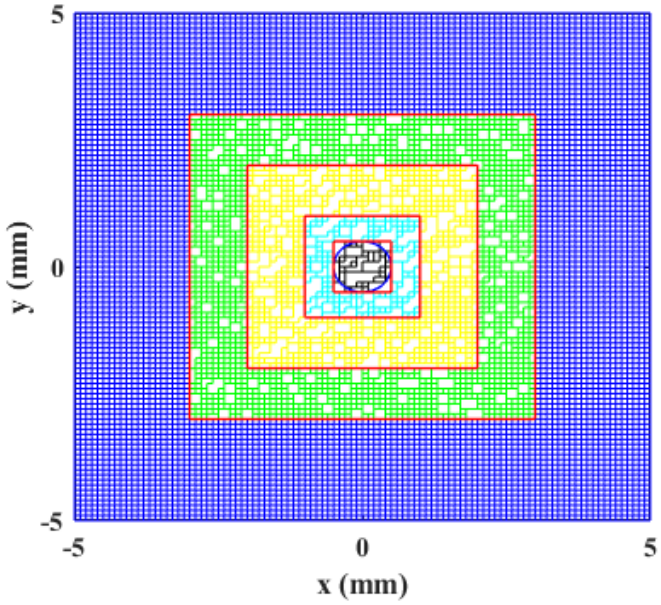

Figure 3.4: Simulated multi-layer vascular network. The level of occupancy on the lattice reduces from 100% *to* 40% *gradually as the distance to the tumor center decreases. The boundaries of the layers are denoted by the red solid lines. The tumor center is denoted by the blue dotted circle.*

points are connected by the blood vessels. In the end, additional edges are added to the developed nodes to ensure that there is no area corresponding to zero blood flow throughout the percolation cluster. Then, a multi-layer vascular network has been developed to depict the fuzzy and blurred boundaries of malignant tumors (Saunders et al.; 2006). This discretized model is required to quantify the diffusive nature of tissue anomaly, which is responsible for the gradual and continuous change in the fractal dimensions across the tumor. The inter-capillary distance of the proposed model shown in Fig. 3.4 is set to be 100 μm and the level of occupancy reduces from 100% to 40% as we move closer to the tumor with layers 1 (green), 2 (yellow), 3 (cyan), and 4 (black) having 85%, 70%, 55%, and 40%, respectively.

3.4.3 Objective Functions

The observable properties of NSs such as pathological vascular structure, redox potential, pH, enzymatic activity or homeostatic regulation form a tumor-induced biological gradient field (BGF). Therefore it is necessary that the *in vivo* BGF should be mapped to an externally measurable objective function by using OVs as a probe for analysis of the host environment. Let f represent the externally measurable objective function defined on the domain $\mathbb{D}$, which represents the high risk tissue under observation. There has not been any widely accepted quantitative model for the above mentioned BGF in the literature. As such, we have taken the sphere, Matyas and Easom functions to evaluate the performance of the smart nanosystem as shown in Fig. 3.5. For example, the hyperthermic nature of most tumors acts as an internal BGF source. Shear stress is also higher in narrowed segments of microvasculature around tumors compared to healthy and wider arterial segments. Therefore, the objective functions in Fig. 3.5 are in general agreement with the qualitative observations made in the existing literature and provide some useful insight into the effectiveness of the proposed direct targeting strategies with varying levels of difficulty. Their arithmetic expressions are

1. *Sphere Function (Bowl-shaped):*

$$f(x,y) = \begin{cases} 1, & \sqrt{x^2+y^2} \leq 0.5 \text{ and } (x,y) \in \mathbb{V} \\ 1 - 0.02\left(x^2+y^2\right), & \\ & \sqrt{x^2+y^2} > 0.5 \text{ and } (x,y) \in \mathbb{V}. \end{cases} \tag{3.1}$$

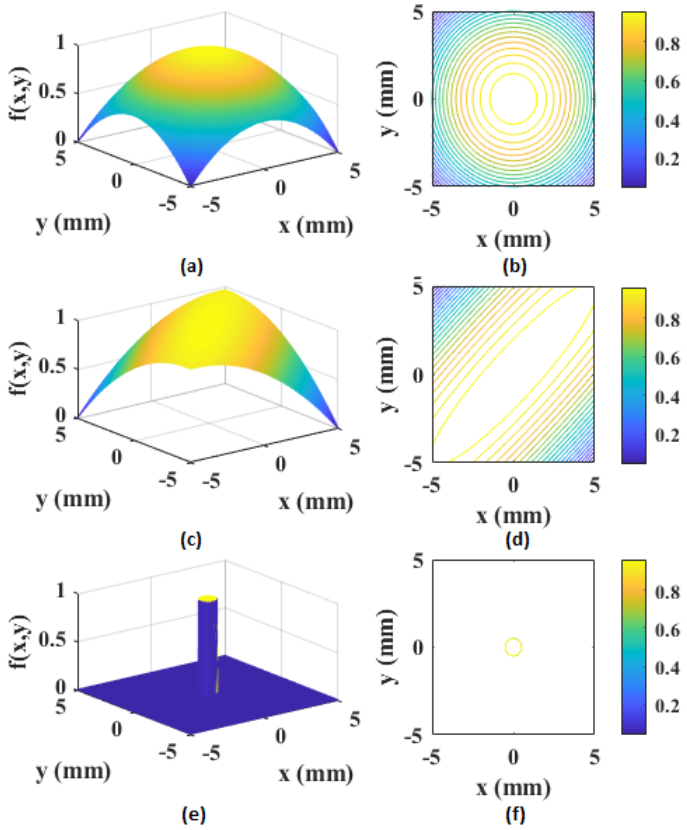

Figure 3.5: Illustration of $f(x, y)$ for three representative objective functions: (a) Sphere function and (b) its contour plot; (c) Matyas function and (d) its contour plot; (e) Easom function and (f) its contour plot. For the objective $f(x, y)$, the maximum is normalized to 1 and the minimum value is 0.

2. *Matyas Function (Plate-shaped):*

$$f(x,y) = \begin{cases} 1, & \sqrt{x^2+y^2} \leq 0.5 \text{ and } (x,y) \in \mathbb{V} \\ 1 - 0.01\left(x^2+y^2\right) + 0.02xy, & \\ & \sqrt{x^2+y^2} > 0.5 \text{ and } (x,y) \in \mathbb{V}. \end{cases} \tag{3.2}$$

3. *Easom function:*

$$f(x,y) = \begin{cases} 1, & \sqrt{x^2+y^2} \leq 0.5 \text{ and } (x,y) \in \mathbb{V} \\ 0.01 + 0.99\cos(3x)\cos(3y) & \\ \qquad \times \exp\left[-\left(9x^2+9y^2\right)\right], & \\ & \sqrt{x^2+y^2} > 0.5 \text{ and } (x,y) \in \mathbb{V}. \end{cases} \tag{3.3}$$

The term $\mathbb{V}$ denotes the discrete vascular network shown in Fig. 3.4. All three landscapes have no local maxima except for the global maximum. The tumor center is denoted by a small circle of radius 0.5 mm located at the origin which represents the highest values of $f(x,y)$. The maximum value of all objective functions is normalized to 1. As we move away from the center, this value starts to decrease. The minimum value at the edges of the landscapes is normalized to 0. After adequate scaling, these extreme values can effectively emulate a large range of BGFs with no loss of generality. Note that the Easom function has no gradient as it abruptly goes from 1 to 0 outside the circle with radius 0.5 mm, representing the worst case scenario. For simplicity, we have just imprinted the objective functions in (3.1), (3.2) and (3.3) on the vascular network $\mathbb{V}$. The blood inflow is assumed to be from the bottom-left corner and the outflow from the top-right corner.

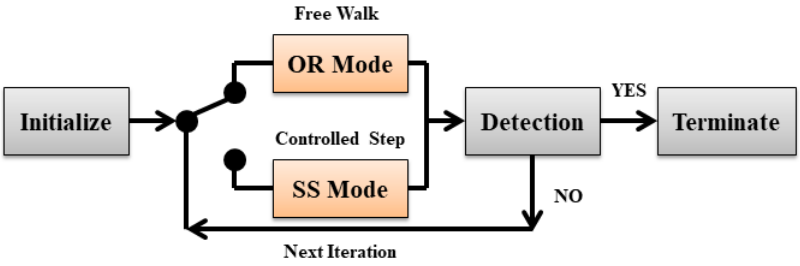

Figure 3.6: Proposed framework where swarm alternately operate in observing-and-recording (OR) mode and swarm-steering (SS) mode. The process keeps on repeating through iterative feedback channel until target is detected.

3.5 Proposed Direct Targeting Strategies through *In Vivo* Computation

3.5.1 Computational Framework

In the proposed framework, a swarm of OVs is randomly deployed in a pre-defined and confined injection area instantaneously. After deployment, the swarm iteratively operates in two basic modes: the observing-and-recording (OR) mode and the swarm-steering (SS) mode as explained below:

1. *Initialization:* Let $\vec{x}_1, \vec{x}_2, \cdots, \vec{x}_N$ represent the locations of N OVs deployed in the initial deployment region -5 mm $\leq x, y \leq -4$ mm. The overall search space is defined by -5 mm $\leq x, y \leq 5$ mm as shown in Fig. 3.4. After deployment, they start searching for the optimal solution based on an iterative algorithm explained in 3.5.3. It is worth mentioning here that the swarm is influenced by the gradient field from a single global optimum in the current framework.

2. *OR Mode:* After initialization, the OVs operate in the common OR mode. It is in this mode that the area around each OV is explored to look for the local gradient. In OR mode, OVs move in the search space without the influence of any guidance, and their movements are observed and recorded to assist in the operation of the SS mode as explained next.

3. *SS Mode:* After the common OR mode in which the swarm wanders freely in the search domain, it goes into the controlled SS mode shown in Fig. 3.6. In the SS mode, the gradients observed in the OR mode are fused together with the help of different strategies explained in 3.5.2. As a result of gradient estimate fusion, the swarm takes a step toward the best direction that will most probably lead to the optimal solution. In natural computation, it corresponds to the application of the external magnetic field to maneuver NSs towards the location of the tumor under the guidance of the BGF as shown in Fig. 3.3. The fusion of gradient estimates helps in resolving a key physical constraint i.e., unidirectional external magnetic field. As the swarm can only be steered in one direction, the individual gradient estimates of NSs need to be fused together to get the possible steering direction for the whole swarm.

4. *Termination:* The swarm switches to operate between the OR and SS modes while homing for the target until detection is achieved. In natural environment, termination of the homing process can be observed externally by noticing NSs when they tend to stop their movement as mentioned in 3.2.4.

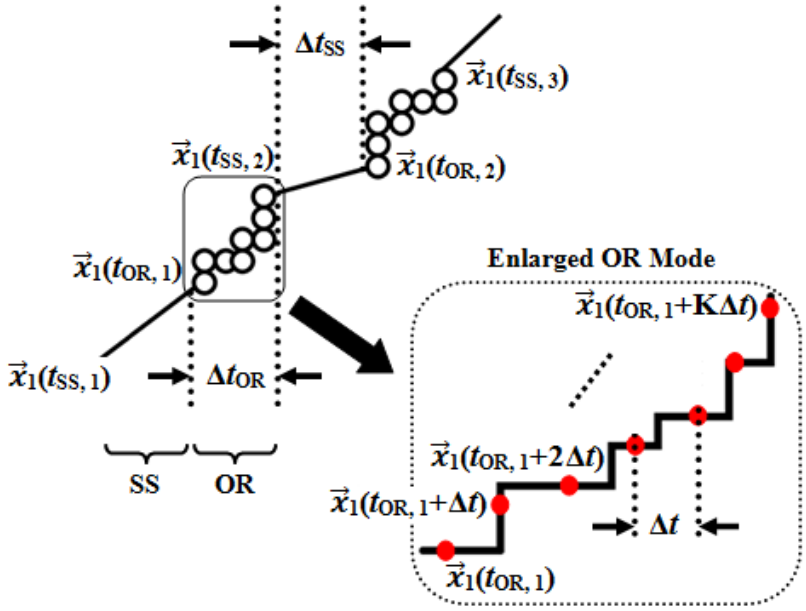

Figure 3.7: Pictorial representation of time division multiplexing of OR and SS modes at top left. Bottom right represents an enlarge illustration of an OR mode in which optimization variable follows a free walk in a zigzag pathway, $\vec{x}_1(t_{\mathrm{OR},1})$, $\vec{x}_1(t_{\mathrm{OR},1}+\Delta t)$, $\cdots$, $\vec{x}_1(t_{\mathrm{OR},1}+K\Delta t)$ with Δt being the observation time interval.

3.5.2 Swarm Steering using MEF for Global Direction Finding

In the OR mode, each OV follows a free and uncontrolled walk in the discrete vascular network shown in Fig. 3.4; $\vec{x}_1(t_{\mathrm{OR},1})$, $\vec{x}_1(t_{\mathrm{OR},1}+\Delta t)$, $\cdots$, $\vec{x}_1(t_{\mathrm{OR},1}+K\Delta t)$, $\vec{x}_1(t_{\mathrm{SS},2})$, where $\Delta t = (t_{\mathrm{SS},2}-t_{\mathrm{OR},1})/(K+1)$ as illustrated in Fig. 3.7. Subsequently, the direction of the gradient is estimated by

$$\begin{aligned}\theta_1(t_{\mathrm{SS},2}) &= \angle\left(\nabla f\left(\vec{x}_1(t_{\mathrm{OR},1})\right)\right)\\ &\approx \angle\left(\vec{x}_1(t_{\mathrm{OR},1}+k_1\Delta t)-\vec{x}_1(t_{\mathrm{OR},1}+k_2\Delta t)\right),\end{aligned} \tag{3.4}$$

and

$$(k_1, k_2) = \underset{k_1', k_2'}{\operatorname{argmax}} \frac{\left[f\left(\vec{x}_1\left(t_{\mathrm{OR},1} + k_1'\Delta t\right)\right) - f\left(\vec{x}_1\left(t_{\mathrm{OR},1} + k_2'\Delta t\right)\right)\right]}{\left\| \vec{x}_1\left(t_{\mathrm{OR},1} + k_1'\Delta t\right) - \vec{x}_1\left(t_{\mathrm{OR},1} + k_2'\Delta t\right)\right\|_2}, \quad \text{where } k_1' > k_2' \text{ and } k_1', k_2' \in \{0, 1, \cdots, K\}. \tag{3.5}$$

Note that $\|\cdot\|_2$ is the ℓ_2 norm and K represents the total number of random steps in a single OR mode. Hence $\theta_1(t_{\mathrm{SS}}), \theta_2(t_{\mathrm{SS}}), \cdots, \theta_N(t_{\mathrm{SS}})$, can be visualized as the directions of localized gradient estimations by N OVs. For the collective swarm locomotion through uniform steering force, we need to find the desired direction which ensures the maximum number of OVs reaching the target. We propose the MEF strategy for swarm steering which tries to find the global estimate $\theta_G(t_{\mathrm{SS}})$, at time t_{SS}, using the localized gradient information through the following optimization metric:

- *Mean Angular Misalignment:* If the actual target location is $\vec{x}_{T,act}$, then the aligned heading direction $\theta_A(t_{\mathrm{SS}})$ is the angle between the x-axis and the vector defined by $\vec{x}_{T,act} - \vec{\epsilon}(t_{\mathrm{SS}})$, where $\vec{\epsilon}(t_{\mathrm{SS}})$ is the swarm center defined as

$$\vec{\epsilon}(t_{\mathrm{SS}}) = \frac{1}{N}\sum_{i=1}^{N} \vec{x}_i(t_{\mathrm{SS}}). \tag{3.6}$$

  The difference between the aligned and estimated heading directions can be represented as

$$\phi(t_{\mathrm{SS}}) = |\theta_A(t_{\mathrm{SS}}) - \theta_G(t_{\mathrm{SS}})|. \tag{3.7}$$

Hence, a $\theta_G(t_{\mathrm{SS}})$ which ensures minimum *mean angular misalignment* $\frac{1}{L}\sum_{l=1}^{L}\phi(t_{\mathrm{SS},l})$ is the desirable estimate. Here, the index l represents the l^{th} SS operation and L is the total number of SS operations performed in the entire tumor homing process.

To solve this problem, different swarm steering strategies are outlined in 3.2.4. They are realized for tumor sensitization problem as below:

1. *Leader-based Swarm Steering:* During the OR mode, each OV estimates the local gradient and its fitness is evaluated in the search space which is the largest value of the objective functions shown in Fig 3.5. The uniform steering direction for the swarm depends upon the highest ranked OV, having the highest fitness value among all OVs in the swarm. So

$$\begin{aligned} &\theta_G^L\left(t_{\mathrm{SS}}\right) = \theta_{i^*}(t_{\mathrm{SS}}), \\ &\text{such that } i^* = \underset{i}{\operatorname{argmax}}\, f\left(\vec{x}_i\left(t_{\mathrm{OR}} + K\Delta t\right)\right), \\ &\text{where } \theta_{i^*} = \angle\left(\nabla f\left(\vec{x}_{i^*}\right)\right) \text{ and } i = 1, \cdots, N. \end{aligned} \tag{3.8}$$

$\theta_1(t_{\mathrm{SS}}), \theta_2(t_{\mathrm{SS}}), \cdots, \theta_N(t_{\mathrm{SS}})$ are the directions of localized gradients learned by the OVs for the SS mode and $\vec{x}_i\left(t_{\mathrm{OR}} + K\Delta t\right)$ represents the position of OV after the final step in the OR mode. Existing models in the literature exhibit a direct relationship between the number of leaders and the swarm size for guiding the swarm. However, in the current work, there can be only one leader due to the limitation of the unidirectional magnetic field. Also note that as the selection criterion for the leader depends upon the largest value of the objective function (i.e., the OV which is closest to the target), any

OV can be selected as the leader of the swarm. After each iteration, current locations of all OVs homing in the search space are observed to determine the new leader.

2. *Weight-based Swarm Steering:* Alternatively, every OV in the swarm can contribute in finding the global heading direction $\theta_G(t_{\mathrm{SS}})$, if all the locally learned gradients by OVs are somehow fused together. One combining approach for localized estimations can be through proportional weighted fusion (PWF). During PWF, learned gradients from all the OVs may be fused together such that the weight of each estimate is proportional to the value of fitness in representative objective functions outlined in 3.4.3. Hence

$$\theta_G^{PWF}(t_{\mathrm{SS}}) = \sum_{i=1}^{N} \varphi_i(t_{\mathrm{SS}})\, \theta_i(t_{\mathrm{SS}}), \tag{3.9}$$

where $\varphi_i(t_{\mathrm{SS}})$ are the weighting factors such that

$$\varphi_i(t_{\mathrm{SS}}) = \frac{f\left(\vec{x}_i\left(t_{\mathrm{OR}} + K\Delta t\right)\right)}{\sum_{i=1}^{N} f\left(\vec{x}_i\left(t_{\mathrm{OR}} + K\Delta t\right)\right)}. \tag{3.10}$$

A much simpler approach in which all the OVs contribute with their localized estimations, is to assign equal weights to their estimated gradients and fuse them to form $\theta_G(t)$ for the whole swarm. We call it equal weighted fusion (EWF). This strategy is unrestrained of fitness-dependent weighted allocation as each estimation effectively has the same weight. The overall swarm heading direction is simply the mean of individual estimated gradients of the OVs.

$$\theta_G^{EWF}(t_{\mathrm{SS}}) = \frac{1}{N} \sum_{i=1}^{N} \theta_i(t_{\mathrm{SS}}). \tag{3.11}$$

It is worth mentioning here that the global heading direction for the swarm may or may not be the best direction for a particular OV.

3. *Geolocation-based Swarm Steering:* In the least-square-position-estimation (LSPE) method (Pages-Zamora et al.; 2002), the target estimation problem is translated into a linear mathematical problem. As demonstrated in Fig. 3.8, the target is located at $\vec{x}_T = (x_T, y_T)$, whereas the i^{th} OV position is $\vec{x}_i(t_{\text{SS}}) = [x_i(t_{\text{SS}}), y_i(t_{\text{SS}})]$ with its estimated gradient as $\theta_i(t_{\text{SS}})$. The LSPE method estimates the target location (Raju et al.; 2016) as

$$\vec{x}_{est}(t_{\text{SS}}) = \begin{bmatrix} x_{est}(t_{\text{SS}}) \\ y_{est}(t_{\text{SS}}) \end{bmatrix} = \left[\mathbf{H}_\theta^T \mathbf{H}_\theta\right]^{-1} \mathbf{H}_\theta^T \mathbf{A}_\theta, \tag{3.12}$$

where

$$\mathbf{H}_\theta = \begin{bmatrix} -\sin\theta_1(t_{\text{SS}}) & \cos\theta_1(t_{\text{SS}}) \\ -\sin\theta_2(t_{\text{SS}}) & \cos\theta_2(t_{\text{SS}}) \\ \vdots & \vdots \\ -\sin\theta_N(t_{\text{SS}}) & \cos\theta_N(t_{\text{SS}}) \end{bmatrix} \tag{3.13}$$

and

$$\mathbf{A}_\theta = \begin{bmatrix} -x_1\sin\theta_1(t_{\text{SS}}) + y_1\cos\theta_1(t_{\text{SS}}) \\ -x_2\sin\theta_2(t_{\text{SS}}) + y_2\cos\theta_2(t_{\text{SS}}) \\ \vdots \\ -x_N\sin\theta_N(t_{\text{SS}}) + y_N\cos\theta_N(t_{\text{SS}}) \end{bmatrix} \tag{3.14}$$

whereas, the heading direction, $\theta_G(t_{\text{SS}})$ of the swarm through (3.11) will be the angle between the x-axis and the vector defined by $\vec{x}_{est}(t_{\text{SS}}) - \vec{\epsilon}(t_{\text{SS}})$, where $\vec{\epsilon}(t)$ is again the swarm center.

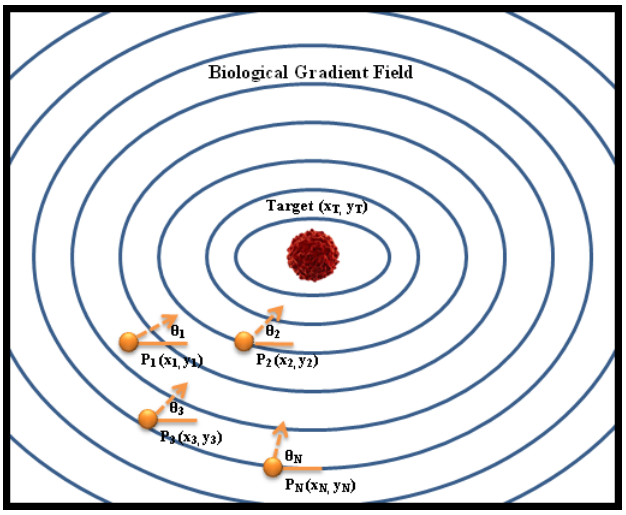

Figure 3.8: Illustration of least-square-position-estimate (LSPE) method in which swarm of nanoswimmers with localized gradient estimations perform target homing through the aid of biological gradient field.

Using (3.6), the aforementioned swarm steering strategies are compared by taking the mean angular misalignment as the optimization parameter.

3.5.3 Swarm Steering using MDGD for Search Acceleration

In order to achieve successful target homing, the total detection time should always be less than the life span of NSs as mentioned in 3.2.4. For natural computing, learning the environment and location update are time-consuming steps, contrary to the mathematical computing where such operations are performed instantly. The direct targeting strategy inspired by the MDGD starts with generic optimization variables $OV_1, OV_2, \cdots, OV_N$ located at $\vec{x}_1, \vec{x}_2, \cdots, \vec{x}_N$ attempting to find the global maximum $f(\vec{x}^*)$. For the framework shown in Fig. 3.6, consider the sequence $\vec{x}_1\left(t^{(1)}_{\mathrm{OR},1}\right), \vec{x}_1\left(t^{(2)}_{\mathrm{OR},1}\right), \vec{x}_1\left(t^{(3)}_{\mathrm{OR},1}\right), \cdots, \vec{x}_1\left(t^{(K)}_{\mathrm{OR},1}\right)$ representing the positions of OV_1 observed by the external system. Here, $\vec{x}_1\left(t^{(k)}_{\mathrm{OR},1}\right)$ represents the

location of the OV_1 after k^{th} step during the zigzag movement in the OR mode as illustrated in Fig. 3.7. During each OR mode, OV_1 goes through K OR processes with the velocity v_{OR}. The variable then needs to update its position during SS mode moving with the velocity v_{SS}. In the classical gradient descent, for location update, we have

$$\vec{x}_1\left(t_{\text{OR},1}^{(k)}\right) = \vec{x}_1\left(t_{\text{OR},1}^{(k-1)}\right) + \gamma_{k-1}\nabla f\left(\vec{x}_1\left(t_{\text{OR},1}^{(k-1)}\right)\right) \quad \text{where} \quad k = 2, 3, \cdots, K. \tag{3.15}$$

However, in our case, where location updating is interrupted by multiple OR and SS modes, the position update is modified as

$$\vec{x}_1\left(t_{\text{OR},2}^{(1)}\right) = \vec{x}_1\left(t_{\text{SS},2}\right) + \gamma_k\nabla f\left(\vec{x}_1\left(t_{\text{SS},2}\right)\right). \tag{3.16}$$

The gradient $\nabla f\left(\vec{x}_1\left(t_{\text{SS},2}\right)\right)$ is estimated through K OR processes. If the gradient is not changing much from $t_{\text{OR},1}^{(k)}$ to $t_{\text{OR},1}^{(k+1)}$, it can be estimated as

$$\nabla f\left(\vec{x}_1\left(t_{\text{SS},2}\right)\right) \approx \max_{k=1,2,\cdots,K}\left\{\nabla f\left(\vec{x}_1\left(t_{\text{OR},1}^{(k)}\right)\right)\right\}. \tag{3.17}$$

Otherwise, only the final gradient estimate is used such that

$$\nabla f\left(\vec{x}_1\left(t_{\text{SS},2}\right)\right) \approx \left\{\nabla f\left(\vec{x}_1\left(t_{\text{OR},1}^{(K)}\right)\right)\right\}. \tag{3.18}$$

Suppose that $f\left(\vec{x}\right)$ is convex and $\nabla f\left(\vec{x}\right)$ is Lipshitz, the step size γ_k can be chosen to guarantee convergence to a global optimum by using the Brazilai-Borwein method (Barzilai and Borwein; 1988).

To meet the physical constraint imposed by the finite life span, it is worth noting that OVs are moved more swiftly in the SS mode as compared to the OR mode i.e. $v_{\mathrm{SS}} > v_{\mathrm{OR}}$. This is because the movement of the OVs during the OR mode should be steady in order to obtain accurate and precise gradient estimations. As a consequence, the distance covered in the SS mode should be as large as possible to reduce the total detection time. We propose a memory-driven approach which helps to accelerate the traditional memory-less gradient descent (MLGD) (Chen, Ali, Shi and Cheang; 2019) in the relevant direction through dampening of oscillations (see Fig. 2(b) in (Ruder; 2016)). Faster detection is achieved by adding an α-term (memory) of the update vector $\beta(t_{\mathrm{SS},L-1})$ of the past time step to the current update vector $\beta(t_{\mathrm{SS},L})$ as

$$\beta(t_{\mathrm{SS},L}) = \left(\sum_{l=1}^{L-1} \zeta_l \beta(t_{\mathrm{SS},l}) \right) + \gamma_k \nabla f\left(\vec{x}_1\left(t_{\mathrm{SS},L-1}\right)\right), \tag{3.19}$$

where

$$\zeta_l = \alpha\, e^{-\frac{l}{\lambda L}}. \quad l = 1, 2, 3, \cdots, L. \tag{3.20}$$

Here, the index l represents the l^{th} SS operation and L is the number of SS steps till the current state. The term ζ is called the *forgetting factor* and has an exponential term which determines the weight given to the past time SS steps. For $\lambda \to 0$, zero weight is assigned to the older SS steps for $l \geq 2$. The larger λ is, the larger is the contribution of previous SS steps to the ζ. As $\lambda \to \infty$, an equal weight is assigned to all the past SS steps. For simulation studies, different numerical values are assigned to α ($\alpha \geq 0$), where $\alpha = 0$ corresponds to the special case of memory-less gradient descent. Finally, the position update is expressed as

$\vec{x}_1\,(t_{\mathrm{OR},L}) = \vec{x}_1\,(t_{\mathrm{SS},L}) + \beta(t_{\mathrm{SS},L})$. When using the MDGD strategy, we actually push our OV in the direction of maximum gradient. The step size for the SS mode increases for dimensions whose gradients point in the same directions that results in faster convergence to the global maximum (i.e. tumor location) with reduced oscillations.

3.6 Performance Analysis

We use MATLAB® as the simulation tool to evaluate the tumor homing and targeting performance of the proposed swarm steering strategies. The results are compared with the brute-force search (i.e., systemic targeting) for analysis purpose.

3.6.1 Computational Results for MEF Strategies

3.6.1.1 Simulation Setup

The objective functions shown in Fig. 3.5 are overlaid on the multi-layer vascular network presented in 3.4.2. The deployment region is set to be -5 mm $\leq x, y \leq -4$ mm. The maximum search time allowed is set to be 200 s for each run of 1000 simulations. To analyze the targeting performance of the aforementioned swarm steering strategies, the swarm consists of five OVs. The target is considered to be detected if 60% of the OVs successfully reach the target and the searching process is stopped. It is assumed that the remaining OVs will be guided towards the target if they have not overshoot the tumor location. The overall targeting efficiency (η) of the system is calculated as the ratio of the number of OVs that have detected

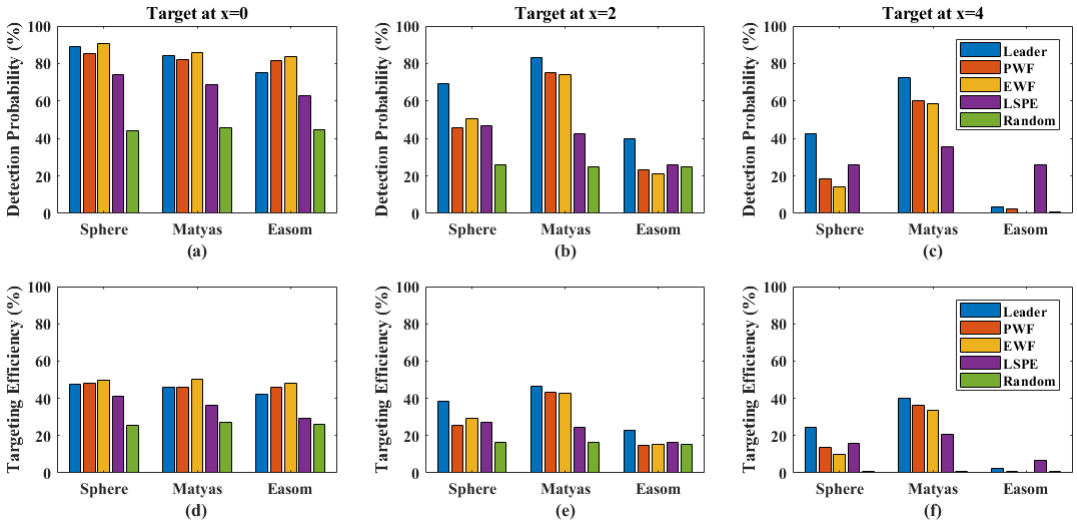

Figure 3.9: Performance comparison of MEF-based swarm steering strategies for the sphere, Matyas and Easom landscapes when: target is at the center of search space ***(a,d)****, target is off-centered at $x = 2$* ***(b,e)*** *and $x = 4$* ***(c,f)****. The blood flow is assumed to be from bottom left to top right. EWF-based swarm steering outperforms other strategies when target is in the direction of blood flow (tumor at center) whereas leader-based swarm steering gives best results when target is not in the direction of blood flow (tumor off-centered).*

the tumor to the total number of deployed OVs over the aforementioned simulation settings. The swarm spreadness δ is given by

$$\delta = \sum_{l=1}^{L} \sum_{i=1}^{N} \|\vec{\epsilon}(t_{\mathrm{SS},l}) - \vec{x}_i(t_{\mathrm{SS},l})\|_2, \tag{3.21}$$

where $\|\cdot\|_2$ is the ℓ_2 norm, is also used as the performance measure. Cytotoxic effect is minimized when the swarm remains compact.

Table 3.1: Mean Angular Misalignment of MEF Strategies (Target Centered)

MEF Strategies	***Mean Angular Misalignment*** ϕ		
	Sphere	**Matyas**	**Easom**
Leader	8.47	10.07	11.60
PWF	7.29	9.35	10.38
EWF	7.07	8.14	10.46
LSPE	10.70	12.25	13.60
Random	20.79	21.41	22.57

3.6.1.2 Simulation Results

Initial statistical results are outlined in Table 3.1 which demonstrate that the mean angular misalignment (ϕ) is minimized for weight-based fusion strategies. For simplicity, results are shown only for the case when the target is at the center of the landscapes. In terms of search space, the sphere landscape with smooth BGF leads to smaller ϕ than the Matyas and Easom landscapes. As expected, random steering (brute-force search) has the largest ϕ as it follows systemic targeting to detect the tumor.

Fig. 3.9 represents the performance of the leader-based, weight-based (PWF and EWF) and LSPE-based swarm steering strategies compared to random steering for target detection. Fig. 3.9(a,d) shows that the EWF strategy achieves the best detection and targeting efficiency ($P_D = 90.50\%$ and $\eta = 49.74\%$) when the target is at the center of the search space. Hence, for a symmetrical swarm-target orientation, the mean of individual estimates provides the best results. However, when the swarm-target orientation is non-symmetrical i.e., target is off-center

(moved to $x = 2$ mm and 4 mm), leader-based swarm steering outperforms other strategies for all three landscapes as shown in Fig. 3.9(b,c,e and f). Nevertheless, all MEF-based swarm steering strategies perform better than the random steering of the swarm.

Table 3.2 outlines the statistical results related to swarm spreadness (δ) for the MEF-based swarm steering strategies. Again for simplicity, the results are for target being at the center of landscapes. δ is selected as the performance measure (as mentioned in 3.1.1) because we want the swarm to remain closely packed. Weight-based (PWF and EWF) swarm steering shows the lowest values of δ whereas random search gives the maximum swarm spreadness. Comparing the search landscapes, the swarm remains more compact for the sphere function than the Easom and Matyas landscapes.

Table 3.2: Swarm Spreadness of MEF Strategies (Target Centered)

MEF Strategies	***Swarm Spreadness*** δ		
	Sphere	**Matyas**	**Easom**
Leader	25.94	26.98	29.67
PWF	23.87	25.35	27.47
EWF	23.85	24.92	26.15
LSPE	25.89	27.83	32.62
Random	31.25	30.37	31.39

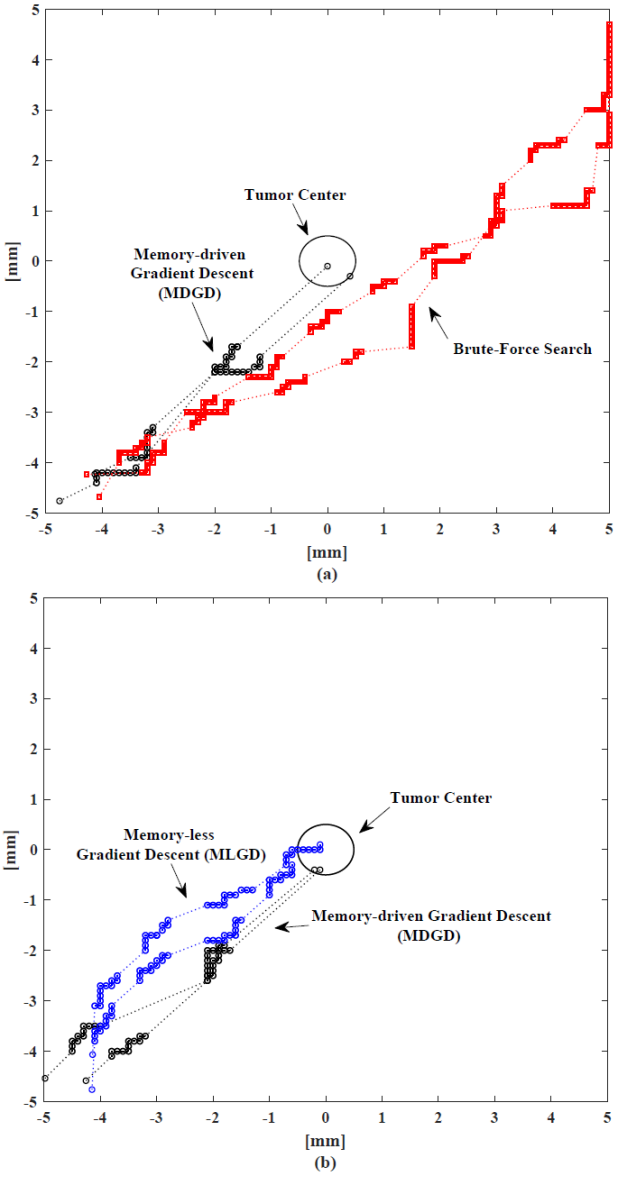

Figure 3.10: Trajectories of optimization variables for: (a) "○" - MDGD-inspired direct targeting and "□" - Brute-force search (b) "○" - MLGD-inspired direct targeting and "○" - MDGD-inspired direct targeting.

3.6.2 Computational Results for MDGD-based Direct Targeting

3.6.2.1 Simulation Setup

As the prime focus is on fast detection of the target through MDGD-based direct targeting, the number of OVs is reduced to two for simplicity. Moreover, as EWF

performs best in terms of detection probability and targeting efficiency, it is used to accelerate the searching process through MDGD. It is assumed that the OVs move faster during the steering process in the SS mode (i.e. $v_{\mathrm{SS}} = 120\ \mu$m/s) as compared to the gradient estimation in the OR mode (i.e. $v_{\mathrm{OR}} = 80\ \mu$m/s). Again, the maximum search time allowed is set to be 200s for each run of 1000 simulations. Finally, the limiting case of $\lambda \to 0$ in Eq. (3.19) is used for numerical analysis while focusing on the impact of α-term on system performance. The searching process is stopped if any of the OVs reach the cancer center assuming that the other OV will be guided to the tumor center if it has not overshoot the tumor location. For the brute-force search, each OV goes through a random walk in the lattice. The brute-force search does not use the information related to gradients to look for the tumor and the OV stops searching if it reaches the tumor center. However, the other OVs continue their random drift in the absence of an external guidance.

3.6.2.2 Simulation Results

Fig. 3.10(a) shows the typical trajectories of OVs for the landscape of the sphere function when both the proposed MDGD-inspired direct targeting and the brute-force search are considered. As demonstrated, the proposed strategy successfully detects the tumor center whereas the brute-force search fails to do so. Fig. 3.10(b) shows the comparisons of gradient descent with and without the memory. As illustrated, MDGD goes into the OR mode (represented with a cluster of points in Fig. 3.10, detailed SS and OR modes in Fig. 3.7) just twice before it detects the target whereas the classical MLGD requires four OR modes consuming more time to reach the target.

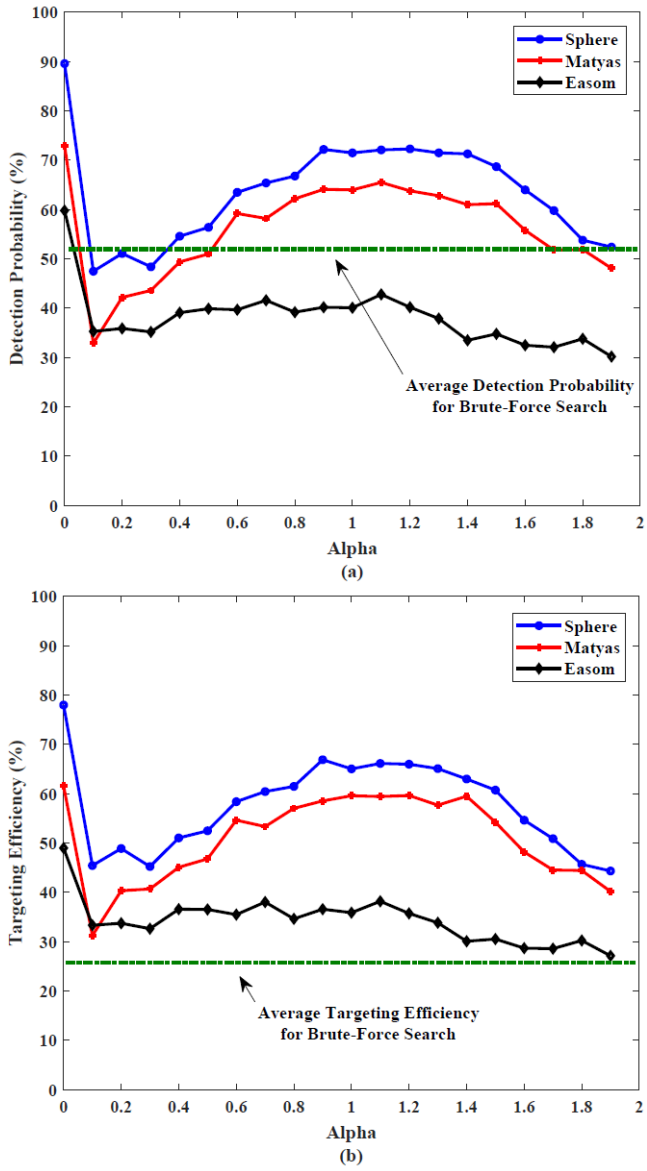

Figure 3.11: Impact of α-term (memory) on system performance for accelerated search through memory-driven gradient descent (MDGD): (a) Probability Detection (P_D) and (b) Targeting Efficiency (η).

The impact of α-term (memory) on the detection probability and targeting efficiency is shown in Fig. 3.11(a and b) respectively. The spike in performance

at $\alpha = 0$ for all landscapes is associated with the absence of any memory-driven component (classical MLGD). However, this better performance of MLGD is at the expense of longer sensitization time. For MDGD, P_D and η follow bell-shaped curves and give better results if $0.8 \leq \alpha \leq 1.4$ for the sphere and Matyas landscapes. The performance of the Easom function is the worst and follows a straight line as expected from a gradient-less search domain. Specifically, graphs show that for the sphere landscape at $\alpha = 0.9$, system performance is the best ($P_D = 72.60\%$ and $\eta = 66.90\%$). It is also evident that the sphere landscape always outperforms the Matyas and Easom landscapes at any particular value of α. Finally, P_D becomes lower than the average detection probability of brute-force search for $\alpha < 0.5$ and $\alpha > 1.8$; however η remains better than the brute-force search for all values of α. In summary, α should be within the range $0.8 \leq \alpha \leq 1.4$ for optimum performance of the proposed strategy.

Finally, Fig. 3.12 represents the histograms of search time for all the landscapes. The graphs demonstrate that the MDGD-based strategy detects the tumor faster as compared to MLGD. This is due to the fact that the current step taken by the OV considers the direction of the previous steps taken by it. If it finds that the direction is correct (i.e. towards the global maximum), it increases its step size resulting in faster target detection. However, there is a trade off between detection performance and search time of both strategies. MDGD starts detecting the target at around 50 seconds whereas MLGD detects at around 100 seconds. However, MDGD detection performance ($P_D = 72.60\%$ and $\eta = 66.90\%$) is lower than MLGD ($P_D = 89.60\%$ and $\eta = 78\%$) for the sphere landscape. The same trend is observed in the Matyas and Easom landscapes. The search time of 200s indicates that none of the two OVs are able to detect the tumor.

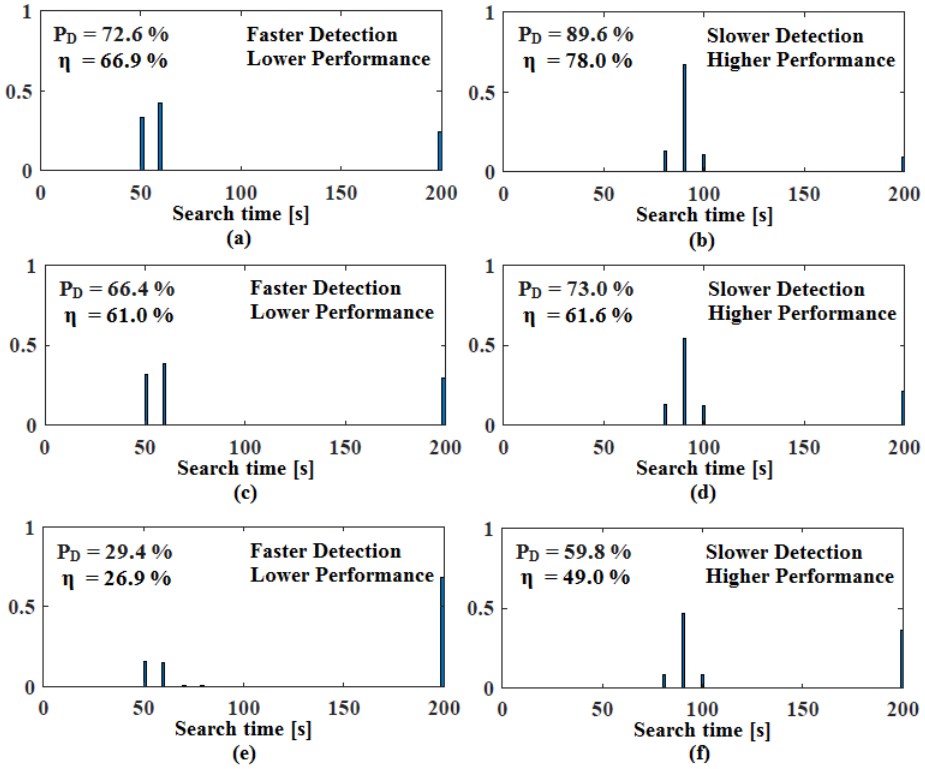

Figure 3.12: Histograms of search time for direct targeting inspired by MDGD in: (a) Sphere landscape, (c) Matyas landscape, (e) Easom landscape, and for MLGD in: (b) Sphere landscape, (d) Matyas landscape, (f) Easom landscape.

3.7 Conclusion

We have proposed novel MEF-based swarm steering strategies to address the physical constraint of unidirectional magnetic field. We have shown by computational experiments that EWF-based swarm steering provides the best solution (with $P_D = 90.50\%$ and $\eta = 49.74\%$ compared to the brute force search with $P_D = 41.29\%$ and $\eta = 20.74\%$) when tumor is in the direction of blood flow whereas leader-based swarm steering outperforms other strategies for non-symmetric NS-tumor orientations. Statistical results also illustrate that uniform swarm steering

direction, obtained from equal weighted fusion of individual estimates, ensures minimum swarm spreadness. MDGD-inspired search acceleration method for tumor sensitization addresses the challenge of finite life span of NSs. Simulation studies demonstrate that the proposed MDGD strategy results in faster localization of the tumor (approximately 50% less time) than the classical MLGD and brute force search.

In future, the proposed framework may be applied to multi-modal optimization where multiple tumors are present in the region-of-interest. Furthermore, the proposed strategies and objective functions should be validated by real experiments to justify their clinical relevance. Finally, apart from memory-based gradient descent, other optimization algorithms may also be looked in to achieve more efficient tumor sensitization.

References

Ali, M., Chen, Y. and Cree, M. J. (2021). Autonomous in vivo computation in internet of nano bio things, *IEEE Internet of Things Journal* **9**(8): 6134–6147.

Ali, M. et al. (2020a). Bio-inspired self-regulated in-vivo computation for smart cancer detection, *2020 IEEE 20th International Conference on Nanotechnology (IEEE-NANO)*, IEEE, pp. 304–309.

Ali, M. et al. (2020b). Self-regulated and co-ordinated smart tumor homing for complex vascular networks, *2020 42nd Annual International Conference of the IEEE Engineering in Medicine & Biology Society (EMBC)*, IEEE, pp. 378–381.

Bae, Y. H. and Park, K. (2011). Targeted drug delivery to tumors: myths, reality and possibility, *J. Control. Release* **153**(3): 198–205.

Baish, J. W. and Jain, R. K. (2000). Fractals and cancer, *Cancer research* **60**(14): 3683–3688.

Baish, J. W. et al. (1996). Role of tumor vascular architecture in nutrient and drug delivery: an invasion percolation-based network model, *Microvascular Research* **51**(3): 327–346.

Barzilai, J. and Borwein, J. M. (1988). Two-point step size gradient methods, *IMA Journal of Numerical Analysis* **8**(1): 141–148.

Beija, M., Marty, J.-D. and Destarac, M. (2011). Thermoresponsive poly (n-vinyl caprolactam)-coated gold nanoparticles: sharp reversible response and easy tunability, *Chemical Communications* **47**(10): 2826–2828.

Bucci, O. M., Bellizzi, G., Borgia, A., Costanzo, S., Crocco, L., Di Massa, G. and Scapaticci, R. (2017). Experimental framework for magnetic nanoparticles enhanced breast cancer microwave imaging, *IEEE Access* **5**: 16332–16340.

Cheang, U. K., Dejan, M., Choi, J. and Kim, M. (2014). Towards model-based control of achiral microswimmers, *ASME 2014 Dynamic Systems and Control Conference*, American Society of Mechanical Engineers Digital Collection.

Cheang, U. K. and Kim, M. J. (2015). Self-assembly of robotic micro-and nanoswimmers using magnetic nanoparticles, *Journal of Nanoparticle Research* **17**(3): 145.

Cheang, U. K. et al. (2017). Feedback control of an achiral robotic microswimmer, *J. of Bionic Eng.* **14**(2): 245–259.

Chen, Y., Ali, M., Shi, S. and Cheang, U. K. (2019). Biosensing-by-learning direct targeting strategy for enhanced tumor sensitization, *IEEE Transactions on Nanobioscience* **18**(3): 498–509.

Chen, Y., Shi, S., Yao, X. and Nakano, T. (2017). Touchable computing: computing-inspired bio-detection, *IEEE Transactions on Nanobioscience* **16**(8): 810–821.

Chen, Y. et al. (2019). Direct targeting strategy for smart cancer detection as natural computing, *ICC 2019-2019 IEEE International Conference on Communications (ICC)*, IEEE, pp. 1–6.

Eberhard, A. et al. (2000). Heterogeneity of angiogenesis and blood vessel maturation in human tumors: implications for antiangiogenic tumor therapies, *Cancer Research* **60**(5): 1388–1393.

Erol-Kantarci, M., Mouftah, H. T. and Oktug, S. (2010). Localization techniques for underwater acoustic sensor networks, *IEEE Communications Magazine* **48**(12): 152–158.

Felfoul, O. et al. (2016). Magneto-aerotactic bacteria deliver drug-containing nanoliposomes to tumour hypoxic regions, *Nat. Nanotechnol.* **11**(11): 941–947.

Gavish, M. and Weiss, A. J. (1992). Performance analysis of bearing-only target location algorithms, *IEEE Transactions on Aerospace and Electronic Systems* **28**(3): 817–828.

Gazit, Y. et al. (1995). Scale-invariant behavior and vascular network formation in normal and tumor tissue, *Physical Review Letters* **75**(12): 2428.

Gazit, Y. et al. (1997). Fractal characteristics of tumor vascular architecture during tumor growth and regression, *Microcirculation* **4**(4): 395–402.

Goodrich, M. A. et al. (2011). Enabling human interaction with bio-inspired robot teams: Topologies, leaders, predators, and stakeholders.

Hori, S. S. and Gambhir, S. S. (2011). Mathematical model identifies blood biomarker–based early cancer detection strategies and limitations, *Sci. Trans. Med.* **3**(109): 109ra116–109ra116.

Karimi, M. et al. (2016). Smart micro/nanoparticles in stimulus-responsive drug/gene delivery systems, *Chem. Soc. Rev.* **45**(5): 1457–1501.

Kasban, H., El-Bendary, M. and Salama, D. (2015). A comparative study of medical imaging techniques, *Int. J. Inf. Sci. Intell. Syst.* **4**(2): 37–58.

Kobayashi, H., Watanabe, R. and Choyke, P. L. (2014). Improving conventional enhanced permeability and retention (epr) effects; what is the appropriate target?, *Theranostics* **4**(1): 81.

Kwon, E. J., Lo, J. H. and Bhatia, S. N. (2015). Smart nanosystems: Bio-inspired technologies that interact with the host environment, *Proc. Nat. Acad. Sci.* **112**(47): 14460–14466.

Li, D., Ding, J., Zhuang, X., Chen, L. and Chen, X. (2016). Drug binding rate regulates the properties of polysaccharide prodrugs, *Journal of Materials Chemistry B* **4**(30): 5167–5177.

Li, J. et al. (2017). Micro/nanorobots for biomedicine: Delivery, surgery, sensing, and detoxification, *Science Robotics* .

Luo, M., Feng, Y., Wang, T. and Guan, J. (2018). Micro-/nanorobots at work in active drug delivery, *Advanced Functional Materials* **28**(25): 1706100.

Maeda, H., Nakamura, H. and Fang, J. (2013). The epr effect for macromolecular drug delivery to solid tumors: Improvement of tumor uptake, lowering of systemic toxicity, and distinct tumor imaging in vivo, *Advanced Drug Delivery Reviews* **65**(1): 71–79.

Maltzahn, G. V. et al. (2011). Nanoparticles that communicate in vivo to amplify tumour targeting, *Nat. Mater.* **10**(7): 545–552.

Nico, B. et al. (2008). Evaluation of microvascular density in tumors, pro and contra, *Histology and Histopathology* .

Pages-Zamora, A., Vidal, J. and Brooks, D. H. (2002). Closed-form solution for positioning based on angle of arrival measurements, *The 13th IEEE international symposium on personal, indoor and mobile radio communications*, Vol. 4, IEEE, pp. 1522–1526.

Park, J.-H., von Maltzahn, G., Ong, L. L., Centrone, A., Hatton, T. A., Ruoslahti, E., Bhatia, S. N. and Sailor, M. J. (2010). Cooperative nanoparticles for tumor detection and photothermally triggered drug delivery, *Advanced Materials* **22**(8): 880–885.

Raju, L. K., Ibrahim, F. and Muralikrishna, P. (2016). Distributed target localization and tracking using distributed bearing sensors, *Procedia Computer Science* **93**: 728–734.

Ruder, S. (2016). An overview of gradient descent optimization algorithms, *ArXiv Preprint ArXiv:1609.04747* .

Saunders, R. et al. (2006). Simulation of mammographic lesions, *Academic Radiology* **13**(7): 860–870.

Seidi, K. et al. (Apr. 2018). Tumor target amplification: Implications for nano drug delivery systems, *J. Con. Rel.* **275**: 142–161.

Servant, A., Qiu, F., Mazza, M., Kostarelos, K. and Nelson, B. J. (2015). Controlled in vivo swimming of a swarm of bacteria-like microrobotic flagella, *Advanced Materials* **27**(19): 2981–2988.

Shi, S., Chen, Y. and Yao, X. (2020). In vivo computing strategies for tumor sensitization and targeting, *IEEE Transactions on Cybernetics* .

Sutherland, R. M. (1988). Cell and environment interactions in tumor microregions: the multicell spheroid model, *Science* **240**(4849): 177–184.

Turner, H. E. et al. (2000). Angiogenesis in pituitary adenomas and the normal pituitary gland, *The Journal of Clinical Endocrinology & Metabolism* **85**(3): 1159–1162.

Upputuri, P. K. et al. (2015). Recent developments in vascular imaging techniques in tissue engineering and regenerative medicine, *BioMed Research International* **2015**.

van, G. T. et al. (2020). Engineering intelligent nanosystems for enhanced medical imaging, *Adv. Int. Sys.* **2**(10): 2000087.

Wilhelm, S. et al. (2016). Analysis of nanoparticle delivery to tumours, *Nat. Rev. Mater.* **1**(5): 16014.

Wong, J., Chilkoti, A. and Moy, V. T. (1999). Direct force measurements of the streptavidin–biotin interaction, *Biomolecular Engineering* **16**(1-4): 45–55.

Zhou, Z., Qutaish, M., Han, Z., Schur, R. M., Liu, Y., Wilson, D. L. and Lu, Z.-R. (2015). Mri detection of breast cancer micrometastases with a fibronectin-targeting contrast agent, *Nature Communications* **6**(1): 1–11.

Chapter 4

Autonomous *In vivo* Computation in Internet-of-Nano-Bio-Things

Different natural biological processes are possible because of the collaboration among simple living cells. Similarly computerized systems such as multi-agent systems (MAS) rely on multiple interacting agents with simplified and reduced capability, to collectively solve difficult problems that are impossible for individual agents to solve on their own. This work highlights an autonomous tumor sensitization strategy in complex human vasculature, where target detection is achieved through swarm coordination mechanism, with no prior knowledge of tumor location. We propose that small-scale biocompatible organisms such as nanoparticles, can perform deterministic tasks following the simple principles of aggregation and migration. We aim to show through computational experiments that tumor-triggered bio-physical gradients can be leveraged by nanoparticles to collectively move towards the potential tumor hypoxic regions. Although individual nanoparticles have no target-directed locomotion ability due to limited communication

and computation capability, we demonstrate that once passive collaboration is achieved, they can successfully avoid obstacles and detect the tumor. Numerical experiments demonstrate that the overall targeting efficiency could improve considerably from 10% to 90% through passive collaboration among nanoparticles. Furthermore, with the introduction of noisy search space and mobile obstacles, the targeting performance would reduce by 25%. Such self-regulating particles can be used as homing agents for target amplification, and hence can assist in early cancer detection through contrast-enhanced medical imaging. We believe that our work will motivate self-dependent and non-centralized approach for magnification of tumor location.

4.1 Introduction

Cancer is one of the leading cause of human deaths for the past few decades (Siegel et al.; 2017). The number of fatalities can be significantly reduced if the tumors are detected at their early stage. This is challenging through existing medical imaging technologies due to their resolution limits. As an emerging nanotechnology, computational nanobiosensing has great potential in the field of biomedicine (Seidi et al.; 2018; Shi et al.; 2019). With the rapid development of mart nanosystems, present diagnostic and therapeutic strategies can be vastly revolutionized. As an example, nanoparticles with inherit biosensing ability along with chemical or physical tumor-induced sensitivity, may perform autonomous detection of small tumors in hard-to-reach tissues and human body cavities.

4.1.1 Background

4.1.1.1 Early Cancer Detection

Cancer grows exponentially, therefore detecting cancer in its early stage is the most important factor for successful treatment of this life threatening disease, especially for prostate and penile cancer in men and for cervical and breast cancer in women. Modern era medical imaging techniques (MITs) such as MRI, computed tomography and X-rays have insufficient resolutions for detecting very small malignant tumors having no clinically evident symptoms (Kasban et al.; 2015). For example, small high risk breast cancer (< 2 mm) and micro-metastasis are undetectable due to limited potential of present clinical imaging modalities (Zhou et al.; 2015). These malignant tumor cells can metastasize to bones, liver, lungs, and brain. In an effort to detect small tumors before they start metastasizing, researchers are turning to nanoparticles or liposomes (Qian et al.; 2012; Ferrari; 2005; Malekzad et al.; 2017) as candidates for contrast agent in MITs (Bucci et al.; 2017; Wen et al.; 2016). Contrast agents such as CREKA-Tris $(GD\text{-}DOTA)_3$, have been used in getting robust contrast enhancement by enabling the detection of small metastatic tumors (< 0.5 mm), extending the detection limit of imaging modalities (Zhou et al.; 2015). Healthy and tumoral tissues can have more prominent distinguishing features, once these contrast enhancing nanoparticles deposit themselves on malignant tumors, making early cancer detection practicable with the help of existing medical imaging techniques.

4.1.1.2 Tumor Homing through Systemic Circulation

Chemotherapy is regarded as one of the most effective treatments of cancer and is widely used around the globe. However, it is associated with systemic toxicity that ultimately harms healthy tissues as well as malignant tumors. Cells in the bone marrow for blood forming, hair follicles, and cells in the digestive tract and reproductive system are most likely to be damaged by chemotherapy. To control this side effect, targeted drug carriers have been proposed in the recent few decades (Mimeault et al.; 2008). Nevertheless, with knowledge-less systemic targeting, a very small percentage of nanoparticles are delivered to the cancerous site. Due to the influence of systemic circulation, ample driving force is not available to target the hypoxic regions. Moreover, nanoparticles are consumed and lost inside the human vasculature due to spreading (diffusion), deterioration and branching (taking a wrong vessel), etc. It is because of these reasons that systemic targeting only delivers a small fraction ($< 2\%$) of nanoparticles to the precise tumor location (Bae and Park; 2011; Wilhelm et al.; 2016).

4.1.1.3 Tumor Homing through External Manipulation

Recent work has increased the detection probability and targeting efficiency of nanoparticles with the aid of external tracking and control (Chen, Ali, Shi and Cheang; 2019). The main advantage of tumor sensitization through external manipulation is that the nanoparticles take the shortest path to reach diseased tissues ensuring their minimum exposure to the systemic circulation. However, *a priori* knowledge of the tumor location is required in order to guide nanoparticles towards the tumor. It has been shown that through the aid of external magnetic field, 55%

of the drug containing nanoliposomes harnessed by the magneto-aerotactic bacteria called Magneto-coccus marinus strain (MC-1) reached the tumor hypoxic regions (Felfoul et al.; 2016). Alternatively, tumor detection can also be achieved with no prior knowledge of the tumor location through smart nanosystems. These systems can be broadly classified into "environment-responsive system" and the "environment-primed systems"(Seidi et al.; 2018; Kwon et al.; 2015; Von Maltzahn et al.; 2011; Park et al.; 2010). They are designed in a way so that the *in vivo* environment itself assists in early microcarcinoma detection. However, in the absence of information related to tumor location, the detection process does not guarantee fast detection of cancer, as it may not always adopt the shortest path. Externally manipulable smart nanosystems are proposed by Chen et al. (Chen, Ali, Shi and Chaeng; 2019), that profits from the benefits of smart nanosystems along with external control and tracking, resulting in an increase of tumor detection capability. It is worth mentioning here that nanoparticles are being treated individually or as a single entity in all of the detection procedures mentioned above. There is no communication or cooperative behaviour among nanoparticles that may help them to move towards malignant tumors. In the case of external manipulation, there is a macro unit for control and tracking which is used to guide the nanoparticles towards the possible tumor location.

4.1.2 Self-Regulated and Coordinated Tumor Targeting

4.1.2.1 Tumor-triggered Gradient Responsiveness

Passive physical properties of the host environment are changed in the presence of a tumor. These include alterations in blood velocity and oxygen content (Baish

et al.; 1996; Komar et al.; 2009), variations in temperature and reshaping of vasculature architecture (Gazit et al.; 1995) in the peritumoral region. Moreover, chemical properties such as the redox potential and pH profile are also changed in the tumoral environment. The rapid proliferation of cancerous cells results in an inadequate supply of blood, causing a reduced supply of oxygen and other nutrients. As a result, lactic acid is produced in cancerous cells, contributing to a lower pH in tumors than normal tissue (pH = 7.4). Finally, biological properties such as the bio-molecular cell structure and enzymes are also changed in the peritumoral region. These biochemophysical gradients are regarded as internal stimuli while external stimuli such as light, ultrasound or magnetic fields can also be used to induce tumor-specific triggers that can prime the host environment with bio-physical gradients (Shen et al.; 2015; Kelley et al.; 2013).

Such a change in conditions in the tumoral environment stimulate nanoparticles to undergo morphological and structural changes. For example, the hyperthermic nature of most tumor sites can act as an internal stimulus for temperature-sensitive polymers such as PNIPAAm and its derivatives. Their structure is switched from a swollen form to a shrunken form and vice versa in response to a change in temperature around upper and lower bounds of critical values called the upper critical solution temperature (UCST) and the lower critical solution temperature (LCST); thereby, a phase transition leading to swelling or shrinking occurs (Yan and Okuzaki; 2008; Beija et al.; 2011; Karimi et al.; 2016). Similarly, "brush hydrogels", consisting of NiPAAm and arcylic acid (AAc) co-polymers also possess the temperature-dependent capability of shrinkage/swelling of the brushes (Lue et al.; 2011). Moreover, temperature-sensitive liposomes are another potential nanoparticles with limited toxicity that exhibit a phase transition after a change

in temperature. In the past few years, there have been abundant advances in finding pH-responsive nanoparticles which have extremely low cytotoxicity towards healthy cells (Song et al.; 2014). For example, self-assembled micelles (Li et al.; 2016), which are stable at the physiological pH of 7.4, undergo swelling in acidic intratumoral (pH = 6.8) and endosomal (pH = 5.5) environments. These phase transition behaviours, which can also be seen in several biological growth processes (s Vicsek; 1992), help to achieve clustering and transportation of nanoparticles by aligning the directions of their motion after collaborating with neighbours (Li et al.; 2019; Vicsek et al.; 1995). As a result, they start to have a self-regulated movement towards the desired target.

4.1.2.2 Autonomous Tumor Sensitization

Nanoparticles have been mainly considered as individual entities in the previous research that require a central macro unit to externally guide them (Cheang et al.; 2017; Ali et al.; 2019). The nanoparticles' behaviour is observed externally which helps in selecting the best direction of magnetic field that is used to steer nanoparticles to the possible tumor location. Similarly, an external control unit is required to explicitly manipulate individual components in most of the current robotic systems designed for target homing or object transportation. By contrast, Li et al. (Li et al.; 2019) has designed loosely coupled particles that can collectively move towards a light source (photo-taxis). These particles can only perform uniform oscillations with no independent locomotive ability. By mutual collaboration and coordination, they attain the capability to perform robust locomotive features such as avoiding obstacle and transporting load without taking help from any external source.

An alternative approach proposed in the current research work, inspired by the natural biological systems such as wound healing (Friedl and Gilmour; 2009; Weijer; 2009), morphogenesis or the growth of cancer itself, is the independent and fully autonomous system in which very simple nanoparticles with minimum computation ability, when combined together, can perform tumor homing and obstacle avoidance in complex human vasculature (Ali, Sharifi, McGrath, Cree and Chen; 2020). The swarm of such biological gradient field (BGF) sensing nanoparticles successfully detects the target through the principles of cooperation and coordination. These nanoparticles collectively achieve target-directed locomotion through internal structural changes, caused by the *in vivo* physical, chemical or biological alterations in the peritumoral region (Park et al.; 2017). Similar collective and collaborative phenomena can also be observed during flocking, shoaling, and swarming behaviours of birds, fish, and insects, respectively. One such system is shown in Fig. 4.1(a), where injected nanoparticles (in black), under the influence of biophysical gradient field (in red shading) around the early microcarcinoma, collaborate with their neighbours and move towards the possible target location. The number of neighbours that each nanoparticle can interact with, depends upon its physical characteristics like shape, size, coating or material and must be designed in order to maximize efficacy. Future micro- or even nano-scale medical applications in which the prime focus is to scale up the number of components while reducing the size of each component has a huge potential for such a system.

In the current work, tumor sensitization is performed through autonomous and independent nanoparticles which form the basis of the proposed self-regulating *in vivo* computation framework. Previous research either focused entirely on sys-

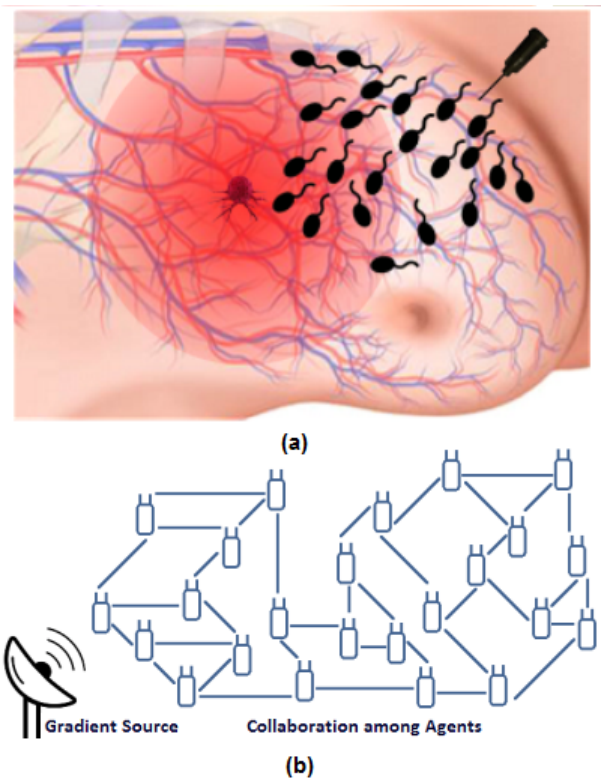

Figure 4.1: (a) Bio-inspired tumor sensitization. Nanoparticles (in black) passively collaborate and move towards potential tumor after sensing gradient (red circle). (b) Illustration of collaboration among agents to move collectively towards a gradient source in a typical Multi-agent system.

temic circulation during the tumor homing process (Bae and Park; 2011; Wilhelm et al.; 2016) or used an external controlling unit to guide nanoparticles towards the possible tumor location (Chen, Ali, Shi and Cheang; 2019; Felfoul et al.; 2016; Cheang et al.; 2017; Ali et al.; 2019). In contrast, the current work is inspired by multi-agent systems (MAS) in which swarm intelligence of autonomous agents helps to solve complex computer science and engineering tasks. One such problem may be target detection in complex search domains where agents using multiple aiding inputs such as environment sensing, collaboration among neighbouring

agents and/or their own history of actions, try to find the possible target location as shown in Fig. 4.1(b).

Working along the same lines, we propose that the BGF-triggered response of the nanoparticles along with collaboration among neighbours can help in collectively deciding about the next course of movement leading to target-directed locomotion. Note that isolated nanoparticles can only go through gradient dependent morphological changes and do not possess any ability to move towards the target. It is only in a collective action, that a targeting behaviour arises. The simple design and working principle of our proposed tumor homing strategy makes it a very promising approach for applications like contrast-enhanced medical imaging or targeted drug delivery. Due to the nature of human vasculature, the prime objective is to go small scale in size which makes it very demanding to achieve individual addressability (Zhang et al.; 2012; Sitti; 2009; Hu et al.; 2018). Moreover, the framework is robust due to the locomotion depending upon collaboration among all the particles rather than on any internal or external individual entity. Hence, it remains operable even if some nanoparticles are lost in the host environment due to degeneration, branching or finite life span of nanoparticles. Finally, due to the absence of any fixed design or pre-specified orientation, the swarm of nanoparticles is highly flexible which can maneuver itself to avoid any obstacle that comes in its way during target homing. Nevertheless, this system always requires a BGF to work in an acceptable manner as demonstrated in Section 4.4.

4.1.3 Main Contributions of the Current Chapter

This work is an extension of our previous research (Ali, McGrath, Shi, Cree, Cheang and Chen; 2020) and provides a detailed explanation of computational experiments for autonomous *in vivo* computation. First of all, a novel analogy of the natural computing problem is established with the multi-agent system (MAS). A one-to-one mapping is presented between tumor sensitization through natural computation and autonomous MAS which was not presented in (Ali, McGrath, Shi, Cree, Cheang and Chen; 2020). Secondly, in the current work, reality checks of natural computing that may affect the system efficacy are outlined, providing a critical insight about the limitations of the natural computation problem. These important aspects on the real-life constraints are missing in our previous work. (Ali, McGrath, Shi, Cree, Cheang and Chen; 2020) focuses only on the ideal case of a noise-less search domain, whereas the current work considers imperfections poised by natural biological environments through a noisy search domain. A range of standard deviations of the noise have been chosen to demonstrate its effect on the targeting efficiency. Furthermore, our previous work considers the simplified scenario of static obstacles. However, there are always some mobile obstacles in the blood circulatory system in the form of red blood cells, white blood cells, platelets, and plasma. These constituents of blood will have effects on the target-directed locomotion of nanoparticles. To emulate these and test the robustness of the algorithm, we have introduced mobile obstacles in our current work. Finally, we have included a new objective function following a bell-shaped Gaussian curve for our simulation experiments.

4.1.4 Organization of the Chapter

The chapter is organized as follows. Section 4.2 first mentions the general characteristics of MAS, followed by mapping of MAS to the natural tumor homing process and the associated challenges. In Section 4.3, we discuss the measurable objective functions for the systemic targeting of tumoral tissues mapped on to *in vivo* biophysical gradients along with different search domains representing tumoral environments. Moreover, general steps of the target amplification framework are also introduced in this section. Section 4.4 give details of the proposed bio-inspired self-regulated *in vivo* computation framework. Section 4.5 describes the simulation parameters followed by the performance analysis of different design parameters to demonstrate the effectiveness and robustness of our proposed framework. Finally, Section 4.6 draws some concluding remarks along with future possible directions.

4.2 MAS Inspired Biosensing

4.2.1 Characteristics of MAS

Multi-agent systems have recently gained enormous popularity among researchers because of their capability to solve complex problems (Dorri et al.; 2018; Shamshirband et al.; 2013). Difficult tasks are divided into simpler sub-tasks for independent and autonomous identities called agents. These agents after sensing the environment and using historical data in some cases, collaborate amongst neighbouring agents to solve their individual tasks. MAS are efficient because a harder problem is divided into simpler tasks for each individual agent making it relatively easy to accomplish. With the simplified task allocated to each agent contributing to a

rather uncomplicated framework with low communication overhead, MAS ensure easy scalability due to limited exchange of information. They are highly flexible because of their inherent potential to learn and make decisions independently. The primary goal of each agent is to gain knowledge of the environment and its neighbours which is achieved by having the following features:

- *Sociability:* In order to solve complex tasks, agents share information with their neighbours. This information can be knowledge of the environment, of their present state and/or of their history of actions.

- *Autonomy:* All agents are completely independent and hence decide about their future actions by themselves. There is no external interference in the critical process of decision making.

- *Proactivity:* Every agent takes a decision after sensing the environment and using the historical data along with knowledge of collaborating neighbours. All individual actions taken by agents results in achieving the ultimate and collective goal. Hence it is the proactiveness of the agents in solving their simpler tasks that helps in resolving the complex problems.

4.2.2 Mapping from MAS to Natural Computing

Natural computing refers to the novel problem-solving techniques inspired from information exchange in nature (Rozenberg et al.; 2012). Natural processes like biological transport, protein-protein interactions, development processes and self-assembly undergo information processing. As a result, natural computing methods employ natural materials such as molecules or micro/nano biological particles for

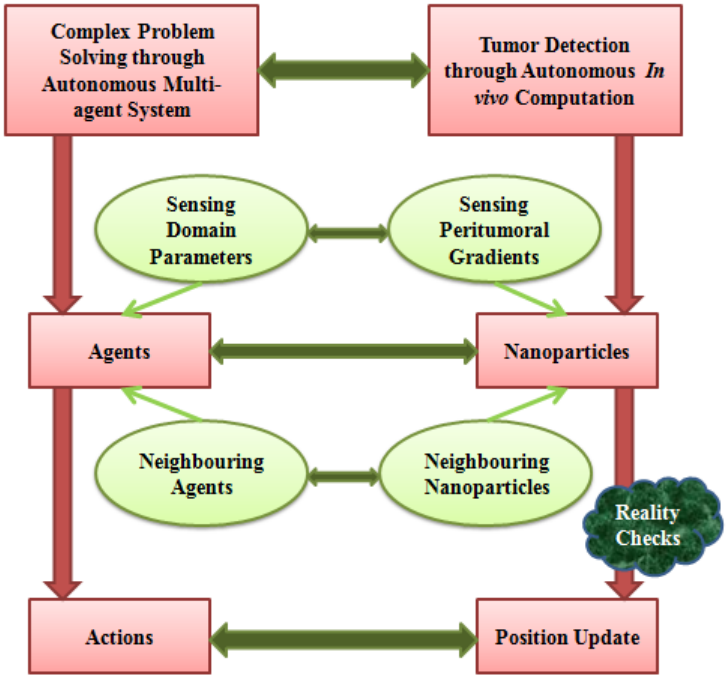

Figure 4.2: Mapping (shown with double headed green arrows) of autonomous MAS to tumor sensitization through autonomous natural computation with reality checks explained in Section 4.4.2.

computation purpose. Swarm intelligence, which is inspired by the behaviour of a group of natural organisms may vice versa provide useful insight into the natural computing procedures. Notably, the collective and social behaviour forming the fundamental working principle of MAS and their salient features mentioned in Section 4.2.1, make them a potential candidate to be researched for natural computing problems like tumor detection which is associated with a complex and uncertain biological environment at a very small scale. MAS do not require any external manipulation or intervention to achieve the common goal and entirely rely on self and autonomous actions. There exists a fascinating analogy between MAS and the tumor homing process which is highlighted below.

1. *Agents:* Agents which are the building blocks of any MAS, correspond to nanoparticles in natural computing as shown in Fig. 4.2. As agents sense their environment to solve their individual sub-tasks, nanoparticles are also capable of sensing the tumoral environment and go through certain morphological changes. Such an alteration in their physical, chemical or biological properties along with their socializing ability (for example, push-and-pull effect due to change in size of an individual nanoparticle) helps them to collaborate with their neighbouring nanoparticles to take decisive actions. Unlike MAS, where agents actively share the sensed information, nanoparticles in natural computing process only go through uniform structural oscillations resulting in passive exchange of information.

2. *Domain:* Domain or environment of the agents in MAS is similar to the biological search space for nanoparticles to look for potential tumoral tissues. A MAS environment may or may not be deterministic but for natural computing process, it is always non-deterministic as the outcome of an action is not entirely predictable because of random *in vivo* conditions such as finite life span of nanoparticles and discretized nature of vascular networks. Furthermore, the peritumoral region is dynamic as the changes that occur in that region are caused by the tumor itself rather than as a consequence of the actions taken by nanoparticles. On the other hand, an environment in MAS can be both static or dynamic.

3. *Parameters:* Parameters are the different types of data available in the domain that are sensed by an agent and its neighbouring partners. This is similar to having different bio-physical gradients in natural computing that

originate due to the presence of tumoral tissues. After sensing the appropriate data, it is shared among the neighbours to take decisive actions. An appropriate decision is achievable through two inputs to agents in MAS, namely domain parameters and neighbouring agents, corresponding to biophysical gradients and neighbouring nanoparticles in natural computing as shown in Fig. 4.2. Apart from possessing the natural ability to sense the peritumoral region, it is very important for nanoparticles to passively exchange the sensed information with neighbouring nanoparticles through structural changes.

4. *Actions:* After sensing the domain parameters, agents perform certain tasks or actions which help them to solve their sub-tasks. Once the individual simplified task is accomplished for each agent, the ultimate complex goal of the whole system is achieved. For example, in a computer soccer game, a certain player (agent) evaluates parameters such as position of the ball, speed and position of opponent players to decide about his action. Similarly, as mentioned in Section 4.1.2, nanoparticles undergo BGF-dependent structural changes in the peritumoral region. For example, swelling and shrinking of temperature-sensitive nanopolymers, along with their proactiveness, autonomous nature and socializing ability, help their swarm to mutually collaborate and potentially move towards the desired target. Although, nanoparticles-oriented biosensing for tumor detection is similar to agents-oriented MAS, the former has several unique reality checks which are explained comprehensively in Section 4.4.2.

4.3 Autonomous Tumor Homing Framework for Target Amplification

4.3.1 Objective Functions

As the research is still in its early stage, there are no quantitative models for the tumor-induced physical (thermal), chemical (pH changes) or biological (enzyme alterations) gradients. As such, we look into some functions that have been routinely applied in standard test problems and could represent the BGFs around the tumor with different modes of fluctuation. Hence, for the purpose of initial investigation, four objective functions represented by $f(x, y)$: sphere function, Matyas function, Gaussian function, and disc function, are chosen to evaluate the performance of the proposed simulation framework. The sphere function has a smooth change in the gradient and is represented by a bowl-shaped landscape (Fig. 4.3(a)). Next, the gradient of the Matyas function is not as smooth as the sphere function but still better than the one we have in the form of a disc function; hence the Matyas function which forms a plate-shaped landscape (Fig. 4.3(c)), can be treated as an average case. The Gaussian function which follows a normal distribution forming a bell-shaped curve is shown in (Fig. 4.3(g)) with mean zero and variance σ^2. These functions should be in general agreement with the qualitative observations made in the existing literature, and thus allow for some useful insight being provided into the effectiveness of the proposed approach for tumor detection with varying levels of difficulty. For example, shear stress can be viewed as an internal mechanical stimulus that can cause change in the morphological structure of nanoparticles. It is higher in narrowed segments of arteries and microvasculature

around the tumor compared to healthy and wider arterial segments, and thus can be qualitatively represented by the sphere, Matyas or Gaussian functions. Finally, the disc function (Fig. 4.3(e)), corresponds to the worst-case search space with zero gradient everywhere except the tumor location. All the objective functions mentioned above can be defined as

1. *Sphere Function:*

$$f(x,y) = \begin{cases} 1, & \sqrt{x^2+y^2} \leq 0.5 \\ 1 - 0.02\left(x^2+y^2\right), & \sqrt{x^2+y^2} > 0.5 \end{cases} \tag{4.1}$$

2. *Matyas Function:*

$$f(x,y) = \begin{cases} 1, & \sqrt{x^2+y^2} \leq 0.5 \\ 1 - 0.01\left(x^2+y^2\right) + 0.02xy, & \sqrt{x^2+y^2} > 0.5 \end{cases} \tag{4.2}$$

3. *Gaussian Function:*

$$f(x,y) = \begin{cases} 1, & \sqrt{x^2+y^2} \leq 0.5 \\ 1/\left(2\pi\sigma^2\right) \times \exp\left[-\left(x^2+y^2\right)/\left(2\sigma^2\right)\right], & \sqrt{x^2+y^2} > 0.5 \end{cases} \tag{4.3}$$

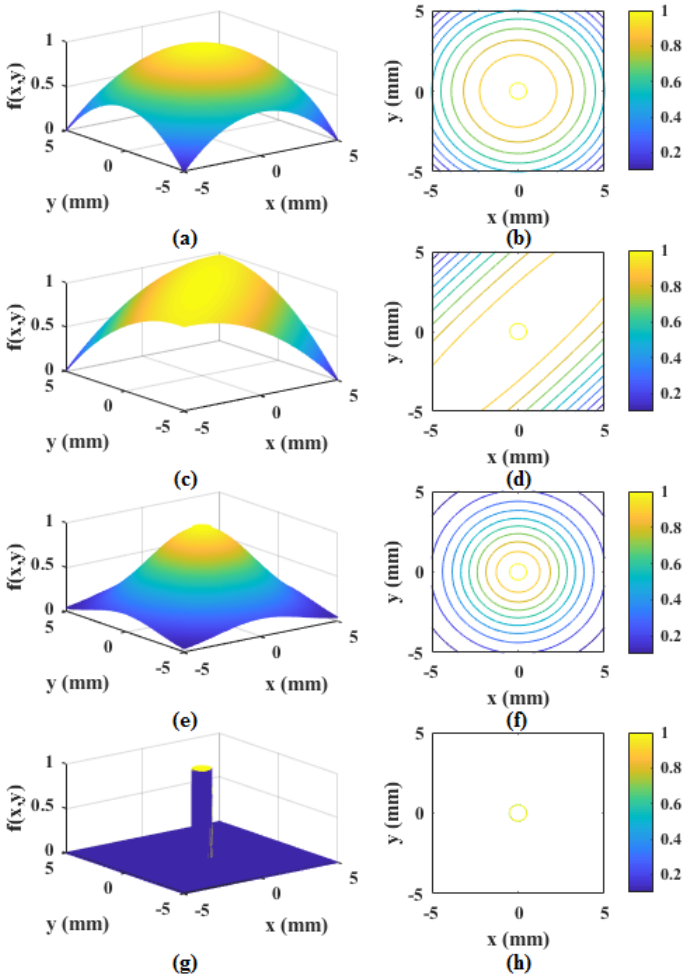

Figure 4.3: Illustration of $f(x, y)$ for three representative objective functions: Sphere function with its contour plot (a) and (b); Matyas function with its contour plot (c) and (d); Gaussian function with its contour plot (e) and (f); Disc function with its contour plot (g) and (h). For the objective function $f(x, y)$, the small yellow circle in the centre of contour plots represents the maxima.

4. *Disc Function:*

$$f(x,y) = \begin{cases} 1, & \sqrt{x^2+y^2} \leq 0.5 \\ 0, & \sqrt{x^2+y^2} > 0.5 \end{cases} \tag{4.4}$$

The search space domain is defined within -5 mm $\leq x, y \leq 5$ mm where the maximum and minimum values of the objective functions are normalized to 1 and 0 respectively. The maximum is in the centre of the domain for all four functions and is denoted by a small circle (representing tumor). As we move away from the center towards the boundaries of the representative functions, their value starts decreasing and eventually becomes 0 at the edges of the search domain. For simplicity, we have chosen 1 (for maximum) and 0 (for minimum) as the extreme values which can effectively emulate a wide variety of biological gradient field landscapes (after adequate scaling) without loss of generality. Note that the disc function is an exception, which has no gradient and abruptly goes from to 1 to 0 outside the circle with radius 0.5 mm. It synthesizes the worst-case scenario without any gradient in the landscape.

4.3.2 Proposed Computational Framework

We propose a non-centralized and independent system in which stochastic (random) movements of nanoparticles when allowed to aggregate and migrate together, result in deterministic behaviours (Li et al.; 2019). These nanoparticles have to be injected simultaneously to start collaborative movements (socializing) in the homing process. Natural phenomena such as morphogenesis, spreading of cancer or healing of a wound are a consequence of collaboration and migration achieved by living organisms. Going along the same lines, a swarm of gradient-selective nanoparticles attempts to swim in a complex vascular network and search for the potential location of the tumor. The group of nanoparticles is highly flexible and scalable due to the absence of individual identity and addressability of nanopar-

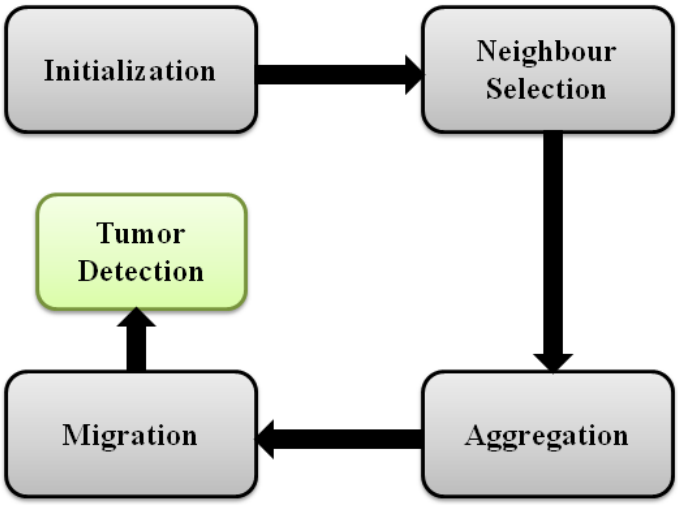

Figure 4.4: Illustration of four major steps involved in the proposed framework. After initial deployment, neighbour selection, aggregation and migration are repeated for tumor sensitization process.

ticles. The non-centralized and independent swarm can orient itself in unfamiliar environments to perform difficult tasks such as object transport (drug delivery) and obstacle avoidance (bypassing wrong vessel). Moreover, these non-centralized nanoparticles are self-evolving in terms of their collective locomotion because of their inherited proactive and autonomous nature, and hence do not require any monitoring unit. Although randomness of this approach prevents its employment in applications where complex pre-specified geometry is vital, its potential is huge in nanomedicines where the prime objective is to maximize the number of components while minimizing the size of each component.

For simplicity, it is assumed that the centre of the tumor introduces an *in vivo* bio-physical isotropic gradient that is sensed by all nanoparticles. The steps involved in the proposed framework are shown in the Fig. 4.4 and explained as follows:

1. *Deployment:* The N nanoparticles are randomly deployed in a pre-defined and confined injection site simultaneously, prior to the start of actual tumor homing in the simulation framework. Under the influence of BGF from a source (tumor), these nanoparticles experience a change in their physical properties such as size. It is important to mention here that the case of one global optimum (centre of tumor) is considered here, which is represented by $f(x, y)^*$ in the domain $\mathbb{D}$.

2. *Neighbour Selection:* After deployment, K neighbours of a nanoparticle are chosen from the swarm of N nanoparticles based on the minimum distance criterion. Hence, the closest K nanoparticles become the neighbours of a particular nanoparticle. In MAS, agents "actively" share their knowledge or request information from other agents to improve their performance in meeting their goals. On the same lines, selecting neighbours in natural *in vivo* computation is critical to help nanoparticles "passively" share the sensed BGF response (structural changes) among them. The simulation framework is flexible and allows for selecting different numbers of neighbours which affect the computational capacity as well as the targeting efficiency (number of nanoparticles successfully detecting the target from the overall deployed swarm) of the homing process. The algorithm demonstrates that more neighbours require large computational power but can also achieve higher targeting efficiency of the homing process.

3. *Aggregation:* Once the neighbours are selected for a certain nanoparticle, the next step is to determine their effect on it. This step is all about collaboration among nanoparticles and can be further divided into two opera-

tions namely "sensing" and "sharing" as can be seen in the mapping demonstrated in Fig. 4.2. A particular nanoparticle is pushed or pulled by its neighbour, depending on whether its neighbour has experienced higher or lower gradients respectively. This pushing/pulling effect can be envisaged because of the difference in sensed BGF by nanoparticles (such as thermal responsive nanopolymers explained in Section 4.1.2) in the peritumoral region. The BGF-dependent pushing and pulling among nanoparticles is actuated by maintaining a favorable distance which is not too large that structural changes do not have any effect on neighbouring nanoparticles and not too small that the interaction cannot be translated into target-oriented locomotion. After calculating the magnitude of the interaction caused by the difference in sensed gradients, the direction of the displacement is calculated which is simply a ratio between the position of a nanoparticle and its neighbour. The process is repeated for all K selected neighbours to determine the resultant displacement direction.

4. *Migration:* The final step in our proposed tumor sensitization strategy is to update the position of the nanoparticle based on the resultant magnitude and direction of the cooperative effect calculated in the previous step. Another important factor that helps in determining the location of the next position is the step size γ that works out the magnitude of displacement of a nanoparticle under the aggregated influence of its neighbours. Nanoparticle behaviours such as its ability to move (step size) and interaction with the environment depends upon its composition features like initial size, material, shape, charge or combination of them (Hauert and Bhatia; 2014).

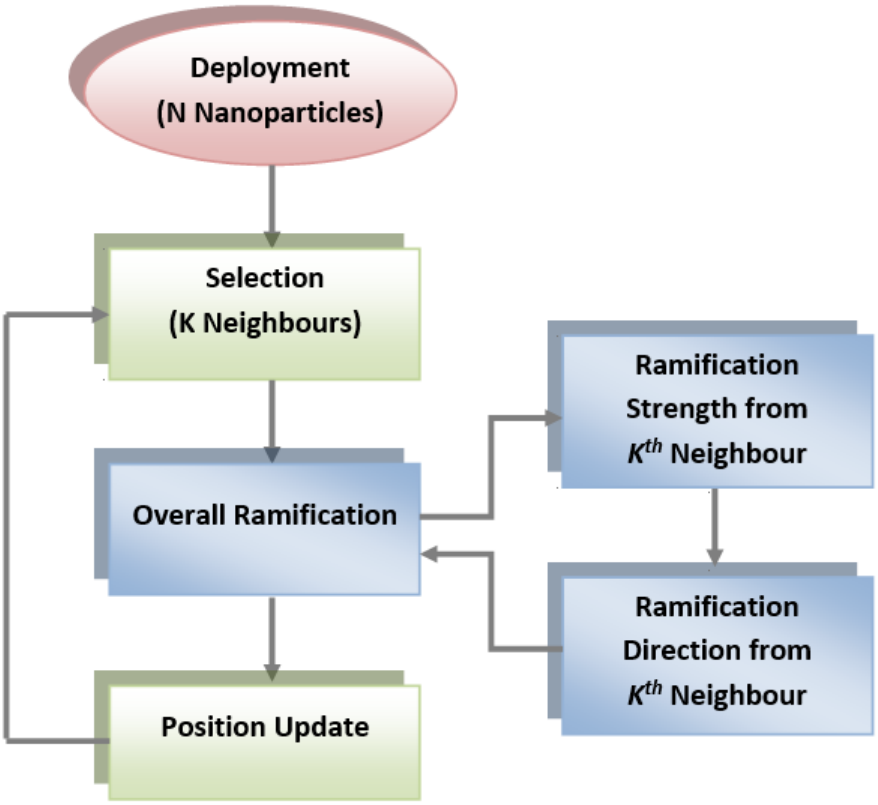

Figure 4.5: Flowchart representing an autonomous computation framework in which N *nanoparticles are deployed to search for the tumor. Loop in blue shows the combined effect of interactions among the* K *selected nanoparticles, helping to determine the next location of nanoparticles.*

4.4 Autonomous Targeting Strategy For Tumor Sensitization

4.4.1 Algorithm for Natural In vivo Computation

In the proposed framework, we start with N nanoparticles of which the j^{th} nanoparticle is deployed at point $\vec{x}_j$ in an injection site which is a localised region in the simulation domain $\mathbb{D}$. After successful deployment, K closest neighbours

are selected as shown in Fig. 4.5. All injected nanoparticles experience the BGF as $\zeta_1, \zeta_2, \zeta_3, \ldots, \zeta_{\mathrm{N}}$ in the domain $\mathbb{D}$ where $\zeta_1 = f(\vec{x}_1), \zeta_2 = f(\vec{x}_2), \zeta_3 = f(\vec{x}_3), \ldots, \zeta_{\mathrm{N}} = f(\vec{x}_N)$. The sensed gradient ζ is inversely proportional to the distance between a nanoparticle and its target. As every nanoparticle and its collaborating neighbours have unique positions in the search domain, they possess a non-identical value of ζ, BGF-dependent structural changes such as change in size are different for all of them. The difference in the sensed BGF values is

$$\Delta\zeta = \zeta_{\mathrm{p}} - \zeta_{\mathrm{n}} \tag{4.5}$$

where ζ_{p} and ζ_{n} are the gradients sensed by a nanoparticle and its neighbour respectively. Eq. (4.5) describes the case of a noiseless search space, however natural environment is always associated with distortions due to non-idealities such as learning errors of nanoparticles and the propagation delays in mechanical wave communications as explained in Section 4.3.2. Learning errors incurred during gradient sensing can be internal (due to physical properties of nanoparticles) or external (caused by the ever-changing characteristics of biological search space) around the tumor. Similarly, long delays in translating BGF-induced morphological changes into target-oriented motions will cause the neighbours of each nanoparticle to induce inter-reaction interference. These phenomena can be viewed as causing noisy communications among the swarm as they both modify the collaborative effect in a disruptive manner. To counter these non-idealities, a normally distributed random noise is added in Eq. (4.5), such that

$$\zeta_{\mathrm{D}} = \Delta\zeta + \chi(\mu, \sigma) \tag{4.6}$$

where ζ_{D} represents the distorted difference in the sensed BGF values and χ is the noise with zero mean ($\mu = 0$) and a standard deviation of $\sigma_{\Delta\zeta}$ for simplicity. Another important parameter during gradient information sharing is the distance between a nanoparticle and its collaborating neighbour. If it is too large, gradient-dependent morphological changes in nanoparticles will not be able to induce pushing or pulling, and hence will not be translated into an overall swarm movement towards the target. On the other hand, closely packed nanoparticles will also make it time consuming for structural variations to be transformed into collective locomotion. Each neighbour of a nanoparticle will push or pull it due to the difference in the sensed BGF values as

$$M = \begin{cases} \frac{\Delta\zeta}{[\Delta d/d_{\mathrm{ref}}]^l} \angle [\phi], & \text{for selected nanoparticle and its } K \text{ neighbours.} \\ 0, & \text{for other swarm nanoparticles.} \end{cases} \tag{4.7}$$

where M shows the effect of interaction experienced by a nanoparticle because of its neighbour as shown in Fig. 4.6. $\Delta\zeta$ is the difference in the BGF values sensed by the nanoparticle and its neighbour, Δd is the Euclidean distance between the nanoparticle and its neighbour, d_{ref} is a normalization factor, ϕ is the direction of the effective passive collaboration and l is the path loss exponent. For simplicity, noiseless BGF difference is represented in this section; however, for simulation experiments, both noisy and noiseless cases have been considered. Let $\vec{x}_p$ and $\vec{x}_n$ be the locations of the nanoparticle and its neighbour, then the displacement between i^{th} neighbour and nanoparticle pair is given by

$$\vec{X}_{off}^{(i)} = \vec{x}_p - \vec{x}_n^{(i)}, \tag{4.8}$$

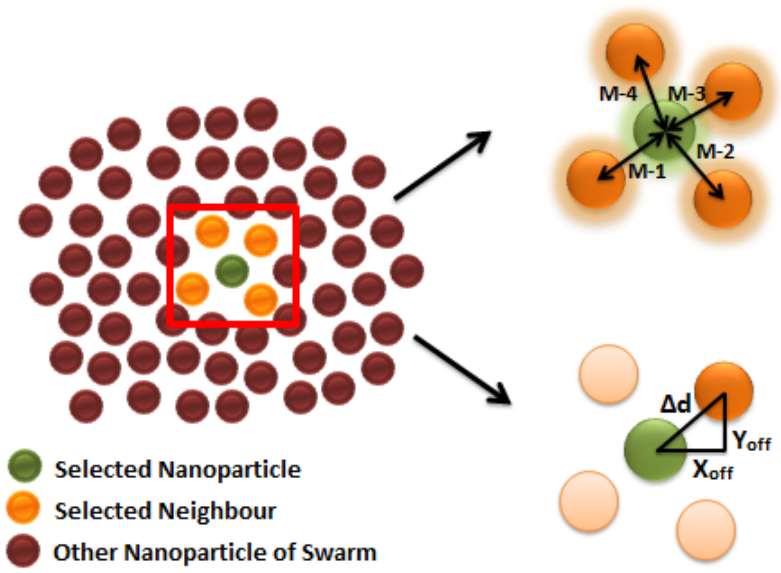

Figure 4.6: Illustration of sensed gradient sharing among nanoparticle and critical distances used for simulations.

and

$$\hat{\vec{X}}_{off}^{(i)} = \frac{\vec{X}_{off}^{(i)}}{|\vec{X}_{off}^{(i)}|}, \tag{4.9}$$

where

$$|\vec{X}_{off}^{(i)}| = \sqrt{\{X_{\text{off}}^{(i)}\}^2 + \{Y_{\text{off}}^{(i)}\}^2}\,. \tag{4.10}$$

Eqs. (4.5), (4.7) and (4.8) demonstrate the socializing behaviour of a single nanoparticle-neighbour pair. This passive collaboration is repeated for all K selected neighbours which is represented by a loop in Fig. 4.5 (in blue). The number of neighbours selected to collaborate with a single nanoparticle strikes a balance between the performance and the computation capacity. The accuracy of the step taken by a nanoparticle as a result of collaboration from a large number of neighbours is higher thereby increasing the targeting efficiency; however, it also in-

troduces a higher propagation delay due to the mechanical wave communications among nanoparticles. The overall magnitude of the interactions with resultant direction is calculated as

$$\vec{A} = \sum_{i=1}^{K} \frac{\Delta\zeta^{(i)}}{[\Delta d^{(i)}/d_{\text{ref}}]^{l}} \vec{\hat{X}}_{off}^{(i)}\,, \tag{4.11}$$

where $\vec{A}$ represents a net directed effect of interactions due to K selected neighbours. During the aggregation process, the difference between the BGF values is computed for each nanoparticle-neighbour pair and is also dependent on the distance between them. A higher number of neighbours will increase the number of parallel computations required to calculate the net effect of interactions experienced by a single nanoparticle as shown in Eq. 11. During natural computation, the above operations are realized through simultaneous biological-gradient-induced morphological changes. Hence, from the design prospective, to achieve parallel computation, a higher number of neighbours will require a more complex design to induce the net effect from all the neighbours. For example, the nanoparticle surface area should be larger so that the push or pull caused by the morphological change of the neighbouring nanoparticles in the swarm can be translated into target-directed locomotions.

After sensing the environment and sharing the tumor induced BGF values among neighbours, the next step is to take a decisive step (migration) towards the global optimum. The location of nanoparticle is updated according to

$$\vec{P}_{n+1} = \vec{P}_{n} + \gamma\vec{\hat{A}}\,, \tag{4.12}$$

where $\vec{P}_n$ is the previous position and $\vec{P}_{n+1}$ is the current position of the nanoparticle. Step size γ is an important factor that helps in determining the location of the next position. Smaller γ will introduce large propagation delays and degeneration of nanoparticles due to their finite life span whereas larger γ may cause target overshooting. Note that γ is a design parameter determined by the basic composition properties of nanoparticles such as their material, shape, initial size or a combination thereof. However, in the natural environment, identical nanoparticles will behave in a faintly unique manner as they will experience different environmental features such as blood velocity, vessel diameter or fluid pressure. Hence, γ is considered as an averaged value of the step size corresponding to non-identical responses of nanoparticles in the natural environment. Therefore, the resultant direction of the nanoparticle, which is a consequence of neighbour collaboration, is used for location update, where γ governs the magnitude of migration step towards the possible target as shown in Eq. (4.12).

4.4.2 Reality Checks for Natural Computing

Operational challenges such as task allocation, controllability and localization that are resolved by generic MAS are handled equally well by natural autonomous computation. The simple working principle of "natural" agents like temperature-dependent structural changes of nanopolymers eliminates communication overhead associated with task allocation. For example, sensed gradient-related information sharing and nanoparticle reaction are naturally integrated through mechanical wave communications. Controllability is required when MAS have to be steered from one state to another (Liu et al.; 2014). In natural computation, nanoparticles

are independent and self-regulate their motions to move towards a global target, thanks to their proactiveness and autonomous nature. Finally, localization which refers to locating an agent in MAS is not a challenge any more as autonomous natural computation is self-evolving and there is no need to locate them as natural agents aggregate in the tumoral area through the receptor-ligand binding process. Nevertheless, nanoparticles-assisted autonomous biosensing is a special category of "natural" MAS which poses its own unique reality checks as mentioned below.

4.4.2.1 Connectivity among Agents

In natural computation, collaboration among neighbours is very vital. All "natural" agents must maintain connection among them to ensure collective locomotion while interacting with the biological search space. As there is no centralized controlling unit available like MAS, agents have to always maintain a certain acceptable distance among themselves so that their morphological changes have an pushing-pulling effect on neighbours resulting in an overall swarm motion towards the target. If the distance among nanoparticles is too large, their gradient-dependent morphological changes such as change in their size will not have any effect on the neighbours. On the the other hand, if the distance is too small, it will result in a packed rigid formation of the swarm posing difficulty in target-directed locomotion.

4.4.2.2 Fault Detection and Isolation

It is highly likely that in natural environments that are associated with many uncertainties, some of the "natural" agents will stop sensing the gradient accurately or will not be able to correctly react to the sensed gradient. Such agents should be

isolated so that their overall effect on the locomotion of the system is minimized. In MAS, fault detection and isolation is achieved with the help of a central agent that isolates faulty agents (Davoodi et al.; 2016). However, natural computing process has to be robust enough to cater for this challenge on its own.

4.4.2.3 Learning Errors and Synchronization

In natural computation, sensing environmental parameters like the biophysical gradient is very essential. Due to the ever-changing characteristics of biological search space around the tumor, there are some errors associated with learning the environment. Synchronization, which is the alignment of actions taken by a "natural" agent in time with all other agents, is directly affected by these gradient sensing errors. To ensure an adequate performance of autonomous *in vivo* computation, it is crucial to consider the distortion caused by the learning errors.

4.4.2.4 Propagation Delay

Collaboration among agents in natural *in vivo* computation can only be achieved through non-electromagentic communications such as mechanical wave communications or molecular communications which will impose delay while sharing information among nanoparticles and their neighbours. This propagation delay introduces inter-reaction interference which may affect the overall efficiency of the homing process.

4.4.2.5 Finite Life Span

During the collective swarm movement of all "natural" agents toward the global optimum (tumor), it is inevitable that some agents may be disassembled and lost in

the biological environment through degeneration (deterioration of nanoparticles) or diffusion (spreading of nanoparticles), referred to as having finite life span. Thus, it is important to ensure a strong bond between nanoparticles and consider their finite life span during *in vivo* natural computation.

4.4.2.6 Formation during Obstacle Avoidance

Proliferation of vessels in peritumoral region leads to a very complex vasculature architecture which acts as a source of hindrance for "natural" agents homing for the tumor. Nanoparticles swarm assembly should be flexible enough to avoid these obstacles with strong bondage among them. Some of the nanoparticles are lost in the vascular architecture by sticking to the obstacles or following an undesired path (branching effect) which should be considered during the *in vivo* computing process.

4.5 Performance Analysis

4.5.1 Simulation Set-up

For evaluating the performance of our proposed strategy, MATLAB® is used as the simulation tool in the computational experiments. Self-regulated tumor homing is tested for different cost functions depicting contrasting domains. The search time allowed for each of the 200 independent simulation is 120 seconds where each simulation consists of 2000 iterations (position updates). There are four cost functions used to run simulations: sphere, Matyas, Gaussian and disc functions, representing the smooth, average, normally distributed, and zero-gradient domains

respectively. Fig. 4.7 illustrates the process. The nanoparticles (shown in blue) are randomly deployed at the same time in the region -5 mm $\leq x, y \leq -4$ mm. When the nanoparticles cross the green circle of radius 0.5 mm, they are considered to have reached the tumor (shown with green colour of nanoparticles).

Five different search domains shown in Fig. 4.7 with an increased level of complexity from top to bottom are imprinted on the representative objective functions explained in Section 4.3.1. The algorithm is first tested in free space with no obstacles (Fig. 4.7(a)) which represents the ideal case. The search domain is extended to have a single horizontal or vertical obstacle (Fig. 4.7(b) and (c)). A host environment with layers of obstacles (dashed) poses multiple hindrances to nanoparticles, and thus a higher level of complexity is shown in Fig 4.7(d). Next, because normal capillaries produce a two-dimensional regularly vascularized homogeneous vessel network (Baish et al.; 1996; Baish and Jain; 2000) outlined by straight and rigid cylindrical vessels (McDougall et al.; 2002; Chen, Ali, Shi and Chaeng; 2019), we develop a two-dimensional grid network (Fig. 4.7(e)) to test the robustness of the proposed strategy. The grid structure is not present in the vicinity of the tumor as the occupancy of vessel network normally reduces near a tumor because of decrease in micro-vascular density. The direction of blood flow is assumed to be from bottom left to top right for all search domains. Finally, due to the ever presence of platelets and plasma (containing blood cells, nutrients and wastes) in the blood circulatory system, the two-dimensional grid structure is enhanced to incorporate mobile obstacles (red squares) with sizes much larger than nanoparticles as shown in Fig. 4.8. In addition to disintegrating the swarm of nanoparticles into smaller groups, these mobile obstacles will cause distortions during biological sensing. To emulate this phenomena, random and normally dis-

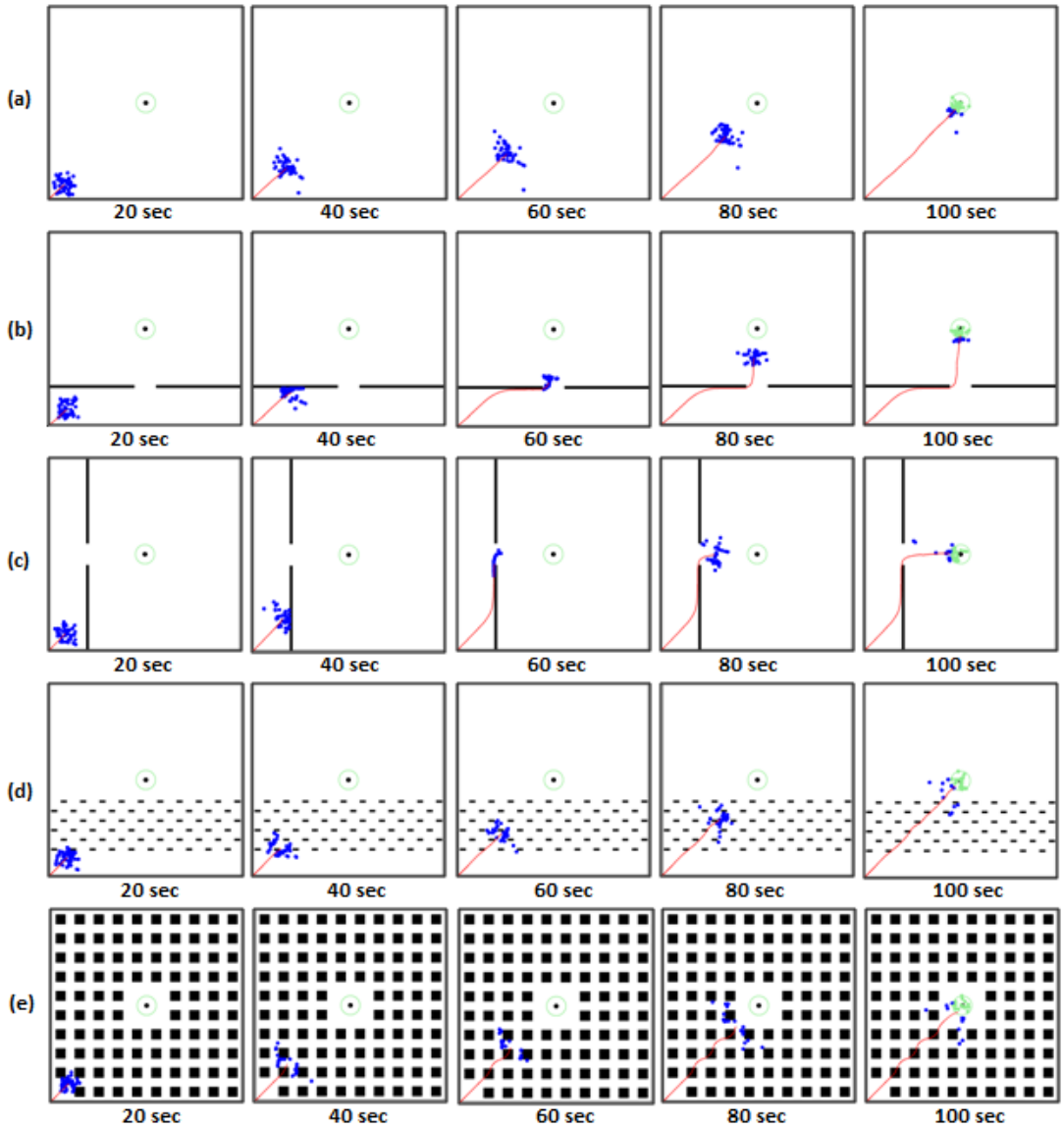

Figure 4.7: Demonstration of mean trajectory (shown in red) of tumor homing nanoparticles that are randomly deployed in the sphere search space without any obstacle ***(a)****. Any nanoparticle coming inside the vicinity (shown with green circle) of the tumor (shown with black dot) is considered to have successfully located the tumor that is represented by going green from its original blue colour.* ***(b-c)*** *shows nanoparticles successfully avoiding horizontal and vertical obstacles respectively. More complex search domains are shown in* ***(d-e)****.*

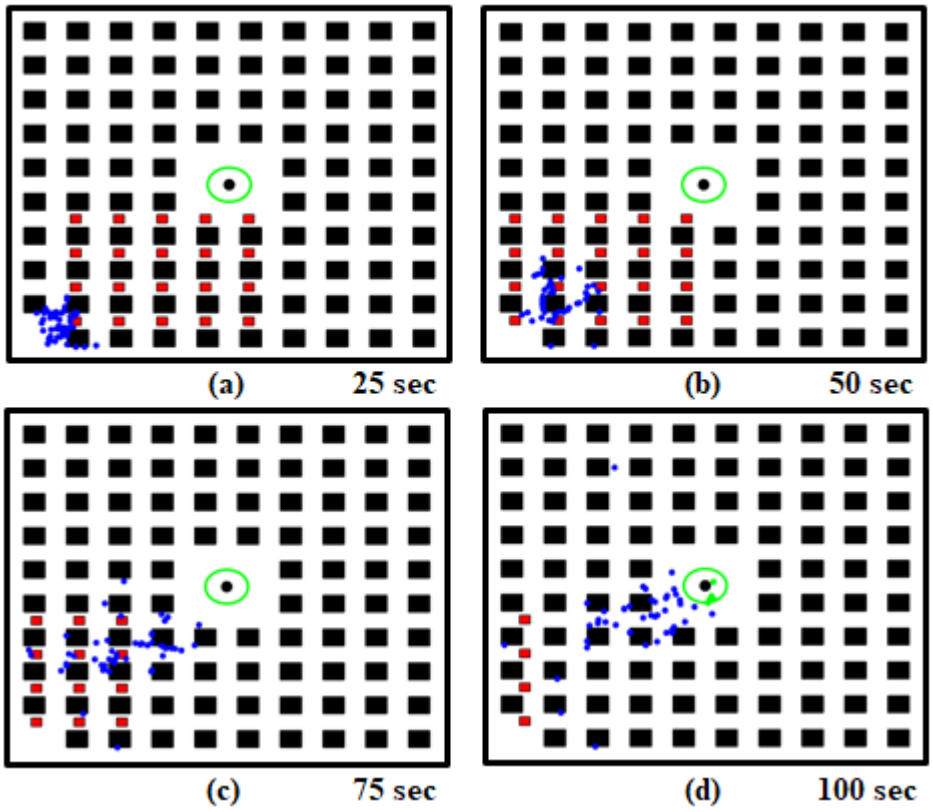

Figure 4.8: Illustration of swarm of nanoparticles avoiding static (grid network) and mobile obstacles (small red squares) during target directed locomotion.

tributed noise with zero mean and a standard deviation of $\sigma_{\Delta\zeta}$ is being introduced during the target homing.

Fig. 4.7 shows typical trajectories of nanoparticles for the sphere function. The tumor is shown with a black dot in the centre whereas the green circle of radius 0.5 mm around the tumor is used to evaluate the targeting efficiency η of the proposed framework. Any nanoparticle that touches or crosses the green circle of radius 0.5 mm is considered a successful detection and can deposit itself on the tumor because of the enhanced permeability and retention (EPR) effect or

receptor ligand binding. The overall targeting efficiency of the system is calculated as the ratio between the nanoparticles that have detected the tumor (in green) to the total number of deployed nanoparticles (green and blue) over the simulation settings defined in Section 4.5.1. If T_d and T_s represent the successful detection time and total search time respectively, and location of j^{th} nanoparticle is $\vec{x_j} \leq 0.5$ for $T_d \leq T_s$, then $N_d = N_d + 1$. Here, N_d represents number of nanoparticles which are inside the tumor region (the circle with the radius of 0.5 mm). η is then simply the ratio (N_d/N), for the swarm of N tumor homing nanoparticles.

4.5.2 Simulation Results

Fig. 4.7(a)-(c) show that nanoparticles while sensing the gradient and following the aggregation and migration principles explained in Section 4.3.2, successfully reached the tumor. Fig. 4.7(d) and (e) illustrate the path followed by the nanoparticles when complex search domains are presented. Fig. 4.8(a)-(d) shows the behaviour of the swarm on encountering the mobile obstacles. The swarm is disintegrated into smaller groups and forced to coordinate with lesser number of neighbours due to their cluster breakage. Once the swarm is split into smaller sub-groups by mobile obstacles, there are two main challenges for each obstructed nanoparticle. First, maneuvering across the obstacle which is much larger in size results in an excess time delay. Second, the number of neighbours available for passive collaboration is reduced. Both these factors will have a negative influence on the targeting performance of the swarm. Furthermore, different levels of noise (due to learning and synchronization errors) are presented to the swarm. Although nanoparticles continue to move towards the target, the overall targeting efficiency

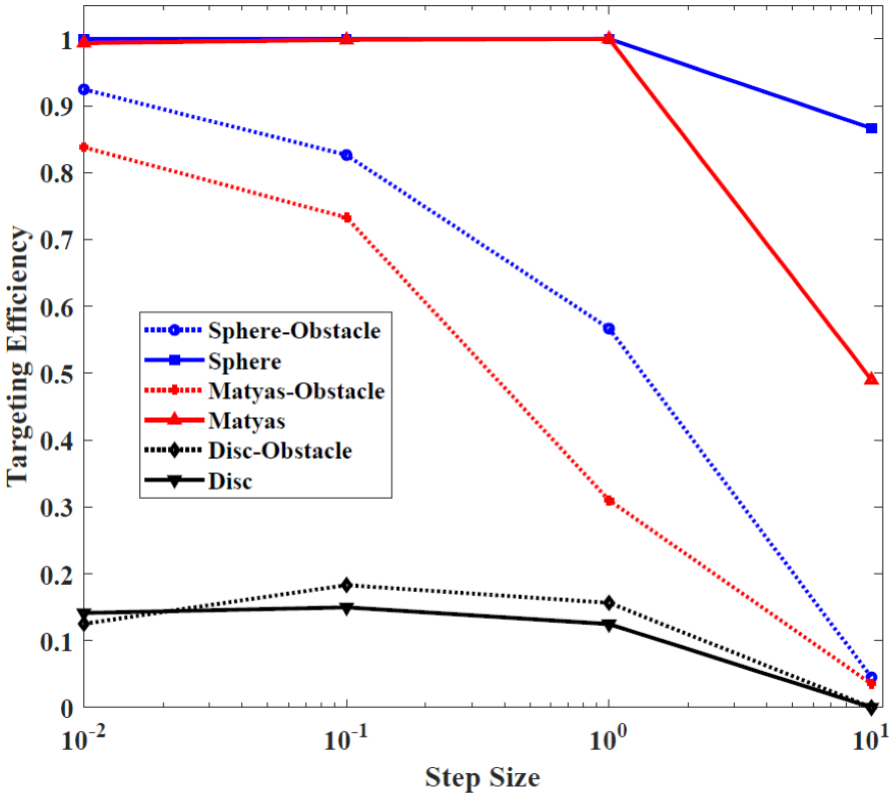

Figure 4.9: Targeting efficiency (η) under the influence of step size (γ) for sphere, matyas and disc landscapes. Solid lines shows the results for free space while dotted line is for search space with obstacles.

of the swarm is degraded when compared to the case with no mobile obstacles (simulation results in Fig. 4.13 and Fig. 4.14). Nevertheless, it is successfully demonstrated that the proposed targeting strategy is flexible and robust enough to help nanoparticles avoid obstacles (static and mobile) coming in their path while tumor homing.

Fig. 4.9 represents the targeting efficiency η of the swarm of nanoparticles with respect to the step size γ. Ideally, γ should be higher when the swarm is away from the target to achieve faster convergence and smaller when it gets closer to

the target to avoid by-passing of the target. Due to the absence of any external intervention and autonomous nature of our framework, it is not possible to change γ values during the homing process. For smaller γ values, our framework achieves targeting efficiency of more than 90% for the landscapes with gradient (sphere and Matyas), however when the step size is increased, the targeting efficiency degrades considerably due to target overshooting for all landscapes (sphere, Matyas and disc). During the target sensitization process, the sphere function with the smoothest transition in gradients, outperforms the Matyas and disc functions, whereas the disc function shows the the worst performance as expected due to lack of any gradient.

Fig. 4.10 demonstrates the influence of the number of neighbours K on targeting efficiency. It is clearly shown that the performance of the proposed algorithm is better with higher values of K even for the gradient-less disc landscape. For both sphere and Matyas functions, η increases significantly with the number of collaborating nanoparticles, for both free space (>90% for $K = 3$) and landscapes with obstacles (>80% for $K = 5$). The surface contact area of a nanoparticle which can be shared among its neighbours limits the value of K. A more complex design such as a chain-like structure of the swarm can help to increase the number of collaborating neighbours. If a large number of neighbours somehow can be linked to a particular nanoparticle and some nanoparticles of the swarm start self-regulated movements and blindly find the target, it will be interesting to have an acceptable η even for the gradient-less search domains such as the disc function.

In general, linear path loss is defined as the ratio of the transmitted information to the received information. However, for the current work, sharing of information is the BGF values sensed by the swarm of nanoparticles. Taking into account the

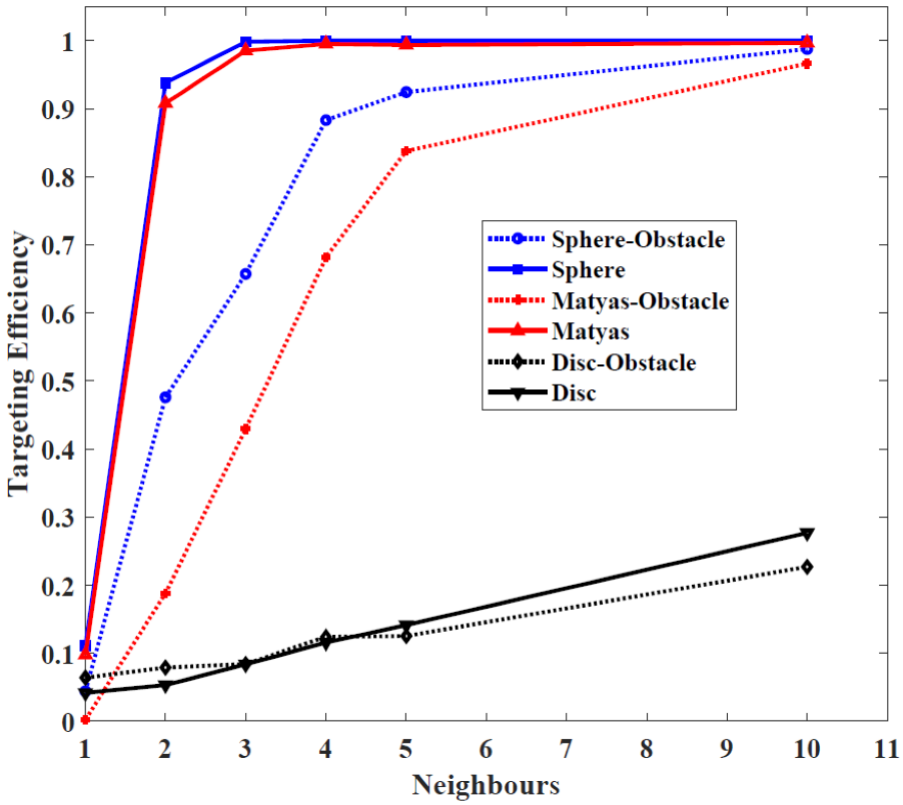

Figure 4.10: Targeting efficiency (η) under the influence of number of neighbours (K) for sphere, matyas and disc landscapes. Solid lines shows the results for free space while dotted line is for search space with obstacles.

effect of path loss exponent l, further simulations are run to see its influence on the targeting efficiency η. The range of l is typically from 2 to 6 in the field of wireless communications; 2 is for the free space propagation, 4 is for the lossy mediums while it is between 4 and 6 for indoor environments such as multi-storey buildings or crowded stadiums. For our computational experiments, path loss exponent showed the similar trend. For higher values of l, the targeting efficiency η is lower (around 40% for l=6). Targeting efficiency can be improved by increasing the number of collaborating neighbours $K = 10$, 20, 30 and 40 as shown in Fig. 4.11 but

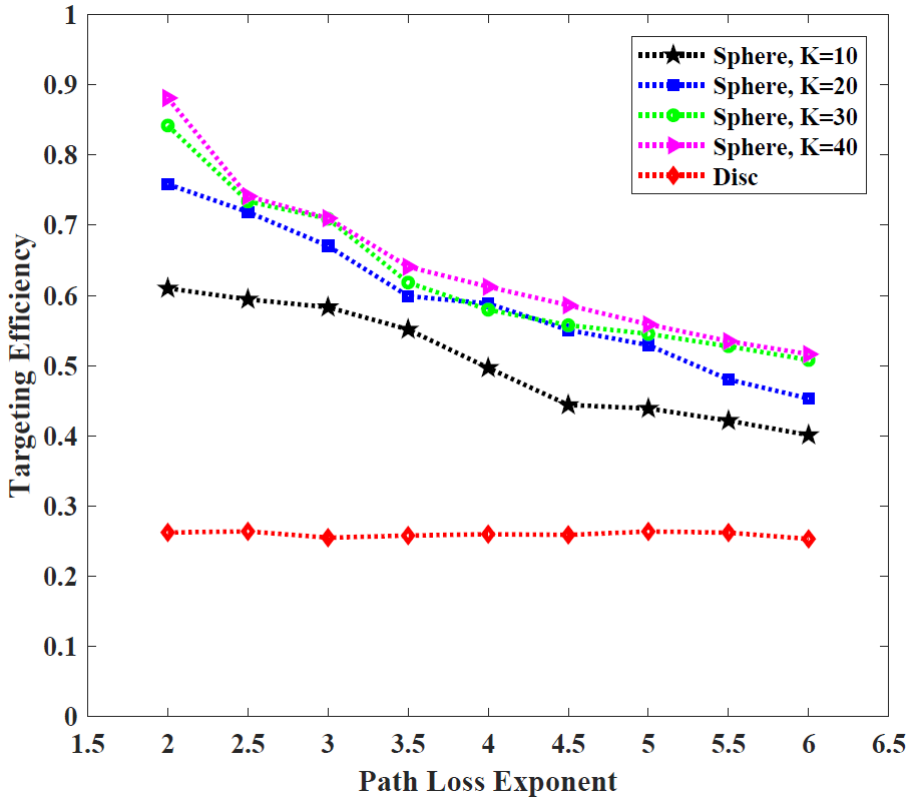

Figure 4.11: Targeting efficiency (η) under the influence of path loss exponent (l) with different collaborating neighbours (K) for sphere and disc landscapes.

the homing process becomes more computationally extensive requiring a complex (for example chain-like) design for a natural computing environment. Moreover, from a biological perspective, higher values of K introduce larger propagation delays as the sensed information needs to be shared and translated into overall locomotion for a greater group of nanoparticles. Note also that l does not have any effect on targeting efficiency for a disc landscape.

The grid structured search space in Fig. 4.7(e) is manipulated in the current simulation set-up to demonstrate the effect of occupancy on targeting efficiency η. A lower level of percentage occupancy (20%) gives better performance than a

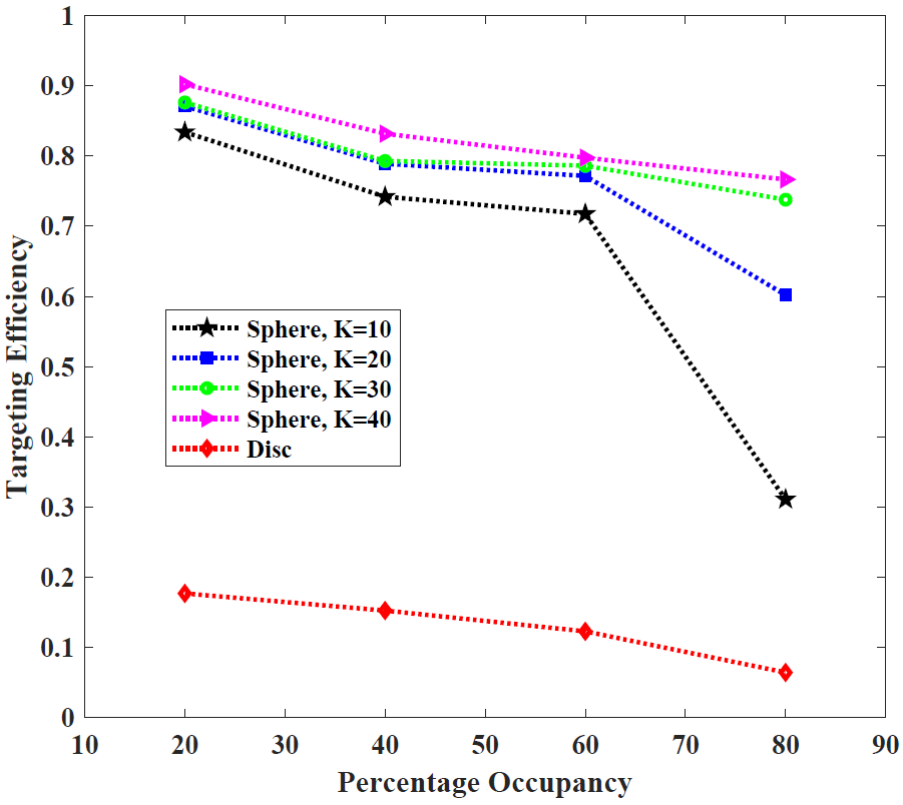

Figure 4.12: Targeting efficiency (η) under the influence of percentage occupancy with different collaborating neighbours (K) for sphere and disc landscapes.

higher level (80%). Natural computing environments such as peritumoral regions normally have higher levels of occupancy where the number of collaborating neighbours K can be increased to obtain the desired targeting efficiency. It can be seen in Fig. 4.12 that for the disc search space, even with $K = 40$, it does not give rise to satisfactory performance. However, for the sphere function, the targeting efficiency is increased as K is increased from 10 to 40.

All of the above mentioned simulation results are for noise-free gradient sensing without considering the non-idealities of the natural computation with prime focus on free-space and stationary obstacles. Fig. 4.13 and Fig. 4.14 show the results

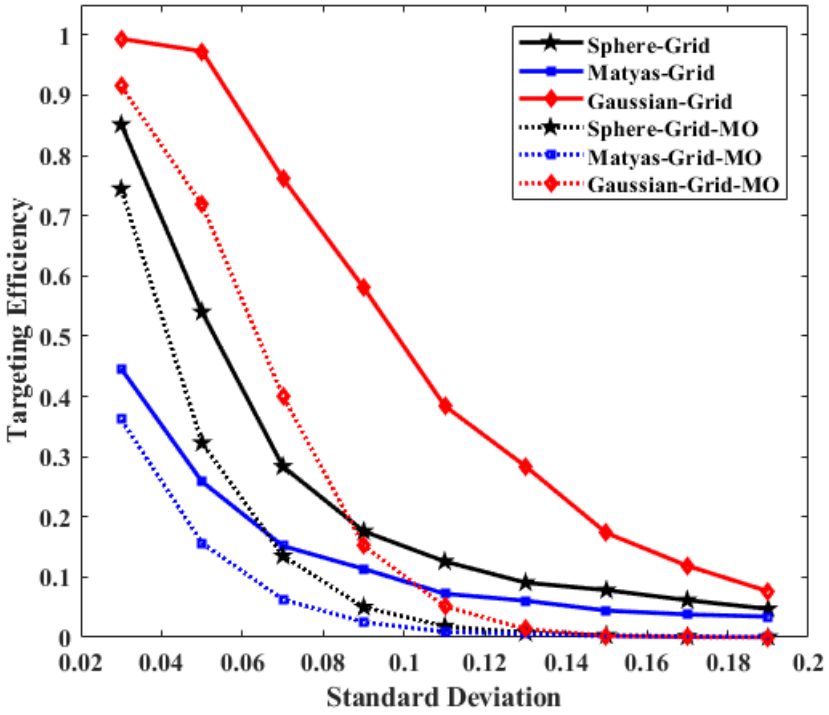

Figure 4.13: Targeting efficiency (η) under the influence of noise χ with zero mean and different standard deviations ($\sigma_{\Delta\zeta}$) for sphere, matyas and Gaussian landscapes with and without mobile obstacles.

after incorporating the non-idealities along with the ever-existing mobile obstacles that can affect the targeting performance of nanoparticles. Learning errors and propagation delays will introduce distortions during biological gradient sensing and on its induced effect respectively. Fig. 4.13 demonstrates that such distorting noise degrades the performance for all landscapes. Specifically, higher values of standard deviation contribute to larger noise levels, resulting in lower values of targeting efficiency. However, the Gaussian function performs better than the sphere and Matyas functions, both with and without the introduction of mobile obstacles.

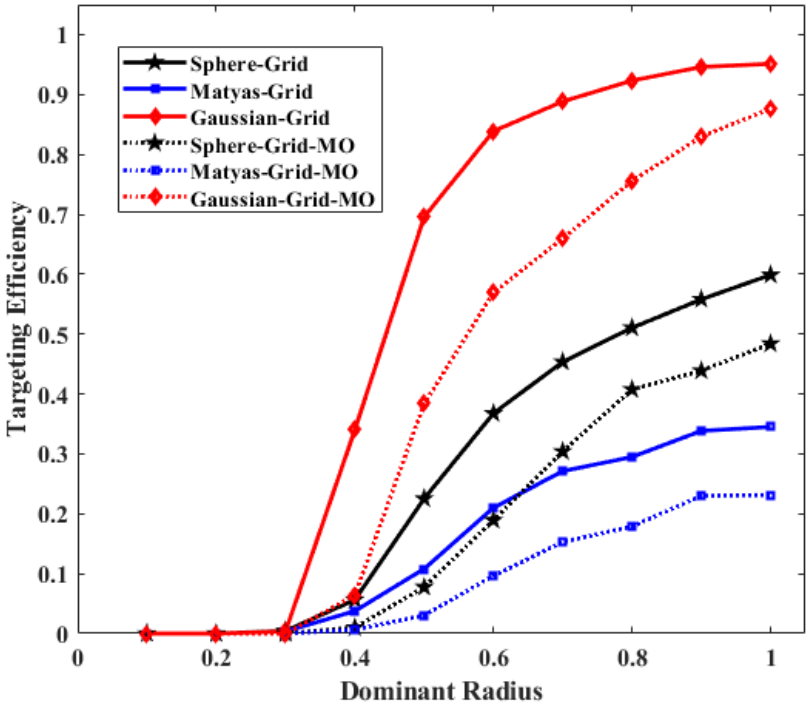

Figure 4.14: Targeting efficiency (η) under the influence of different dominant radii (R_d) for sphere, matyas and Gaussian landscapes with and without mobile obstacles.

Fig. 4.14 shows the effect of distance between a nanoparticle and its neighbour in a noisy environment for a grid-structured network. We introduced a circular threshold distance around a nanoparticle defined by the dominant radius R_d. For simplicity, it is assumed that any neighbour outside the circle of radius R_d will not have any effect on the nanoparticle. Hence, only those neighbours with their distance from the nanoparticle no greater than R_d are considered to be active neighbours, contributing in the homing process. Simulation results show that the Gaussian function performs better than the sphere and Matyas landscapes in the grid network. The trend remains the same when mobile obstacles are introduced during the target homing.

4.6 Conclusion

A novel self-regulated and bio-inspired autonomous approach for tumor detection has been proposed in this work. We have used computational experiments to demonstrate that morphological changes caused by the tumor-triggered biophysical gradients can be used to achieve target-directed locomotion for a swarm of nanoparticles. For noise-free search domains, different design parameters like path loss exponent, number of collaborating neighbours, step size and occupancy are considered with their impact on system performance. For a smooth gradient landscape such as a sphere function, the targeting efficiency is considerably improved from 10% to almost certain detection (>90%) when passive collaboration is achieved among as few as four nanoparticles. We also considered noisy search domains with the introduction of normally distributed random noise, along with the ever present mobile obstacles in complex grid structure to verify the robustness and flexibility of the proposed strategy. This work will certainly open new doors of research for *in vivo* cancer detection through self-evolving systems which are operable without the aid of any external stimulus.

Current work can be extended in future to the discrete search domains, mimicking the actual vasculature around the tumor in which nanoparticles are limited to only pre-specified paths. Moreover, this framework can be applied to a multi-objective optimization approach where more than one tumor (metastasis) are present in the region of interest. Finally, the proposed targeting strategy should be validated with the help of experiments, taking into account the non-idealities of nanoparticles such as limited life span and their consumption in human vasculature due to the inevitable phenomena of branching and diffusion.

References

Ali, M., Cree, M. J., Sharifi, N. and Chen, Y. (2019). Nanoswimmer-oriented direct targeting strategy inspired by momentum-based gradient optimization, *2019 41st Annual International Conference of the IEEE Engineering in Medicine and Biology Society (EMBC)*, IEEE, pp. 741–744.

Ali, M., McGrath, N., Shi, S., Cree, M. J., Cheang, U. K. and Chen, Y. (2020). Bio-inspired self-regulated in-vivo computation for smart cancer detection, *2020 IEEE 20th International Conference on Nanotechnology (IEEE-NANO)*, IEEE, pp. 304–309.

Ali, M., Sharifi, N., McGrath, N., Cree, M. J. and Chen, Y. (2020). Self-regulated and co-ordinated smart tumor homing for complex vascular networks, *2020 42nd Annual International Conference of the IEEE Engineering in Medicine & Biology Society (EMBC)*, IEEE, pp. 378–381.

Bae, Y. H. and Park, K. (2011). Targeted drug delivery to tumors: myths, reality and possibility, *Journal of Controlled Release* **153**(3): 198.

Baish, J. W., Gazit, Y., Berk, D. A., Nozue, M., Baxter, L. T. and Jain, R. K. (1996). Role of tumor vascular architecture in nutrient and drug delivery: an invasion percolation-based network model, *Microvascular Research* **51**(3): 327–346.

Baish, J. W. and Jain, R. K. (2000). Fractals and cancer, *Cancer Research* **60**(14): 3683–3688.

Beija, M., Marty, J.-D. and Destarac, M. (2011). Thermoresponsive poly (n-vinyl caprolactam)-coated gold nanoparticles: sharp reversible response and easy tunability, *Chemical Communications* **47**(10): 2826–2828.

Bucci, O. M., Bellizzi, G., Borgia, A., Costanzo, S., Crocco, L., Di Massa, G. and Scapaticci, R. (2017). Experimental framework for magnetic nanoparticles enhanced breast cancer microwave imaging, *IEEE Access* **5**: 16332–16340.

Cheang, U. K., Kim, H., Milutinović, D., Choi, J. and Kim, M. J. (2017). Feedback control of an achiral robotic microswimmer, *Journal of Bionic Engineering* **14**(2): 245–259.

Chen, Y., Ali, M., Shi, S. and Chaeng, U. K. (2019). Direct targeting strategy for smart cancer detection as natural computing, *ICC 2019-2019 IEEE International Conference on Communications (ICC)*, IEEE, pp. 1–6.

Chen, Y., Ali, M., Shi, S. and Cheang, U. K. (2019). Biosensing-by-learning direct targeting strategy for enhanced tumor sensitization, *IEEE Transactions on Nanobioscience* **18**(3): 498–509.

Davoodi, M., Meskin, N. and Khorasani, K. (2016). Simultaneous fault detection and consensus control design for a network of multi-agent systems, *Automatica* **66**: 185–194.

Dorri, A., Kanhere, S. S. and Jurdak, R. (2018). Multi-agent systems: A survey, *IEEE Access* **6**: 28573–28593.

Felfoul, O., Mohammadi, M., Taherkhani, S., De Lanauze, D., Xu, Y. Z., Loghin, D., Essa, S., Jancik, S., Houle, D., Lafleur, M. et al. (2016). Magneto-aerotactic

bacteria deliver drug-containing nanoliposomes to tumour hypoxic regions, *Nature Nanotechnology* **11**(11): 941.

Ferrari, M. (2005). Cancer nanotechnology: opportunities and challenges, *Nature Reviews Cancer* **5**(3): 161–171.

Friedl, P. and Gilmour, D. (2009). Collective cell migration in morphogenesis, regeneration and cancer, *Nature Reviews Molecular Cell Biology* **10**(7): 445.

Gazit, Y., Berk, D. A., Leunig, M., Baxter, L. T. and Jain, R. K. (1995). Scale-invariant behavior and vascular network formation in normal and tumor tissue, *Physical Review Letters* **75**(12): 2428.

Hauert, S. and Bhatia, S. N. (2014). Mechanisms of cooperation in cancer nanomedicine: towards systems nanotechnology, *Trends in Biotechnology* **32**(9): 448–455.

Hu, W., Lum, G. Z., Mastrangeli, M. and Sitti, M. (2018). Small-scale soft-bodied robot with multimodal locomotion, *Nature* **554**(7690): 81.

Karimi, M., Ghasemi, A., Zangabad, P. S., Rahighi, R., Basri, S. M. M., Mirshekari, H., Amiri, M., Pishabad, Z. S., Aslani, A., Bozorgomid, M. et al. (2016). Smart micro/nanoparticles in stimulus-responsive drug/gene delivery systems, *Chemical Society Reviews* **45**(5): 1457–1501.

Kasban, H., El-Bendary, M. and Salama, D. (2015). A comparative study of medical imaging techniques, *Int. J. Information Sci. Intelligent System* **4**: 37–58.

Kelley, E. G., Albert, J. N., Sullivan, M. O. and Epps III, T. H. (2013). Stimuli-responsive copolymer solution and surface assemblies for biomedical applications, *Chemical Society Reviews* **42**(17): 7057–7071.

Komar, G., Kauhanen, S., Liukko, K., Seppänen, M., Kajander, S., Ovaska, J., Nuutila, P. and Minn, H. (2009). Decreased blood flow with increased metabolic activity: a novel sign of pancreatic tumor aggressiveness, *Clinical Cancer Research* **15**(17): 5511–5517.

Kwon, E. J., Lo, J. H. and Bhatia, S. N. (2015). Smart nanosystems: Bio-inspired technologies that interact with the host environment, *Proceedings of the National Academy of Sciences* **112**(47): 14460–14466.

Li, D., Ding, J., Zhuang, X., Chen, L. and Chen, X. (2016). Drug binding rate regulates the properties of polysaccharide prodrugs, *Journal of Materials Chemistry B* **4**(30): 5167–5177.

Li, S., Batra, R., Brown, D., Chang, H.-D., Ranganathan, N., Hoberman, C., Rus, D. and Lipson, H. (2019). Particle robotics based on statistical mechanics of loosely coupled components, *Nature* **567**(7748): 361.

Liu, B., Su, H., Li, R., Sun, D. and Hu, W. (2014). Switching controllability of discrete-time multi-agent systems with multiple leaders and time-delays, *Applied Mathematics and Computation* **228**: 571–588.

Lue, S. J., Chen, C.-H., Shih, C.-M., Tsai, M.-C., Kuo, C.-Y. and Lai, J.-Y. (2011). Grafting of poly (n-isopropylacrylamide-co-acrylic acid) on micro-porous polycarbonate films: Regulating lower critical solution temperatures for drug controlled release, *Journal of Membrane Science* **379**(1-2): 330–340.

Malekzad, H., Zangabad, P. S., Mirshekari, H., Karimi, M. and Hamblin, M. R. (2017). Noble metal nanoparticles in biosensors: recent studies and applications, *Nanotechnology Reviews* **6**(3): 301–329.

McDougall, S. R., Anderson, A., Chaplain, M. and Sherratt, J. (2002). Mathematical modelling of flow through vascular networks: implications for tumour-induced angiogenesis and chemotherapy strategies, *Bulletin of Mathematical Biology* **64**(4): 673–702.

Mimeault, M., Hauke, R. and Batra, S. K. (2008). Recent advances on the molecular mechanisms involved in the drug resistance of cancer cells and novel targeting therapies, *Clinical Pharmacology & Therapeutics* **83**(5): 673–691.

Park, B.-W., Zhuang, J., Yasa, O. and Sitti, M. (2017). Multifunctional bacteria-driven microswimmers for targeted active drug delivery, *ACS nano* **11**(9): 8910–8923.

Park, J.-H., von Maltzahn, G., Ong, L. L., Centrone, A., Hatton, T. A., Ruoslahti, E., Bhatia, S. N. and Sailor, M. J. (2010). Cooperative nanoparticles for tumor detection and photothermally triggered drug delivery, *Advanced Materials* **22**(8): 880–885.

Qian, W.-Y., Sun, D.-M., Zhu, R.-R., Du, X.-L., Liu, H. and Wang, S.-L. (2012). ph-sensitive strontium carbonate nanoparticles as new anticancer vehicles for controlled etoposide release, *International Journal of Nanomedicine* **7**: 5781.

Rozenberg, G., Bäck, T. and Kok, J. N. (2012). *Handbook of natural computing*, Springer.

s Vicsek, T. (1992). *Fractal growth phenomena*, World Scientific.

Seidi, K., Neubauer, H. A., Moriggl, R., Jahanban-Esfahlan, R. and Javaheri, T. (2018). Tumor target amplification: implications for nano drug delivery systems, *Journal of Controlled Release* **275**: 142–161.

Shamshirband, S., Anuar, N. B., Kiah, M. L. M. and Patel, A. (2013). An appraisal and design of a multi-agent system based cooperative wireless intrusion detection computational intelligence technique, *Engineering Applications of Artificial Intelligence* **26**(9): 2105–2127.

Shen, Y., Fu, X., Fu, W. and Li, Z. (2015). Biodegradable stimuli-responsive polypeptide materials prepared by ring opening polymerization, *Chemical Society Reviews* **44**(3): 612–622.

Shi, S., Sharifi, N., Cheang, U. K. and Chen, Y. (2019). Perspective: Computational nanobiosensing, *IEEE Transactions on Nanobioscience* **19**(2): 267–269.

Siegel, R. L., Miller, K. D., Fedewa, S. A., Ahnen, D. J., Meester, R. G., Barzi, A. and Jemal, A. (2017). Colorectal cancer statistics, 2017, *CA: A Cancer Journal for Clinicians* **67**(3): 177–193.

Sitti, M. (2009). Miniature devices: Voyage of the microrobots, *Nature* **458**(7242): 1121.

Song, S., Chen, F., Qi, H., Li, F., Xin, T., Xu, J., Ye, T., Sheng, N., Yang, X. and Pan, W. (2014). Multifunctional tumor-targeting nanocarriers based on hyaluronic acid-mediated and ph-sensitive properties for efficient delivery of docetaxel, *Pharmaceutical Research* **31**(4): 1032–1045.

Vicsek, T., Czirók, A., Ben-Jacob, E., Cohen, I. and Shochet, O. (1995). Novel type of phase transition in a system of self-driven particles, *Physical Review Letters* **75**(6): 1226.

Von Maltzahn, G., Park, J.-H., Lin, K. Y., Singh, N., Schwöppe, C., Mesters, R., Berdel, W. E., Ruoslahti, E., Sailor, M. J. and Bhatia, S. N. (2011). Nanoparticles that communicate in vivo to amplify tumour targeting, *Nature Materials* **10**(7): 545.

Weijer, C. J. (2009). Collective cell migration in development, *Journal of Cell Science* **122**(18): 3215–3223.

Wen, C.-Y., Xie, H.-Y., Zhang, Z.-L., Wu, L.-L., Hu, J., Tang, M., Wu, M. and Pang, D.-W. (2016). Fluorescent/magnetic micro/nano-spheres based on quantum dots and/or magnetic nanoparticles: preparation, properties, and their applications in cancer studies, *Nanoscale* **8**(25): 12406–12429.

Wilhelm, S., Tavares, A. J., Dai, Q., Ohta, S., Audet, J., Dvorak, H. F. and Chan, W. C. (2016). Analysis of nanoparticle delivery to tumours, *Nature Reviews Materials* **1**(5): 16014.

Yan, H. and Okuzaki, H. (2008). Temperature-responsive poly (n-isopropylacrylamide) gels containing polymeric surfactants, *Composite Interfaces* **15**(7-9): 661–670.

Zhang, L., Petit, T., Peyer, K. E. and Nelson, B. J. (2012). Targeted cargo delivery using a rotating nickel nanowire, *Nanomedicine: Nanotechnology, Biology and Medicine* **8**(7): 1074–1080.

Zhou, Z., Qutaish, M., Han, Z., Schur, R. M., Liu, Y., Wilson, D. L. and Lu, Z.-R. (2015). Mri detection of breast cancer micrometastases with a fibronectin-targeting contrast agent, *Nature Communications* **6**(1): 1–11.

Chapter 5

Semi-Autonomous *In Vivo* Computation in Internet of Bio-Nano Things

Magnetically assembled bioresorbable nanoswimmers can be used to highlight small tumors, thereby increasing the diagnostic capability of existing medical imaging techniques. Built upon our earlier work, this paper proposes a novel *in vivo* computational framework for early cancer detection. Engineered nanoswimmers experience a change in their physical properties under the influence of tumor-induced biological gradients. The biologically sensed data by such bio-nano things (nanoswimmers) can either trigger an autonomous target-directed motion or be assisted through external manipulation for steering the swarm towards the target. Previously developed externally manipulable *in vivo* computation requires constant monitoring of nanoswimmers, introducing positioning and steering errors along with a limit on the swarm size. A parallel approach called autonomous *in*

vivo computation helps to resolve the above drawbacks, but the tumor homing is slow contributing to a higher percentage of pre-detection loss of nanoswimmers. We propose the spot sampling strategy for an autonomous swarm which considers the whole swarm as a single entity for the purpose of its tracking and steering. We show through computational experiments (1) that the proposed semi-autonomous *in vivo* framework can achieve faster tumor sensitization in complex environments having static and mobile obstacles, and (2) that the spot sampling provides sufficiently precise data to steer the swarm towards the target, saving around 90% of the monitoring resource. Our proposed framework also helps to achieve a large swarm size (number of nanoswimmers) which in return can achieve higher deposition of nanoswimmers on malignant tumors.

5.1 Introduction

Early stage tumor detection is very vital to curing cancer which is a life threatening disease (Hori and Gambhir; 2011). The number of most cancerous cells grow exponentially and their detection at stage-1 can save significant number of lives worldwide (Tao et al.; 2017). However, early diagnosis of cancer is impeded by the low resolution of present medical imaging techniques (Kasban et al.; 2015). Biodegradable nanoparticles (Qian et al.; 2012; Malekzad et al.; 2017) have profound applications in current theranostic approaches. The resolution quality of imaging modalities can be improved through contrast enhancement, which is achieved by potential contrast agents such as magnetically selective nanoparticles (Felfoul et al.; 2016).

After performing their required task (i.e., highlighting the diseases tissues), nanoparticles are dissolved in the body causing no harm to the healthy tissues. Penetration into diseased tissues and adequate retention are necessary for high accumulation of contrast agents at the tumor site. Due to their small size, nanoparticles are an ideal candidate to yield improved biodistribution profiles compared to small molecules, as their passive accumulation in diseased tissues may benefit from the enhanced permeability and retention (EPR) effect (Kobayashi et al.; 2014). However, the delivery of such nanoparticles from a remote injection site to the tumors comes with its own set of challenges. The conventional systemic targeting which relies only on the human circulation system, delivers only a small percentage (0.7%) of the injected nanoparticles to the tumors (Wilhelm et al.; 2016).

Loss of nanoparticles in the human vasculature can be due to their movement towards wrong vessels that do not lead to the tumor (branching effect) or because of their diffusion and degradation (finite life span), before reaching the desired target. Moreover, they lack a steering force which is required to push them towards the target for faster tumor sensitization. Hence, nanorobotic technologies should be implemented to construct maneuverable nanoswimmers (NSs). External controlling equipment can be used to provide that much needed propelling force to the swarm of NSs (Ali et al.; 2016). However, such external manipulation is associated with real world constraints such as a uniform magnetic field for the whole swarm (Chen, Ali, Shi and Cheang; 2019). Moreover, to steer NSs towards the desired direction, they are continuously tracked and controlled externally which leads to positioning and steering errors (Shi et al.; 2020).

The aforementioned challenges of an externally manipulable system can be resolved through an autonomous and self-regulatable system. Engineered NSs can be tuned to the tumor-induced biological gradients based on the principle of "particle robotics" (Li et al.; 2019). Specifically, the strength of biological gradient which is passively sensed by each NS (acting like a biosensor), can trigger morphological changes in them, i.e., changes in their size and shape. This causes NSs to expand or contract, evolving into the pushing-and-pulling effect among their loosely coupled neighbors. Such collaboration among NSs behaves like an internet of bio-nano things where the sensed biological gradients can be translated into target-directed locomotion (Ali et al.; 2021). This decentralized approach is robust but can be slow in the absence of an external propelling force. As a result, higher consumption of NSs occurs in the human body before the target is detected.

In summary, conventional targeting strategies based on systemic circulation can deliver a small number of passive nanoparticles to the tumor. Factors such as branching, diffusion and biodegradation of nanoparticles in human vasculature contribute to poor targeting performance. To overcome this problem, NSs with state-of-the-art features such as biosensing, actuation and signaling (Rahul et al.; 2017), along with some sort of external steering, can improve the targeting efficiency of the tumor homing process. However, constant tracking of the swarm for external manipulation is challenging, particularly when the swarm size is large. Alternatively, an independent and noncentralized target localization approach, which is based on the stochastic (random) movements of NSs is tracking-free but suffers from slow detection of the target.

5.1.1 Contributions of the Current Chapter

This chapter is focused on developing a natural computing framework through the fusion of bio-sensed data by internet of bio-nano things. We aim to provide a solution to the limitations of the existing natural computational approaches, i.e., constant monitoring of an unscalable swarm with external steering in the manipulable *in vivo* computation (MIVC) and slower detection of the tumor in the autonomous *in vivo* computation (AIVC).

We propose a semi-autonomous framework called hybrid *in vivo* computation (HIVC) that achieves faster tumor sensitization through a highly scalable swarm. With the help of the autonomous swarm spot sampling (ASSS) strategy, we show that constant monitoring of the swarm is not essential for steering it towards the best possible direction. Specifically, the swarm first moves autonomously in the search space and then, the information about its gradient-dependent locomotion is fused to drive it towards the target. Finally, the ASSS strategy also reduces the steering and positioning imperfections incurred in the MIVC framework by spot sampling the collective movement of the swarm rather than continuously monitoring individual NSs.

The efficiency of the proposed tumor sensitization approach is evaluated through extensive simulation studies.

5.1.2 Organization of the Chapter

The paper is organized as follows. Section 5.2 gives the essential background knowledge about the MIVC and AIVC, which helps in presenting the HIVC. Section 5.3 starts with outlining the objective functions required to represent the

tumor-induced biological gradients. The proposed semi-autonomous framework is formulated next, highlighting the ASSS strategy for swarm steering. In Section 5.4, numerical examples are used to evaluate the performance of HIVC while some concluding remarks are drawn in Section 5.5.

5.2 Background

5.2.1 Externally Manipulable In vivo Computation

The local tumoral microenvironment is heterogeneous due to the presence of malignant tumors (Sutherland; 1988). This can be either due to the diversified passive properties of the peritumoral environment such as blood flow velocity, pH, tortuous blood vessel architecture, or through utilization of some "activator" nanomaterials such as gold nanorods that induce biological changes around the tumor. Such biological gradients are used to aid in developing agile early tumor diagnostic systems.

Nanoparticles assembled by 50–100 nm magnetic iron oxide nanoparticles can be used in such microenvironment that possess tumor-induced biological gradients. These NSs indirectly reveal the gradients while moving in the high-risk diseased area (Li et al.; 2017). Hence, the observable characteristics of NSs such as their velocity, size or trajectories can be probed by an external monitoring unit. The swarm of NSs is then steered towards the possible tumor location by an external magnetic field (Sun et al.; 2008). Once early malignant tumors are encountered, NSs tend to stop the homing process and deposit themselves at the peritumoral area through receptor-ligand binding. This phenomenon is perceived by the exter-

nal monitoring unit which notices an improved biodistribution profile resulting in contrast enhancement for medical imaging techniques.

Previously developed MIVC strategies (Chen et al.; 2016, 2017, 2019) require real-time monitoring of NSs to gather information for external controlling unit. Such a requirement poses a scalabilty challenge on the swarm of NSs. The increased number of NSs, the more complex it is to track their movements. Moreover, there are tracking errors due to the limited resolution of the positioning equipment and steering imperfections due to the constrained accuracy of the external steering unit. Finally, due to the limitation of a uniform magnetic field (Cheang and Kim; 2015), it is an insurmountable challenge to actuate all NSs towards their respective intended directions. Consequently, for any position update, the NSs are moved towards a compromised common direction. The aforementioned limitations are illustrated with gray boxes on the left hand side of Fig. 5.1.

5.2.2 Autonomous In vivo Computation

Computerized systems such as multi-agent systems use simplified agents with reduced capabilities, to solve complex engineering problems (Dorri et al.; 2018). These agents sense the environment around them and use the acquired knowledge along with historical data to solve simpler tasks. The results are then shared among their neighbors which help them in finding the solution to a difficult task. Working on the same lines, NSs (which act like *in vivo* bio-nano things) with no individual target-directed locomotion ability, can successfully move towards the target by leveraging tumor-triggered biological gradients. For example, PNIPAAm and its derivatives, alter their structure in response to a temperature change (Yan

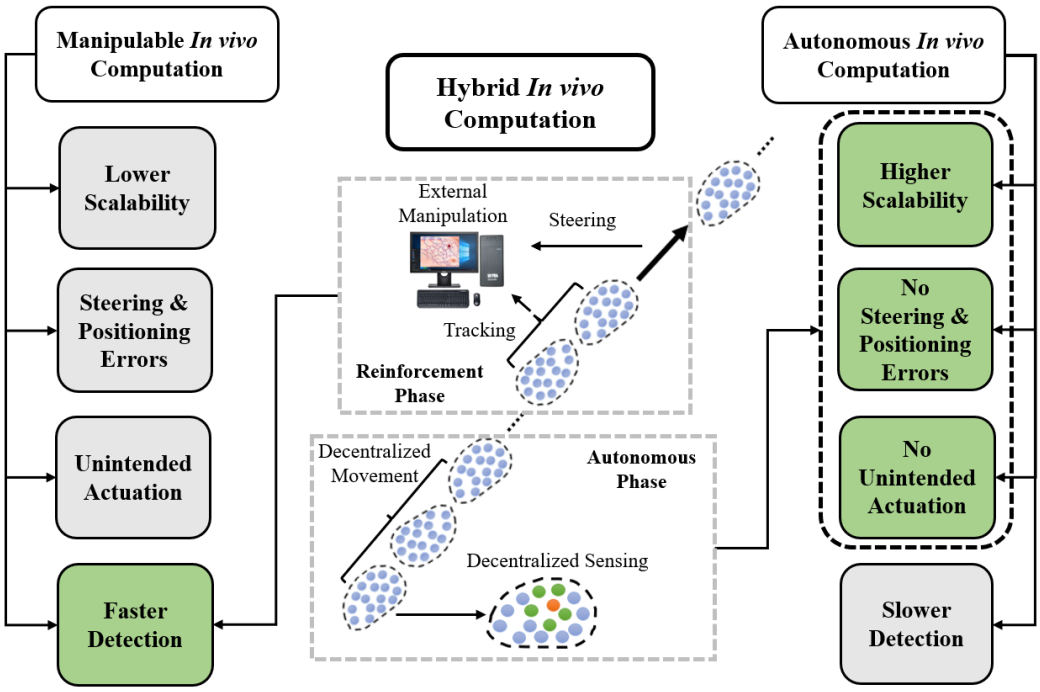

Figure 5.1: Proposed semi-autonomous hybrid in vivo *computation (HIVC) system extracting positive features (shown in green boxes) of the externally manipulable* in vivo *computation (MIVC) and the autonomous* in vivo *computation (AIVC).*

and Okuzaki; 2008; Beija et al.; 2011). Similarly, self-assembled miscelles undergo swelling in an acidic tumoral environment (pH = 6.8) from the stable condition in a healthy environment (pH = 7.4) (Li et al.; 2016). Such morphological and structural changes of NSs, along with collaboration among their neighbors (data fusion among bio-nano things), assist in aligning their directions towards the possible target location (Li et al.; 2019; Vicsek et al.; 1995).

This parallel approach termed as AIVC (Ali, McGrath, Shi, Cree, Cheang and Chen; 2020; Ali, Sharifi, McGrath, Cree and Chen; 2020; Ali et al.; 2021), addresses the aforementioned limitations of MIVC. The tumor homing is self-regulated and tracking-free due to the inherited proactive nature of the NSs. Such

a non-centralized swarm can orient itself in unfamiliar environments such as human vessels and efficiently perform difficult tasks such as bypassing the wrong vessel or drug transportation. In the absence of an external monitoring unit, this approach does not have any tracking or positioning errors. Moreover, scalability is not an issue here as the whole target detection procedure relies on self-evolving principles of aggregation and migration. However, tumor homing is slower due to the absence of any steering push from an external controlling unit (highlighted on the right hand side of Fig. 5.1). As a consequence, more NSs may be consumed in the human body before reaching the tumor.

5.2.3 Hybrid In vivo Computation

In the current work, we propose the HIVC framework which gives a solution to the limitations of both MIVC and AIVC as illustrated in Fig. 5.1. The swarm of NSs performs self-dependent tumor homing by passively sensing the tumor-induced biological gradients. Note that each NS behaves like a computation-free bio-nano thing with no independent ability to move towards the target. In response to the biological gradients, the self-tuning of NSs such as change in their size, surface properties or charge occurs, which is shared among their neighbors. Such collaboration among NSs essentially performs a multi-sensor fusion that helps in generating a targeting behaviour.

The scalability of the swarm in the proposed approach is not an issue as individual addressability of NSs is not required, thanks to their self-evolving nature. The homing process is also free of steering and positioning errors, because of the absence of real-time external manipulation. Moreover, as the target-directed

movement of the swarm is self-evolved, there is no unintended actuation of NSs. However, to achieve faster sensitization of the tumor, the swarm is propelled from time to time in the possible tumor direction with the help of an external magnetic field. It is worth mentioning here that such noninvasive propulsion of the swarm does not require real-time monitoring and is only done at specific time instants (spot sampling). The prime objective in the nanomedicine field is to maximize the swarm size, while keeping the size of each particle in the swarm to the minimum level. The large swarm size helps to achieve better contrast enhancement whereas smaller size of NSs is required for deeper penetration (van Moolenbroek et al.; 2020). The proposed approach is very flexible in terms of swarm size because the whole swarm is monitored as a single entity where tracking of individual NSs is not required.

5.3 Proposed Semi-autonomous HIVC

5.3.1 Objective Functions

Due to the presence of malignant tumors, the peritumoral region is altered physically (i.e., change in blood velocity and oxygen content (Baish et al.; 1996; Komar et al.; 2009)), chemically (i.e., change in redox potential and pH profile), and biologically (i.e., change in biomolecular cell structure and enzymes). As the research is in its early stage, there are no quantitative models available to adequately represent this tumor-induced biological gradient field (BGF). This BGF can be viewed as an objective function which is utilized to define the fitness landscape for the optimization agents (OAs). Hence, we resort to the objective functions shown in

Fig. 5.2 which are in general agreement with the qualitative observations made in the existing literature. They are widely used in the optimization theory and can provide some useful insights to the proposed tumor sensitization approach. The Sphere function has a smooth change in the gradient and is represented by a bowl-shaped landscape [Fig. 5.2(a)]. Next, the gradient of the Matyas function is more complex than the Sphere function but still better than the one in the form of a Disc function. The Matyas function forms a plate-shaped landscape [Fig. 5.2(c)]. Finally, the Disc function [Fig. 5.2(e)], corresponds to the worst case search space with zero gradient everywhere except the tumor location. The above mentioned objective functions are defined as

1. *Sphere Function:*

$$f(x,y) = \begin{cases} 1, & \sqrt{x^2+y^2} \leq 0.5 \\ 1 - 0.02\left(x^2+y^2\right), & \sqrt{x^2+y^2} > 0.5 \end{cases} \tag{5.1}$$

2. *Matyas Function:*

$$f(x,y) = \begin{cases} 1, & \sqrt{x^2+y^2} \leq 0.5 \\ 1 - 0.01\left(x^2+y^2\right) + 0.02xy, & \sqrt{x^2+y^2} > 0.5 \end{cases} \tag{5.2}$$

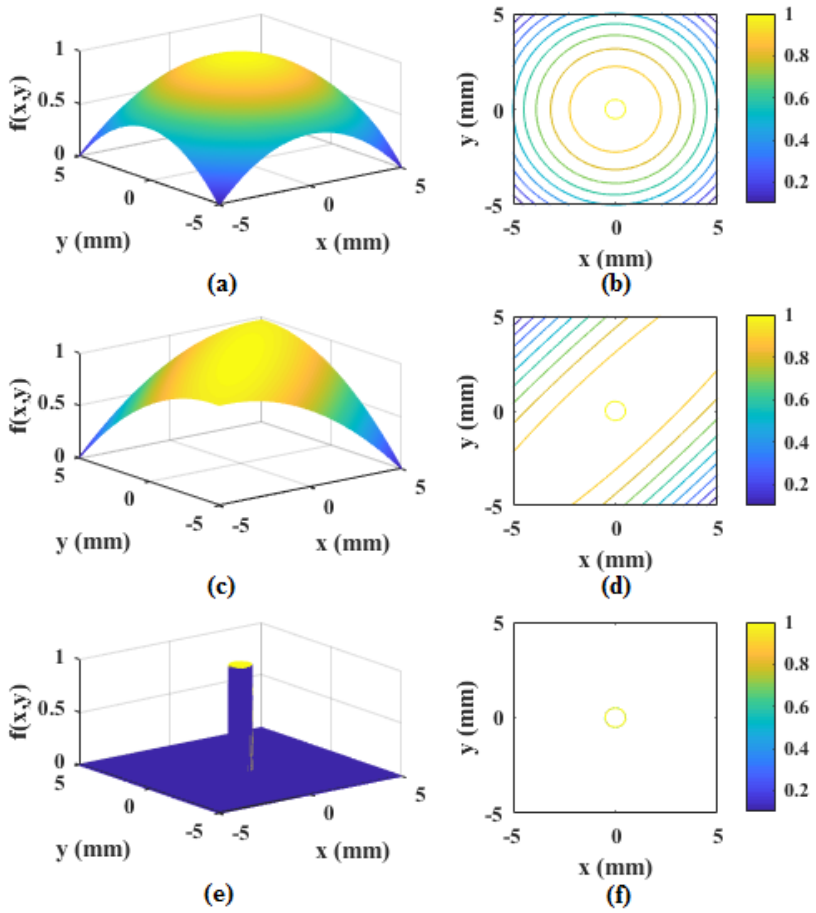

Figure 5.2: Illustration of $f(x, y)$ for three objective functions: Sphere function with its contour plot (a) and (b); Matyas function with its contour plot (c) and (d); Disc function with its contour plot (e) and (f). For the objective function $f(x, y)$, the small yellow circle in the centre of contour plots represents the maxima.

3. *Disc Function:*

$$f(x, y) = \begin{cases} 1, & \sqrt{x^2 + y^2} \leq 0.5 \\ 0, & \sqrt{x^2 + y^2} > 0.5 \end{cases} \tag{5.3}$$

The search space domain is defined within -5 mm $\leq x, y \leq 5$ mm whereas the maximum and minimum values of the objective functions are normalized to 0 and 1 respectively. The maximum is placed in the center of the domain for all the objective functions and is denoted by a small circle of radius 0.5 mm. As we move away from the center, the values of the Sphere and Matyas functions start decreasing and are 0 at the edges of their landscape. Note that the Disc function is an exception in which the BGF is zero throughout the landscape and then abruptly goes from 0 to 1 at the center.

5.3.2 Computational Framework

We propose a semi-autonomous framework in which the swarm of OAs representing NSs, move iteratively in decentralized (autonomous) and centralized (reinforcement) phases to detect the target. Broadly classifying, the autonomous phase represents the operation of AIVC where the passive collaboration among neighbors helps the swarm to achieve target-directed locomotion without the intervention of any external force. Similarly, the reinforcement phase represents the operation of MIVC where the swarm is steered through an external push to guide it towards the target. For simplicity, the case of a single maximum is considered which introduces an isotropic gradient. The steps involved in the framework are as follows.

1. *Initialization:* The swarm of N OAs are randomly deployed in a predefined and confined site -5 mm $\leq x, y \leq -4$ mm which is a localized region in the overall search space defined by -5 mm $\leq x, y \leq 5$ mm. The n^{th} OA is deployed at the point $\vec{x}_n$ within an injection area. After deployment, OAs start experiencing BGF passively as $\zeta_1(t_{\text{AP},l})$, $\zeta_2(t_{\text{AP},l}), \ldots, \zeta_{\text{N}}(t_{\text{AP},l})$ where

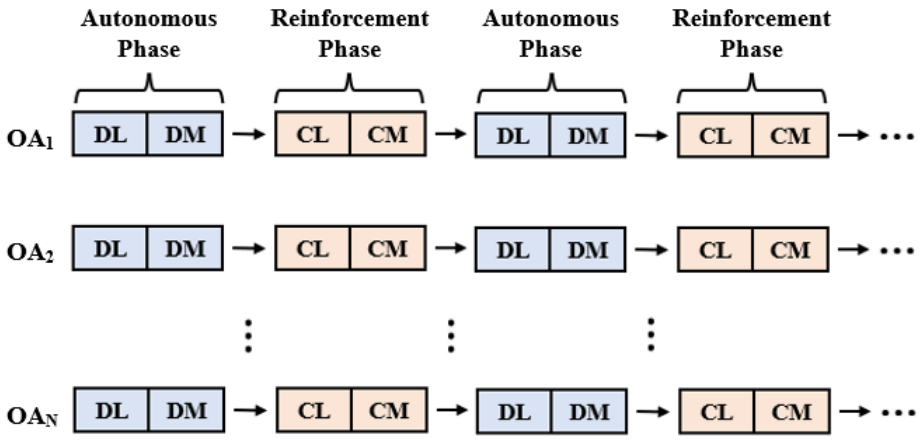

Figure 5.3: Illustration of the steps involved in semi-autonomous HIVC framework.

$\zeta_1(t_{\mathrm{AP},l}) = f\left(\vec{x_1}(t_{\mathrm{AP},l})\right), \zeta_2(t_{\mathrm{AP},l}) = f\left(\vec{x_2}(t_{\mathrm{AP},l})\right), \ldots, \zeta_{\mathrm{N}}(t_{\mathrm{AP},l}) = f\left(\vec{x_N}(t_{\mathrm{AP},l})\right)$. The index l represents a small step in the autonomous phase explained next.

2. *Autonomous Phase:* The BGF sensed by the OAs is shared amongst themselves in an independent and non-centralized manner. Such autonomous collaboration results in deterministic behaviours such as target directed locomotion (Li et al.; 2019). As shown in Fig. 5.3, the autonomous phase can be sub-divided into the decentralized learning (DL) and decentralized movement (DM) modes which are outlined below.

   (a) *DL Mode:* DL starts from selecting K neighbors among N OAs. This selection is based on the minimum distance criterion, so that the closest K OAs become neighbors of a particular OA. After neighbor identification, passive collaboration (sensing and sharing) of BGF information happens among an OA and its neighbors. The BGF experienced by an

OA and its neighbor are represented by $\zeta_{\mathrm{OA}}(t_{\mathrm{AP},l})$ and $\zeta_{\mathrm{B}}(t_{\mathrm{AP},l})$ respectively, and

$$\Delta\zeta(t_{\mathrm{AP},l}) = \zeta_{\mathrm{OA}}(t_{\mathrm{AP},l}) - \zeta_{\mathrm{B}}(t_{\mathrm{AP},l}) \tag{5.4}$$

is the difference in their sensed BGFs. Depending on whether a neighbor has sensed a higher or lower BGF, a particular OA is pushed or pulled by its neighbors. The sharing of BGF can only take place between an OA and its neighbor if the latter comes within the dominant radius of the OA as shown in the top left of Fig. 5.4. Hence, to cause a pushing/pulling effect due to change in size, a neighbor needs to be within the dominant radius of the corresponding OA. The effect of interaction experienced by an OA and its neighbor is given by

$$M(t_{\mathrm{AP},l}) = \begin{cases} \frac{\Delta\zeta(t_{\mathrm{AP},l})}{[\Delta d/d_{\mathrm{ref}}]^{\lambda}} \angle\left[\phi(t_{\mathrm{AP},l})\right], \text{for an OA-neighbor pair} \\ \\ 0, \qquad\qquad \text{for other OAs} \end{cases} \tag{5.5}$$

where Δd is the Euclidean distance between an OA and its neighbor, d_{ref} is a normalization factor, $\phi(t_{\mathrm{AP},l})$ is the direction of the effective passive collaboration and λ is the path loss exponent. The net directed effect of interactions (aggregation) due to K selected neighbors is calculated as

$$\vec{A}(t_{\mathrm{AP},l}) = \sum_{i=1}^{K} \frac{\Delta\zeta^{(i)}(t_{\mathrm{AP},l})}{[\Delta d^{(i)}/d_{\mathrm{ref}}]^{\lambda}} \, \vec{\hat{X}}_{\mathrm{off}}^{(i)}(t_{\mathrm{AP},l}) \, . \tag{5.6}$$

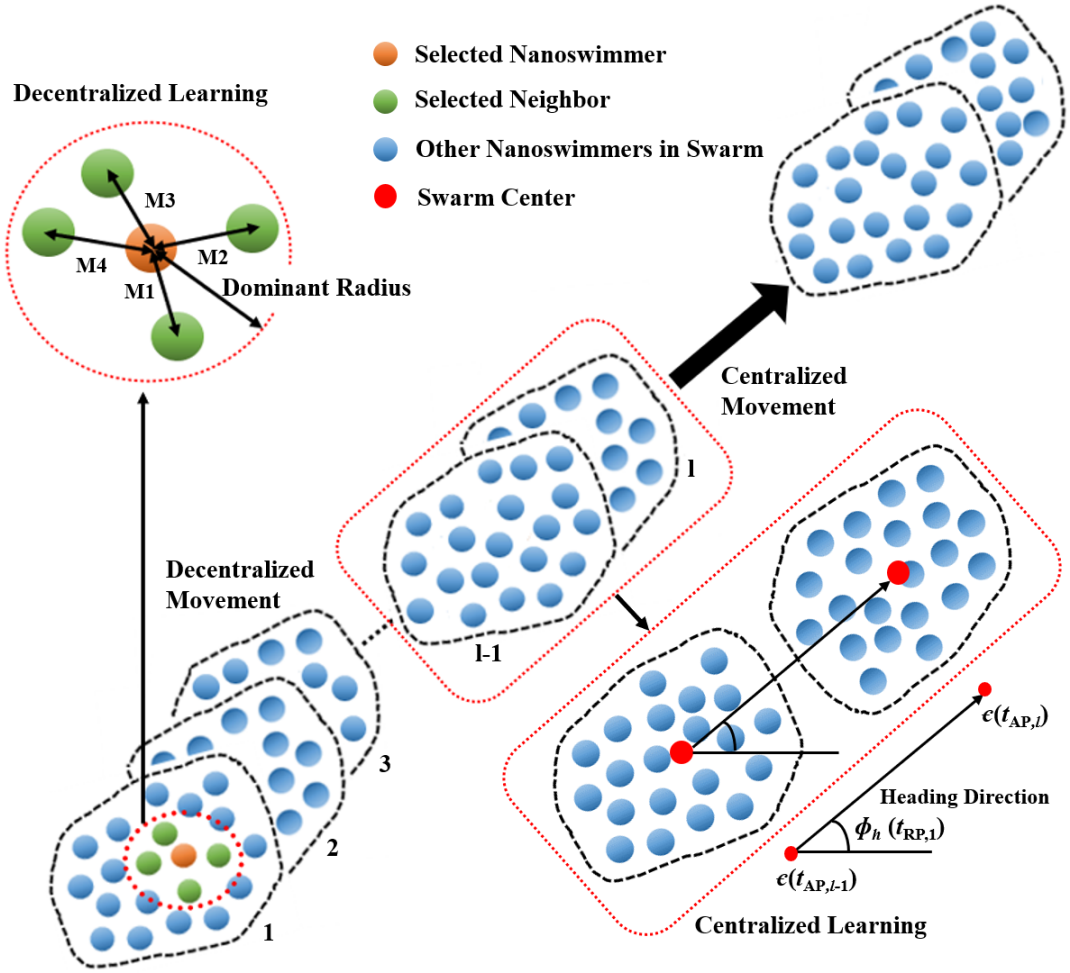

Figure 5.4: Pictorial representation of semi-autonomous hybrid in vivo *computation (HIVC) highlighting decentralized learning (top left) and decentralized movement in the autonomous phase and centralized learning (bottom right) and centralized movement in the reinforcement phase. The simplest case, when the last autonomous step is used to decide about the heading (steering) direction of the swarm is illustrated at the bottom right. The red dots labelled as $\vec{\epsilon}(t_{\mathrm{AP},l})$ and $\vec{\epsilon}(t_{\mathrm{AP},l-1})$, represent the swarm centers at the $(l-1)^{\mathrm{th}}$ and l^{th} autonomous steps respectively.*

Here, $\vec{X}^{(i)}_{\mathrm{off}}(t_{\mathrm{AP},l}) = \vec{x}_{\mathrm{OA}}(t_{\mathrm{AP},l}) - \vec{x}^{(i)}_{\mathrm{B}}(t_{\mathrm{AP},l})$ represents the displacement between an OA and its i^{th} neighbor such that $\vec{x}_{\mathrm{OA}}(t_{\mathrm{AP},l})$ and $\vec{x}^{(i)}_{\mathrm{B}}(t_{\mathrm{AP},l})$ are their locations in the search domain, respectively.

(b) *DM Mode:* After learning from the search space around them, OAs update their position based on the DL of the environment towards the resultant direction of the cooperative effect calculated in (6). In the DM mode, the i^{th} OA takes small autonomous steps $\vec{x}_i\left(t_{\text{AP},1}\right)$, $\vec{x}_i\left(t_{\text{AP},2}\right)$, $\cdots$, $\vec{x}_i\left(t_{\text{AP},L}\right)$, and the position update for the l^{th} step is given by

$$\vec{x}_i\left(t_{\text{AP},l}\right) = \vec{x}_i\left(t_{\text{AP},l-1}\right) + \gamma\vec{\hat{A}}\left(t_{\text{AP},l-1}\right), \quad \text{and} \quad l = 1, 2, \cdots, L. \tag{5.7}$$

Here, $\vec{x}_i\left(t_{\text{AP},l-1}\right)$ is the previous position of the OA, $\vec{x}_i\left(t_{\text{AP},l}\right)$ is the current position and L are the total steps in a single DM mode. The magnitude of this displacement (migration) depends on the autonomous phase step size γ. In natural computation, NS behaviours such as their ability to migrate (step size) rely on their physical properties like shape, size, composition material or a combination of them (Hauert and Bhatia; 2014).

3. *Reinforcement Phase:* From the decentralized modes in the autonomous phase, the swarm of OAs are then externally manipulated in the reinforcement phase with the help of the centralized learning (CL) and centralized movement (CM) modes.

(a) *CL Mode:* The CL mode relies on the autonomous phase as shown in Fig. 5.3. The BGF-dependent decentralized motion of the swarm is externally observed for P steps from the total L steps in the DM mode. This observation assists in computing the steering direction and magni-

tude of the swarm movement. We propose the autonomous swarm spot sampling (ASSS) strategy for this purpose. In ASSS, the swarm is spot sampled for certain consecutive steps rather than continuously monitored as required in externally manipulable computation (Chen, Ali, Shi and Cheang; 2019). The center of gravity of the swarm is evaluated by dividing the swarm shape in Y small equilateral and non-overlapping triangles. The gravity center of each triangle $(\vec{\mu}_0, \vec{\mu}_1, \cdots, \vec{\mu}_y)$ is simply the average of its three coordinates. Averaging out all the gravity centers and weighting them by the area of each triangle such that

$$\vec{\epsilon}(t_{\mathrm{AP},l}) = \frac{1}{Y} \sum_{i=1}^{Y} \vec{\mu}_y \left(t_{\mathrm{AP},l}\right) \chi_y \left(t_{\mathrm{AP},l}\right), \tag{5.8}$$

gives the approximate center of gravity $\vec{\epsilon}(t_{\mathrm{AP},l})$ of the swarm. The area of the y^{th} triangle (χ_y), is calculated by taking 2-D cross product of any two sides of the equilateral triangle. The angle between the x-axis and the vector $\vec{\epsilon}(t_{\mathrm{AP},l}) - \vec{\epsilon}(t_{\mathrm{AP},l-1})$, gives the heading direction $\phi_h\left(t_{\mathrm{RP},1}\right)$ for the first reinforced step of the swarm, based on the last autonomous step as illustrated in the bottom right of Fig. 5.4. Here the index l represents the autonomous step in the DM mode. When the swarm is monitored for P steps with autonomous step moving directions $\phi\left(t_{\mathrm{AP},1}\right)$, $\phi\left(t_{\mathrm{AP},2}\right)$,$\cdots$, $\phi\left(t_{\mathrm{AP},P}\right)$, the heading direction $\phi_h\left(t_{\mathrm{RP},1}\right)$ is estimated through the least square regression line (Aldrich; 1998). Given the collection of points $(p, \phi\left(t_{\mathrm{AP},p}\right))$, where $p = 1, 2, \cdots, P$, there is a line

$$\phi_h\left(t_{\mathrm{RP},1}\right) = \hat{\beta}_1 p + \hat{\beta}_0, \tag{5.9}$$

that best fits the data in the sense of minimizing the sum of the squared errors. Its slope $\hat{\beta}_1$ and y-intercept $\hat{\beta}_0$ are computed using the relations

$$\hat{\beta}_1 = \frac{SS_{p\phi(t_{\mathrm{AP},p})}}{SS_{pp}}, \tag{5.10}$$

and

$$\hat{\beta}_0 = \overline{\phi}\left(t_{\mathrm{AP},P}\right) - \hat{\beta}_1 \overline{P}, \tag{5.11}$$

where

$$SS_{pp} = \sum_{p=1}^{P} p^2 - \frac{1}{P}\left(\sum_{p=1}^{P} p\right)^2, \tag{5.12}$$

$$SS_{p\phi(t_{\mathrm{AP},p})} = \sum_{p=1}^{P} p\,\phi(t_{\mathrm{AP},p}) - \frac{1}{P}\left(\sum_{p=1}^{P} p\right)\left(\sum_{p=1}^{P} \phi(t_{\mathrm{AP},p})\right), \tag{5.13}$$

$$\overline{P} = \frac{1}{P}\sum_{p=1}^{P} p, \tag{5.14}$$

and

$$\overline{\phi}\left(t_{\mathrm{AP},P}\right) = \frac{1}{P}\sum_{p=1}^{P} \phi\left(t_{\mathrm{AP},p}\right). \tag{5.15}$$

Using the above relationships, (5.10) gives the estimated heading direction $\phi_h\left(t_{\mathrm{RP},1}\right)$ for the swarm. Note, that $P = L$ is the special case where all autonomous steps are monitored. This may give the best heading direction but the swarm needs to be observed throughout the autonomous phase. However, for the simplest case ($P = 1$), only the l^{th} and $(l-1)^{\mathrm{th}}$ steps are used to find its steering direction. Hence, there is a trade-off between the reliability of the estimated heading direction and the use of monitoring resources.

(b) *CM Mode:* The second step of the reinforcement phase is the CM mode in which the swarm of OAs is centrally steered towards the best direction that will most probably lead them to the optimal solution. The swarm of OAs evolve their positions according to

$$\vec{x}_i\left(t_{\mathrm{RP},1}\right) = \vec{x}_i\left(t_{\mathrm{AP},L}\right) + \Gamma\ \phi_h\left(t_{\mathrm{RP},1}\right), \tag{5.16}$$

where Γ is the step size for the reinforcement phase, $\vec{x}_i\left(t_{\mathrm{AP},L}\right)$ is the position at the last autonomous step and $\vec{x}_i\left(t_{\mathrm{RP},1}\right)$ is the current position of the OA. The steering vector in the direction of $\phi_h\left(t_{\mathrm{RP},1}\right)$ helps in guiding the collective movement of the swarm in the CM mode. This steering corresponds to the application of an external magnetic field in natural computation. Such centralized movement of the swarm is crucial to countering the physical constraint imposed by the finite life span of NSs as mentioned in Section 5.1.

In natural computation, the step size during the autonomous motion of the swarm is dependent on the inherent properties of NSs such as their sizes or shapes, whereas the step size during the centralized motion depends on the external steering equipment. As the aim is to achieve faster target sensitization, the duration of the reinforcement phase is longer as compared to the autonomous step duration. The step size for the reinforcement phase Γ is given by

$$\Gamma = v_{\mathrm{RP}}\ d_{\mathrm{RP}}\,, \tag{5.17}$$

where, the velocity v_{RP} of the swarm is assumed to be constant for simplicity and the duration of the reinforcement phase d_{RP} is given by

$$d_{\mathrm{RP}} = c\, e^{(-\alpha_{\mathrm{s}}/a_{\mathrm{o}})}\,. \tag{5.18}$$

Here, $\alpha_{\mathrm{s}} = \sum_{i=1}^{Y} \chi_y\,(t_{\mathrm{AP},L})$ is the area of the swarm after the last autonomous step in the DM mode and is determined by adding areas of all the Y triangles (as outlined in (5.8)), a_{o} is the normalization factor, and c is the constant. For $a_{\mathrm{o}} \to 0$, the reinforcement phase duration d_{RP} approaches the constant c as the exponential term in (5.18) equals 1. For $a_{\mathrm{o}} \to \infty$, the exponential term and consequently d_{RP}, both approach zero, which implies that the swarm will not move in the reinforcement phase for sufficiently large values of a_{o}. It is worth mentioning here that the swarm cannot be steered with over large steps through longer durations in the reinforcement phase, as this will degrade the targeting performance because of the target overshooting effect (Ali et al.; 2021).

4. *Termination:* The swarm of OAs continue to operate in the autonomous and reinforcement phases iteratively ($AP \rightarrow RP \rightarrow AP$), as the swarm advances towards the target. The homing process ends when an OA reaches the target. In natural computation, termination can be observed externally when OAs tend to stop their movement as mentioned in Section 5.2.1.

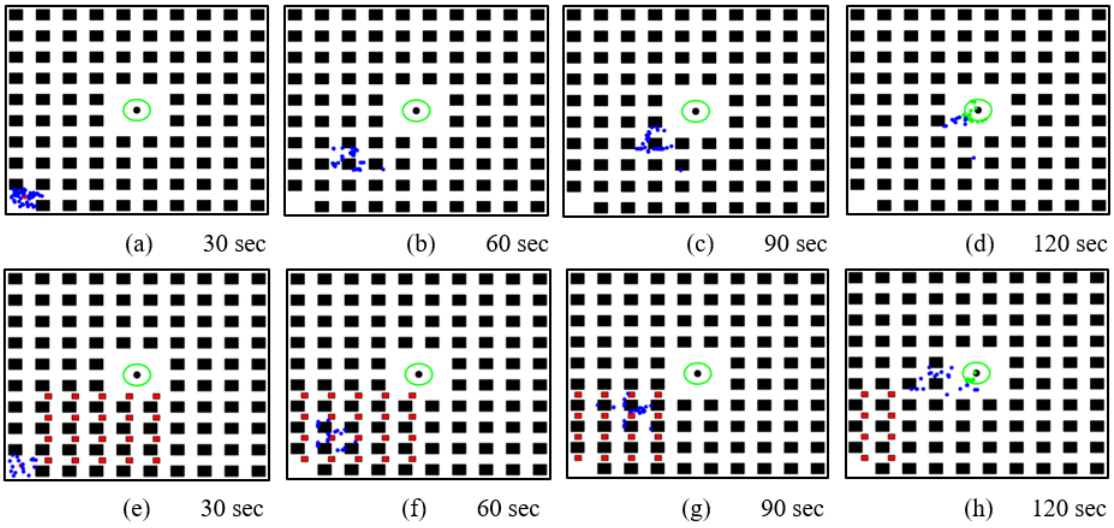

Figure 5.5: (a-d) Demonstration of target homing by swarm of optimization variables (representing nanoswimmers) when the Sphere function is overlaid on a grid network (static obstacles). (e-f) Illustrates of the swarm avoiding both static and mobile obstacles (small red squares).

5.4 Performance Analysis

To evaluate the target homing performance of our semi-autonomous HIVC framework, we use MATLAB® as a simulation tool for numerical analysis.

5.4.1 Simulation Setup

We use different cost functions having contrasting BGF profiles as stated in Section 5.3.1, which are overlaid on the search space shown in Fig. 5.5. The normal capillaries in the human body produce a homogeneous network which is vascularized regularly in 2-D (Baish and Jain; 2000; McDougall et al.; 2002). Therefore, the grid-like search domain depicts the vessel structure serving as the static obstacle network for the swarm. Moreover, the human circulation system always consists

of plasma, platelets, red and white blood cells, and some other nutrients. Hence, to be consistent with the natural environment, we introduce mobile obstacles as shown with red small boxes in Fig. 5.5. These mobile obstacles move from right to left and provide an additional hindrance to check the robustness of the swarm movement.

There are $N = 50$ OAs in the swarm, which are simultaneously positioned at random locations in the region -5 mm $\leq x, y \leq -4$ mm. The search time allowed for each of the 50 independent simulations is 150 seconds. The dominant radius R_d (to select neighbors which can collaborate mutually) around an OA is set to be 1 mm with the limit on the maximum number of neighbors K set to 20. So, an OA is not considered to be a neighbor if its distance is greater than R_d from another OA. For simplicity, the path loss exponent λ is 2. For the purpose of spot sampling, we are using the last two steps of the autonomous phase to find the steering direction for the swarm. The tumor is denoted by a small dot in Fig. 5.5, while any OA coming inside the green circle of radius 0.5 mm is considered to have detected the target. The overall targeting efficiency η is defined as the ratio between the number of OAs that have detected the target to the size of the swarm initially deployed.

5.4.2 Simulation Results

Fig. 5.5 (a-d) show that a swarm of OAs successfully detect the target following the principles of aggregation and migration in the autonomous phase and steering through spot sampling. The movement of the swarm is encountered by static obstacles (grid structure) during the homing process. Fig. 5.5 (e-h) illustrate

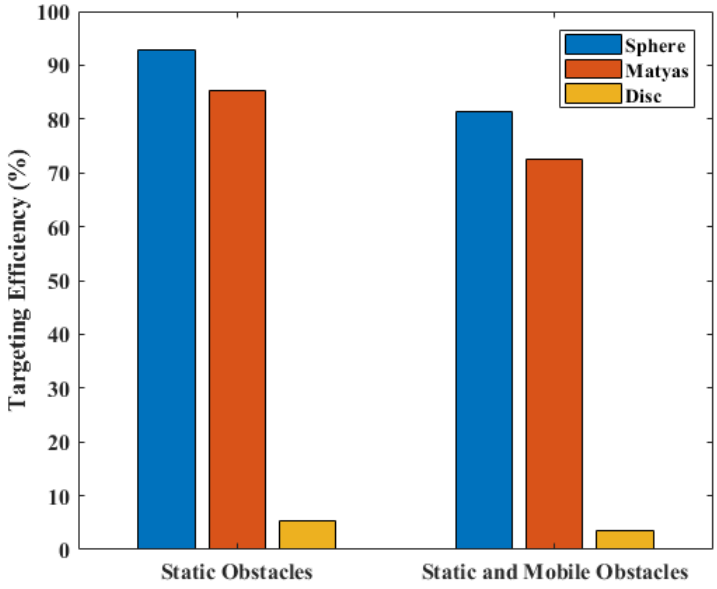

Figure 5.6: Targeting efficiency of the swarm in a grid structure with and without mobile obstacles.

a more complex environment for the swarm where mobile obstacles (shown with red boxes moving right to left) are also present along with static obstacles. The collision of OAs with mobile obstacles causes a delay in their collective motion towards the target. This can be observed in Fig. 5.5 by vertically comparing the swarm position at a particular time instant for both scenarios i.e., with and without mobile obstacles. Nevertheless, apart from the slight delay caused due to the scattering of swarm by mobile obstacles, their coordination is robust enough to reach the target successfully.

Fig. 5.6 presents the targeting performance of the swarm in the grid structure, both with and without mobile obstacles. The Sphere function gives the best performance with ($\eta = 81.44\%$) and without ($\eta = 92.76\%$) mobile obstacles followed by the Matyas function. As expected, the Disc function with zero gradient per-

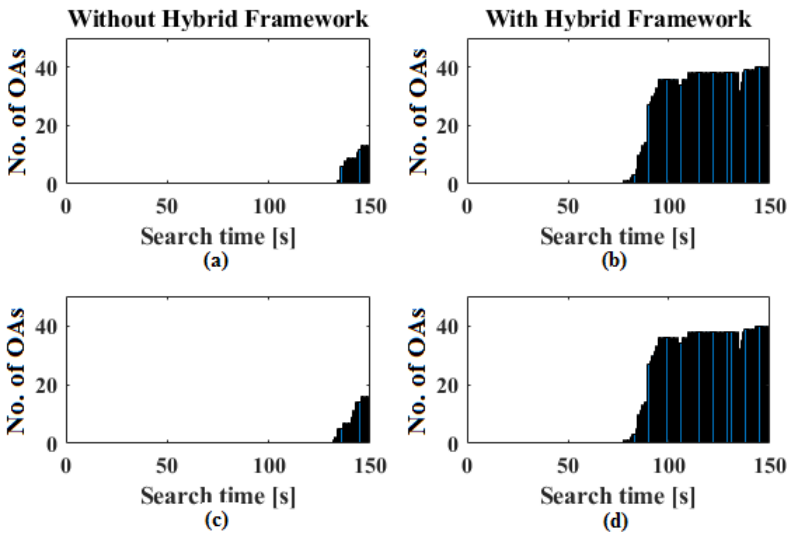

Figure 5.7: Comparison of detection time in grid network. The Sphere landscape with: (a) AIVC, (b) proposed HIVC, and the Matyas landscape with: (c) AIVC, (d) proposed HIVC.

forms the worst because the whole swarm coordination is BGF-dependent which is not available. It is worth mentioning here that the targeting performance shown in Fig. 5.6 is achieved by a sufficient reduction (approximately 85%) of the tracking computation as only 2 out of 15 steps in the autonomous phase are used to find the steering direction for OAs in the reinforcement phase. The general performance degradation of the swarm for all landscapes attribute to the splitting of the swarm due to mobile obstacles. First, the sub-clustering of the swarm causes a reduction in available neighbors for passive collaboration. Next, their movement across the mobile obstacles which are much larger in size, also results in an excess time delay.

Fig. 5.7 represents the search time of the swarm in the Sphere and Matyas landscapes in the grid network (static obstacles only). When the swarm is not

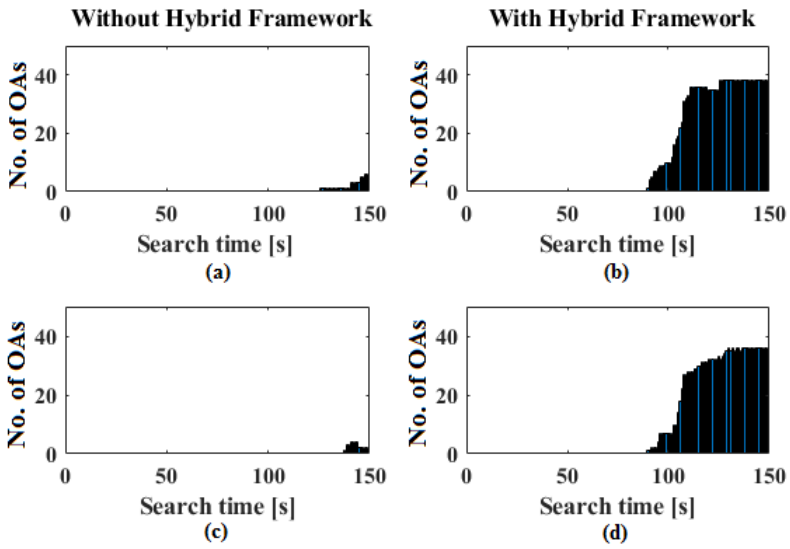

Figure 5.8: Comparison of detection time in grid network along with mobile obstacles. The Sphere landscape with: (a) AIVC, (b) proposed HIVC, and the Matyas landscape with: (c) AIVC, (d) proposed HIVC.

propelled through the proposed HIVC and target homing is fully autonomous, Fig. 5.7(a and c) show that only a small number of OAs reach the target within the total search time (150 secs). However, with the hybrid approach, the much-needed push is applied to the swarm which results in a higher number of OAs reaching the target as can been seen in Fig. 5.7(b and d). Specifically, the Sphere function has larger number of OAs (around 41 out of 50) reaching the target which is followed by the Matyas function. This worse performance is because of the more complex BGF in the Matyas function.

Fig. 5.8 also represents the detection performance but here the OAs have both static and mobile obstacles on their way to the target. The numerical results show that with the hybrid approach, OAs start detecting the target in approximately 33% less time compared to the autonomous target detection. It can be seen in

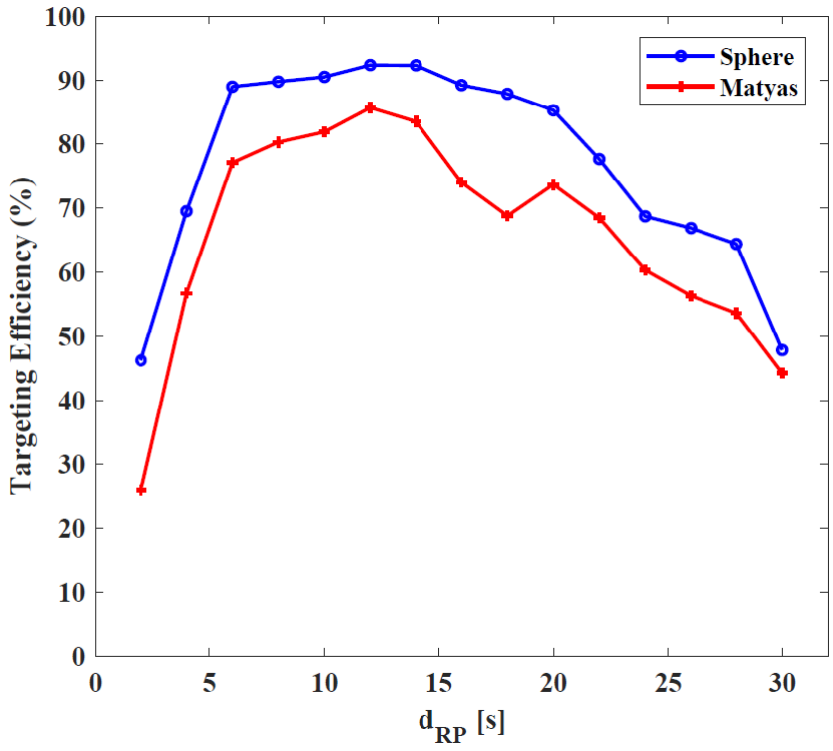

Figure 5.9: Performance comparison of the proposed HIVC in the Sphere and Matyas landscapes for different reinforcement phase durations.

Fig. 5.8(a and c) that the introduction of mobile obstacles further reduces the number of OAs reaching the target. However, for the Sphere function, the hybrid approach still manages to get a sufficient amount of OAs (around 37 out of 50) to the target. Again, the Sphere function performs better than the Matyas function. Note that we have not included the BGF-less landscape i.e., the Disc function in these results as its targeting efficiency is close to zero as shown in Fig. 5.6.

Targeting performance of the swarm for different durations of the reinforcement phase is illustrated in Fig. 5.9. It is shown that η peak and plateau for the Sphere and Matyas landscapes demonstrating better results within the range of

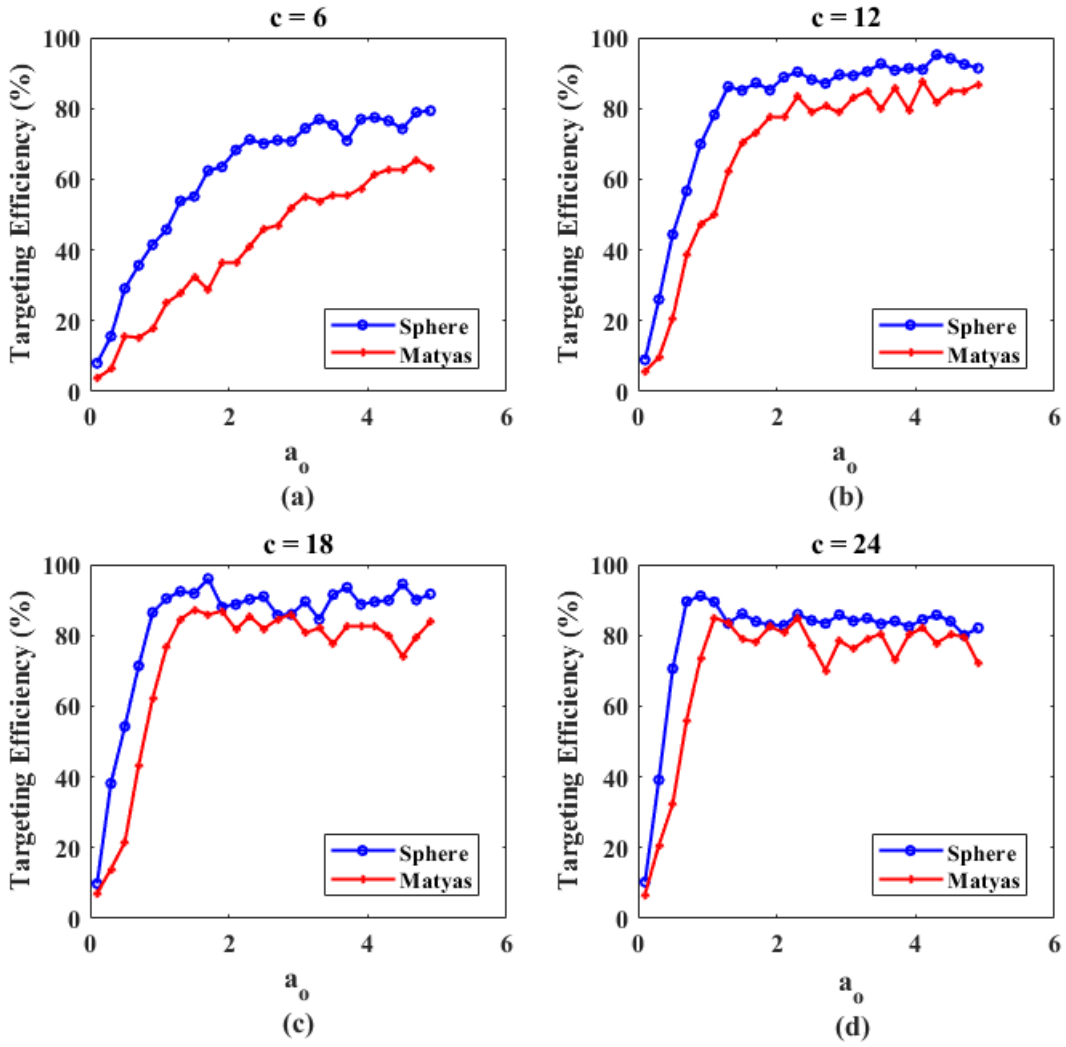

Figure 5.10: Performance comparison of the proposed HIVC in the Sphere and Matyas landscapes for the adaptive reinforcement phase duration model when: (a) c = 6, (b) c = 12, (c) c = 18 and (d) c = 24.

$8 \leq d_{\mathrm{RP}} \leq 20$ seconds. It is also evident that the Sphere function always gives better performance than the Matyas function for any particular value of d_{RP}.

Finally, numerical experiments are performed for the adaptive reinforcement phase duration based on (5.18). For simulation studies, different numerical values

are assigned to a_o (i.e. $a_o > 0$) for multiple values of constant c (i.e. $c = 6$, 12, 18 and 24). It can be seen that when the constant $c = 6$ (Fig. 5.10(a)), the slope of targeting efficiency η in getting to its peak value is not sharp. On the other hand, for higher values of c (Fig. 5.10(b, c and d)), the slopes of the η graphs become steeper. It is also observed that the peak value of η is higher when $c = 12$ and 18 (Fig. 5.10(b and c)), which is expected as they fall within the range of optimal d_{RP} observed in Fig. 5.9. Last, the potential performance deterioration of the Matyas function compared to the Sphere function is due to the more complex landscape of the former function.

5.5 Conclusion

We have proposed a novel semi-autonomous HIVC framework to address the limitations of MIVC and AIVC frameworks. Our numerical results demonstrate that swarm steering in the reinforcement phase helps to achieve faster sensitization (in approximately 33% less time) of the target compared to the autonomous approach. Moreover, simulation results also illustrate that through the ASSS strategy, a sufficient targeting efficiency (approximately 80% in a grid network with mobile obstacles) can be achieved, with less usage (around 85% less) of the monitoring resources compared to the manipulable tumor homing approach. The robustness of the targeting process has been evaluated in the presence of static and mobile obstacles with landscapes having different BGF profiles.

Further work may be done by incorporating the dynamic nature of the natural biological environment. The static objective functions may be replaced by the time-varying dynamic objective functions to evaluate the targeting performance of

the proposed framework. Finally, to justify their clinical relevance, the proposed strategies should be validated through *in vitro* experiments. A two-dimensional micro-fluidic blood vessel model can be used to depict the human vasculature and a magnetic control system can serve as the external steering and monitoring system.

References

Aldrich, J. (1998). Doing least squares: perspectives from gauss and yule, *International Statistical Review* pp. 61–81.

Ali, J., Cheang, U. K., Liu, Y., Kim, H., Rogowski, L., Sheckman, S., Patel, P., Sun, W. and Kim, M. J. (2016). Fabrication and magnetic control of alginate-based rolling microrobots, *AIP Advances* **6**(12): 125205.

Ali, M., Chen, Y. and Cree, M. J. (2021). Autonomous in vivo computation in internet of nano bio things, *IEEE Internet of Things Journal* **9**(8): 6134–6147.

Ali, M., McGrath, N., Shi, S., Cree, M. J., Cheang, U. K. and Chen, Y. (2020). Bio-inspired self-regulated in-vivo computation for smart cancer detection, *2020 IEEE 20th International Conference on Nanotechnology (IEEE-NANO)*, IEEE, pp. 304–309.

Ali, M., Sharifi, N., McGrath, N., Cree, M. J. and Chen, Y. (2020). Self-regulated and co-ordinated smart tumor homing for complex vascular networks, *2020 42nd Annual International Conference of the IEEE Engineering in Medicine & Biology Society (EMBC)*, IEEE, pp. 378–381.

Baish, J. W. and Jain, R. K. (2000). Fractals and cancer, *Cancer Research* **60**(14): 3683–3688.

Baish, J. W. et al. (1996). Role of tumor vascular architecture in nutrient and drug delivery: an invasion percolation-based network model, *Microvascular Research* **51**(3): 327–346.

Beija, M., Marty, J.-D. and Destarac, M. (2011). Thermoresponsive poly (n-vinyl caprolactam)-coated gold nanoparticles: sharp reversible response and easy tunability, *Chemical Communications* **47**(10): 2826–2828.

Cheang, U. K. and Kim, M. J. (2015). Self-assembly of robotic micro-and nanoswimmers using magnetic nanoparticles, *Journal of Nanoparticle Research* **17**(3): 145.

Chen, Y., Ali, M., Shi, S. and Cheang, U. K. (2019). Biosensing-by-learning direct targeting strategy for enhanced tumor sensitization, *IEEE Transactions on Nanobioscience* **18**(3): 498–509.

Chen, Y., Nakano, T., Kosmas, P., Yuen, C., Vasilakos, A. V. and Asvial, M. (2016). Green touchable nanorobotic sensor networks, *IEEE Communications Magazine* **54**(11): 136–142.

Chen, Y., Shi, S., Yao, X. and Nakano, T. (2017). Touchable computing: computing-inspired bio-detection, *IEEE Transactions on Nanobioscience* **16**(8): 810–821.

Chen, Y. et al. (2019). Direct targeting strategy for smart cancer detection as natural computing, *ICC 2019-2019 IEEE International Conference on Communications (ICC)*, IEEE, pp. 1–6.

Dorri, A., Kanhere, S. S. and Jurdak, R. (2018). Multi-agent systems: A survey, *IEEE Access* **6**: 28573–28593.

Felfoul, O. et al. (2016). Magneto-aerotactic bacteria deliver drug-containing nanoliposomes to tumour hypoxic regions, *Nat. Nanotechnol.* **11**(11): 941–947.

Hauert, S. and Bhatia, S. N. (2014). Mechanisms of cooperation in cancer nanomedicine: towards systems nanotechnology, *Trends in Biotechnology* **32**(9): 448–455.

Hori, S. S. and Gambhir, S. S. (2011). Mathematical model identifies blood biomarker–based early cancer detection strategies and limitations, *Sci. trans. med.* **3**(109): 109ra116–109ra116.

Kasban, H., El-Bendary, M. and Salama, D. (2015). A comparative study of medical imaging techniques, *Int. J. Inf. Sci. Intell. Syst.* **4**(2): 37–58.

Kobayashi, H., Watanabe, R. and Choyke, P. L. (2014). Improving conventional enhanced permeability and retention (epr) effects; what is the appropriate target?, *Theranostics* **4**(1): 81.

Komar, G., Kauhanen, S., Liukko, K., Seppänen, M., Kajander, S., Ovaska, J., Nuutila, P. and Minn, H. (2009). Decreased blood flow with increased metabolic activity: a novel sign of pancreatic tumor aggressiveness, *Clinical Cancer Research* **15**(17): 5511–5517.

Li, D., Ding, J., Zhuang, X., Chen, L. and Chen, X. (2016). Drug binding rate regulates the properties of polysaccharide prodrugs, *Journal of Materials Chemistry B* **4**(30): 5167–5177.

Li, J. et al. (2017). Micro/nanorobots for biomedicine: Delivery, surgery, sensing, and detoxification, *Science Robotics* .

Li, S., Batra, R., Brown, D., Chang, H.-D., Ranganathan, N., Hoberman, C., Rus, D. and Lipson, H. (2019). Particle robotics based on statistical mechanics of loosely coupled components, *Nature* **567**(7748): 361.

Malekzad, H., Zangabad, P. S., Mirshekari, H., Karimi, M. and Hamblin, M. R. (2017). Noble metal nanoparticles in biosensors: recent studies and applications, *Nanotechnology Reviews* **6**(3): 301–329.

McDougall, S. R., Anderson, A., Chaplain, M. and Sherratt, J. (2002). Mathematical modelling of flow through vascular networks: implications for tumour-induced angiogenesis and chemotherapy strategies, *Bulletin of Mathematical Biology* **64**(4): 673–702.

Qian, W.-Y., Sun, D.-M., Zhu, R.-R., Du, X.-L., Liu, H. and Wang, S.-L. (2012). ph-sensitive strontium carbonate nanoparticles as new anticancer vehicles for controlled etoposide release, *International Journal of Nanomedicine* **7**: 5781.

Rahul, V. A. et al. (2017). A brief review on nanorobots, *SSRG-IJME* **4**: 15–21.

Shi, S., Chen, Y. and Yao, X. (2020). In vivo computing strategies for tumor sensitization and targeting, *IEEE Transactions on Cybernetics* .

Sun, C., Lee, J. S. and Zhang, M. (2008). Magnetic nanoparticles in mr imaging and drug delivery, *Advanced Drug Delivery Reviews* **60**(11): 1252–1265.

Sutherland, R. M. (1988). Cell and environment interactions in tumor microregions: the multicell spheroid model, *Science* **240**(4849): 177–184.

Tao, Z., Dang, X., Huang, X., Muzumdar, M. D., Xu, E. S., Bardhan, N. M., Song, H., Qi, R., Yu, Y., Li, T. et al. (2017). Early tumor detection afforded by in vivo imaging of near-infrared ii fluorescence, *Biomaterials* **134**: 202–215.

van Moolenbroek, G. T. et al. (2020). Engineering intelligent nanosystems for enhanced medical imaging, *Adv. Int. Sys.* **2**(10): 2000087.

Vicsek, T., Czirók, A., Ben-Jacob, E., Cohen, I. and Shochet, O. (1995). Novel type of phase transition in a system of self-driven particles, *Physical Review Letters* **75**(6): 1226.

Wilhelm, S. et al. (2016). Analysis of nanoparticle delivery to tumours, *Nat. Rev. Mater.* **1**(5): 16014.

Yan, H. and Okuzaki, H. (2008). Temperature-responsive poly (n-isopropylacrylamide) gels containing polymeric surfactants, *Composite Interfaces* **15**(7-9): 661–670.

Chapter 6

Conclusion and Future Work

6.1 Conclusion

In this thesis, we have envisaged a new paradigm of *in vivo* computation (IVC) by developing different frameworks which can increase the tumor targeting performance. Externally manipulable, self-regulatable or hybrid IVC frameworks can be utilized as effective tools for tumor biosensing.

First, we have developed a novel iterative-optimization-based direct targeting strategy for externally manipulable framework. Computational experiments have shown that tumor-induced biological gradients can be used for "guided" direct targeting. While homing for the target, the framework facilitates nanoswimmers (NSs) to use the shortest physiological route having minimum system exposure. Numerical results demonstrate that probability of tumor detection and accumulation of drug nanoparticles can be significantly improved through the proposed direct targeting. However, NSs-oriented natural computing have some unique limitations such as uniform magnetic field to steer whole swarm (unintended actua-

tion), finite life span of nanoswimmers, damage to healthy tissues during target homing (cytotoxicity), steering and positioning errors due to the constrained accuracy of external equipment.

Second, built upon our earlier work on direct targeting framework, we have resolved three of the real life constraints of *in vivo* natural computation, i.e., (1) finite life span of NSs, (2) uniformity of magnetic field for swarm actuation, and (3) cytotoxicity. We have proposed the multi-estimate fusion (MEF) strategy to find a common steering direction for the whole swarm. Numerical results demonstrate that for symmetric orientations (tumor location in line with the blood flow direction), the mean of the individual gradient estimates provides the best steering direction, whereas for non-symmetric search space, estimate of the leader (with the largest value of the objective functions used to represent biological search space) can be selected for swarm steering to obtain best results. Next, the constraint of finite life span can be resolved through the iterative memory-driven gradient descent (MDGD) optimization which helps to detect the target faster compared to the classical memory-less gradient descent (MLGD) and systemic targeting. Also, the prime objective throughout the homing process with the proposed strategies is to maintain compactness of the swarm which is crucial to reduce the effect of cytotoxicity. Although, some of the key physical constraints are resolved, but the targeting approach still suffers from positioning and steer errors caused by the usage of external monitoring and controlling system.

Third, we have proposed a parallel framework for autonomous *in vivo* computation (AIVC) which as the name suggests, is independent of any external monitoring unit. This approach is inspired from the multiagent systems (MASs) where interacting agents with simplified functionalities and reduced capabilities, solve complex

problems that could not be solved by them on their own. We have first developed a one-to-one correspondence between the MAS and tumor detection through natural computation. Numerical experiments have shown that the tumor-triggered biological gradients can be leveraged by the NSs to successfully move towards the target. The homing ability of the swarm has been tested through different environments with non-identical orientations and complexity levels. Next, the reality checks of natural autonomous computing have been highlighted such as the effect of noisy search environments and interaction with ever-existing mobile obstacles. Finally, these non-idealities have been included in the search domain parameters for computational experiments, which has not only tested the robustness of the proposed approach but also provided a critical insight of the natural computation problem. However, this tumor homing approach is slow because there is no intervention of an external steering force to propel the swarm towards the target.

The aforementioned MIVC requires constant monitoring of the NSs, causing positioning and steering errors along with a scaling limit on the swarm size. On the other hand AIVC suffers from slow detection as the target-directed motion totally relies on self-regulated principles of aggregation and migration. Hence, to address these limitations, we have resorted to a semi-autonomous approach called hybrid *in vivo* computation (HIVC). We have proposed a spot sampling strategy which considers the whole swarm as a single entity for the operations of tracking and steering. The swarm is observed for a short duration to determine its steering direction. We have demonstrated through computational experiments that the proposed HIVC approach achieves faster target sensitization in complex search environments with static and mobile obstacles. The spot sampling not only

helps in reduction of monitoring source requirement but is also beneficial in the transportation of a larger swarm to the target.

6.2 Future Work

In the current work, the proposed IVC frameworks can be applied to find a single tumor. We have assumed that the tumor introduces an isotropic biological gradient which is leveraged by the NSs to probe the biological environment. Next, all of our numerical investigations are based on the hypothesis that the search environment is time invariant, i.e., it remains the same through out the target homing process. Hence, we are effectively considering the static function optimization problem.

Further Computational Frameworks: Future work may be done on extending the proposed frameworks to:

- Multi-solution optimization problem for multi-tumor detection. Such addition to the current work will help to address the natural phenomena of metastasis, in which malignant tumor cells can multiply and spread to bones, liver and lungs.

- The biological environment is dynamic in nature due to its ever-changing properties such as the flow of body fluids. The characteristics of the natural environment can also vary after interacting with the nanoparticles which makes it a dynamic optimization problem. Therefore, further investigations are required to incorporate the dynamic nature of the biological search space.

- Although we have included a range of vascular models for numerical experiments in the current research i.e., multi-layer layer discretized networks

with static and mobile obstacles; they are all two-dimensional. Further work needs to be done to generate three-dimensional network models which are more realistic to the natural environment.

- Moreover, the proposed frameworks are for successful detection of the tumor but do not consider the distribution of nanoparticles on the tumor itself. Further work may be done to extend current frameworks so that the uniform distribution of the nanoparticles can be achieved which may help in classification of the tumors.

- Finally, the current frameworks can be extended for multi-objective optimization problem. For example, after detection of the tumor, the drug delivery can also be performed to cure cancerous cells of malignant tumors.

In vitro Experiments: Nanomaterial-based pharmaceutical developments should be made so that the proposed frameworks can be validated through *in vitro* experiments. To emulate computational agents, novel magnetic Janus nanorobots composed of polystyrene (PS) polymeric nanoparticles coated on one side with nickel (Ni) can be utilized. A two-dimensional micro-fluidic blood vessel model can be used to depict the human vasculature and a magnetic control system can serve as the external steering and monitoring system.

In vivo Experiments: Verification of the results from *in silico* simulations by the *in vitro* experiments may be the first step towards the realization of the proposed nanobiosensing work by real experiments (with animals). The *in vivo* proof-of-concept can be obtained through an animal tumour xenograft model, which will further justify the clinical relevance of the current work.

Appendix

Co-Authorship Forms

The co-authorship forms related to four articles included in this thesis are provided on the following pages

THE UNIVERSITY OF WAIKATO
Te Whare Wānanga o Waikato

Co-Authorship Form

Postgraduate Studies Office
Student and Academic Services Division
Wahanga Ratonga Matauranga Akonga
The University of Waikato
Private Bag 3105
Hamilton 3240, New Zealand
Phone +64 7 838 4439
Website: http://www.waikato.ac.nz/sasd/postgraduate/

This form is to accompany the submission of any PhD that contains research reported in published or unpublished co-authored work. **Please include one copy of this form for each co-authored work.** Completed forms should be included in your appendices for all the copies of your thesis submitted for examination and library deposit (including digital deposit).

Please indicate the chapter/section/pages of this thesis that are extracted from a co-authored work and give the title and publication details or details of submission of the co-authored work.

Chapter 2: Biosensing-by-learning Direct Targeting Strategy for Enhanced Tumor Sensitization

Published in IEEE Transactions on Nanobioscience, doi: 10.1109/TNB.2019.2919132.

Nature of contribution by PhD candidate	Modelling, Computation, Writing and Reviewing
Extent of contribution by PhD candidate (%)	45

CO-AUTHORS

Name	Nature of Contribution
Yifan Chen	Modelling, Computation, Writing and Reviewing
Shaolong Shi	Reviewing
U Kei Cheang	Reviewing

Certification by Co-Authors

The undersigned hereby certify that:

- the above statement correctly reflects the nature and extent of the PhD candidate's contribution to this work, and the nature of the contribution of each of the co-authors; and

Name	Signature	Date
Yifan Chen	Yifan Chen	08/20/2022
Shaolong Shi	Shaolong Shi	8/19/2022
U Kei Cheang	U Kei Cheang	08/19/2022

THE UNIVERSITY OF WAIKATO
Te Whare Wānanga o Waikato

Co-Authorship Form

Postgraduate Studies Office
Student and Academic Services Division
Wahanga Ratonga Matauranga Akonga
The University of Waikato
Private Bag 3105
Hamilton 3240, New Zealand
Phone +64 7 838 4439
Website: http://www.waikato.ac.nz/sasd/postgraduate/

This form is to accompany the submission of any PhD that contains research reported in published or unpublished co-authored work. **Please include one copy of this form for each co-authored work.** Completed forms should be included in your appendices for all the copies of your thesis submitted for examination and library deposit (including digital deposit).

Please indicate the chapter/section/pages of this thesis that are extracted from a co-authored work and give the title and publication details or details of submission of the co-authored work.

Chapter 3: In Vivo Computation with Sensor Fusion and Search Acceleration for Smart Tumor Homing

Accepted in Computers in Biology and Medicine, doi: 10.1016/j.compbiomed.2022.105887

Nature of contribution by PhD candidate	Conceptualization, Modelling, Computation, Writing and Reviewing
Extent of contribution by PhD candidate (%)	70

CO-AUTHORS

Name	Nature of Contribution
Yifan Chen	Conceptualization and Reviewing
Michael J. Cree	Conceptualization and Reviewing
Mengjie Zhang	Reviewing

Certification by Co-Authors

The undersigned hereby certify that:

- the above statement correctly reflects the nature and extent of the PhD candidate's contribution to this work, and the nature of the contribution of each of the co-authors; and

Name	Signature	Date
Yifan Chen		20/08/2022
Michael J. Cree		22/08/2022
Mengjie Zhang	Mengjie Zhang here	19/08/2022

THE UNIVERSITY OF WAIKATO
Te Whare Wānanga o Waikato

Co-Authorship Form

Postgraduate Studies Office
Student and Academic Services Division
Wahanga Ratonga Matauranga Akonga
The University of Waikato
Private Bag 3105
Hamilton 3240, New Zealand
Phone +64 7 838 4439
Website: http://www.waikato.ac.nz/sasd/postgraduate/

This form is to accompany the submission of any PhD that contains research reported in published or unpublished co-authored work. **Please include one copy of this form for each co-authored work.** Completed forms should be included in your appendices for all the copies of your thesis submitted for examination and library deposit (including digital deposit).

Please indicate the chapter/section/pages of this thesis that are extracted from a co-authored work and give the title and publication details or details of submission of the co-authored work.
Chapter 4: Autonomous In vivo Computation in Internet-of-Nano-Bio-Things

Published in IEEE Internet of Things Journal, doi: 10.1109/JIOT.2021.3111089.

Nature of contribution by PhD candidate	Conceptualization, Modelling, Computation, Writing and Reviewing
Extent of contribution by PhD candidate (%)	70

CO-AUTHORS

Name	Nature of Contribution
Yifan Chen	Conceptualization and Reviewing
Michael J. Cree	Conceptualization, Editing and Reviewing

Certification by Co-Authors

The undersigned hereby certify that:

- the above statement correctly reflects the nature and extent of the PhD candidate's contribution to this work, and the nature of the contribution of each of the co-authors; and

Name	Signature	Date
Yifan Chen		20/08/2022
Michael J. Cree	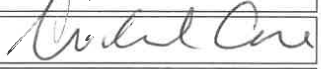	22/08/2022

THE UNIVERSITY OF WAIKATO
Te Whare Wānanga o Waikato

Co-Authorship Form

Postgraduate Studies Office
Student and Academic Services Division
Wahanga Ratonga Matauranga Akonga
The University of Waikato
Private Bag 3105
Hamilton 3240, New Zealand
Phone +64 7 838 4439
Website: http://www.waikato.ac.nz/sasd/postgraduate/

This form is to accompany the submission of any PhD that contains research reported in published or unpublished co-authored work. **Please include one copy of this form for each co-authored work.** Completed forms should be included in your appendices for all the copies of your thesis submitted for examination and library deposit (including digital deposit).

Please indicate the chapter/section/pages of this thesis that are extracted from a co-authored work and give the title and publication details or details of submission of the co-authored work.

Chapter 5: Semi-Autonomous In Vivo Computation through Biosensor Fusion for Smart Cancer Sensitization

To be submitted in Information Fusion Journal

Nature of contribution by PhD candidate	Conceptualization, Modelling, Computation, Writing and Reviewing
Extent of contribution by PhD candidate (%)	70

CO-AUTHORS

Name	Nature of Contribution
Yifan Chen	Conceptualization and Reviewing
Michael J. Cree	Conceptualization and Reviewing

Certification by Co-Authors

The undersigned hereby certify that:

- the above statement correctly reflects the nature and extent of the PhD candidate's contribution to this work, and the nature of the contribution of each of the co-authors; and

Name	Signature	Date
Yifan Chen	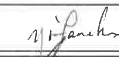	08/20/2022
Michael J. Cree		08/22/2022